

**STRETCHED
COORDINATE PML
in TLM**

By

Jomiloju Odeyemi, BEng



Thesis submitted to the University of Nottingham for the degree of Doctor of Philosophy,
December 2021

Abstract

As with all differential equation based numerical methods, open boundary problems in TLM require special boundary treatments to be applied at the edges of the computational domain in order to accurately simulate the conditions of an infinite propagating medium. Particular consideration must be given to the choice of the domain truncation technique employed since this can result in the computation of inaccurate field solutions. Various techniques have been employed over the years to address this problem, where each method has shown varying degree of success depending on the nature of the problem under study. To date, the most popular methods employed are the matched boundary, analytical absorbing boundary conditions (ABCs) and the Perfectly Matched Layer (PML). Due to the low absorption capability of the matched boundary and analytical ABCs a significant distance must exist between the boundary and the features of the problem in order to ensure that an accurate solution is obtained. This substantially increases the overall computational burden. On the other hand, as extensively demonstrated in the Finite Difference Time Domain (FDTD) method, minimal reflections can be achieved with the PML over a wider frequency range and for wider angles of incidence. However, to date, only a handful of PML formulations have been demonstrated within the framework of the TLM method and, due to the instabilities observed, their application is not widely reported. The advancement of the PML theory has enabled the study of more complex geometries and media, especially within the FDTD and Finite Element (FE) methods. It can be argued that the advent of the PML within these numerical methods has contributed significantly to their overall usability since a higher accuracy can be achieved without compromising on the computational costs. It is imperative that such benefits are also realized in the TLM method.

This thesis therefore aims to develop a PML formulation in TLM which demonstrates high effectiveness in a broad class of electromagnetic applications. Motivated by its suitability to general media the stretched coordinate PML theory will be basis of the PML formulation developed. The PML method developed in this thesis is referred to as the *mapped* TLM-PML due to the implementation approach taken

which avoids the direct discretization of the PML equations but follows more closely to the classical TLM mapping of wave equations to equivalent transmission line quantities. In this manner the highly desired unconditionally stability of the TLM algorithm is maintained. Based on the mapping approach a direct stretching from real to complex space is thus applied to the transmission line parameters. This is shown to result in a complex propagation delay and complex frequency dependent line admittances/impedances. Consequently, this modifies the connect and scatter equations.

A comprehensive derivation of the mapped TLM-PML theory is provided for the 2D and 3D TLM method. The 2D mapped TLM-PML formulation is demonstrated through a mapping of the shunt node. For the 3D case a process of mapping the Symmetrical Condensed Node (SCN) is formulated. The reflection performance of both the 2D and 3D formulations is characterised using the canonical rectangular waveguide application. Further investigation of the capability of the developed method in 3D TLM simulations is demonstrated by applying the mapped TLM-PML in: (i) the simulation of planar-periodic structures, (ii) radiation and scattering applications, and (iii) in terminating materially inhomogeneous domains. A performance comparison with previously proposed TLM-PML schemes demonstrates the superior temporal stability of the mapped TLM-PML.

Acknowledgements

First and foremost I would like to express my sincere gratitude to my supervisors Prof. Phillip Sewell, Prof. Ana Vukovic and Prof. Trevor Benson for the unwavering support they provided all through my research. I am especially thankful for the meticulous scrutiny provided on my papers and thesis. I am in awe of the perfect coordination amongst my supervisors which provided constant reassurance on the direction of the research. I am immensely grateful for the opportunity to have been guided by such brilliant minds.

I would like to acknowledge Dr Mark Panitz and Dr Chris Smartt for the opportunity to collaborate together and for the fruitful discussions which followed. I am especially thankful to Dr Chris Smartt for making time in his busy schedule to discuss different technical issues and for supporting with the implementation and demonstration of the PML technique within the GGITLM software.

I would like to give a special thanks to fellow members of the GGIEMR group who created an inspiring environment for me and motivated me throughout my research. I am thankful for the friendship I have found in: Dr Michael Basford, Dr Shakirudeen Lasisi, Dr Soumitra Kumar, Latifah, Kaiqi, Luke, Rohan and Ekrem.

I am most grateful for the support I have received from my family and friends. My academic journey has been filled with ups and downs but your love and patience with me have helped steady my spirit. I am especially thankful to my parents Oluyomi and Oluyemisi Odeyemi for their constant prayers and the deepest care and love shown. To my dearest siblings Adura, Mr Dimeji and Mofe thank you for being understanding. To Cassie, Ore, Abigail, Nadia, Joshua, Winifred, Mr Biyi and Dr Deke your encouragement through my many moments of self-doubt was very much appreciated.

Above all, to the Great and Almighty God, the author of knowledge and giver of all wisdom. I am grateful.

List Of Publications

The following papers have arisen out of the work described in this thesis:

Conferences

- I. **J. S. Odeyemi**, A. Vukovic, T. M. Benson and P. Sewell, "An improved PML implementation in the transmission line method," 2019, Tenth International Conference on Computational Electromagnetics (CEM 2019), pp. 1-4, 2019.
- II. **J. Odeyemi**, C. Smartt, A. Vukovic, T. M. Benson and P. Sewell, "PML Effectiveness in the Transmission Line Modelling Method for Radiation and Scattering Applications," 2020 14th European Conference on Antennas and Propagation (EuCAP), pp. 1-4, 2020.

Journals

- III. **J. Odeyemi**, A. Vukovic, T. Benson, P. Sewell, "Stretched-Coordinate PML in 2D TLM simulations," *IET Science, Measurement and Technology*, vol.14, no.3, pp. 272-277, 2020.
- IV. **J. S. Odeyemi**, A. Vukovic, T. M. Benson and P. D. Sewell, "A Complex Domain Mapping of the SCN for an Effective PML Implementation in TLM," in *IEEE Open Journal of Antennas and Propagation*, vol. 1, pp. 126-135, 2020.
- V. **J. Odeyemi**, M. Panitz, A. Vukovic, T. M. Benson and P. Sewell, "An Effective Stretched Coordinate TLM-PML Suitable for Analyzing Planar Periodic Structures," in *IEEE Microwave and Wireless Components Letters*, vol. 30, no. 8, pp. 725-728, Aug. 2020.

List Of Symbols

Below are a list of symbols that are frequently used throughout the thesis. Local symbols used in specific sections are excluded from this list.

\mathbf{E}	Electric Field Vector
\mathbf{H}	Magnetic Field Vector
$\bar{\epsilon}$	Permittivity Tensor
$\bar{\mu}$	Permeability Tensor
$\bar{\epsilon}_s$	Permittivity Tensor in Uniaxial PML
$\bar{\mu}_s$	Permeability Tensor in Uniaxial PML
ϵ_r	Relative Permittivity
μ_r	Relative Permeability
ϵ_0	Permittivity of Free Space
μ_0	Permeability of Free Space
$\bar{\sigma}_e, \bar{\sigma}_m$	Electric and Magnetic Conductivity Tensors
ρ	Total Electric Charge Density
$\sigma_x, \sigma_y, \sigma_z$	PML Electric Conductivities
$\sigma_x^*, \sigma_y^*, \sigma_z^*$	PML Magnetic Conductivities
ω	Angular Frequency
f	Frequency
c	Speed of Light in Free Space
k_x, k_y, k_z	Wave Numbers
\mathbf{k}	Wave Vector
S_i, S_i^*	PML Stretch Factors Applied to Electric and Magnetic Field Components
R_{th}	PML Theoretical Reflection Coefficient for Normally Incident waves
∇^s	Spatial Differential Operator Vector in Stretched Coordinate
∂_i	Partial Differential Operator for i-Coordinate
Δt	Time Step

Δl	Mesh Discretization Length
Z_0	Characteristic Impedance of Free Space
Y_0	Characteristic Admittance of Free Space
V_n^i	The Incident Voltage at Port n
V_n^r	The Reflected Voltage at Port n
\mathbb{R}	Real Number Space
\mathbb{C}	Complex Number Space
j	Imaginary Unit
s	Complex Argument in s Domain
z	Complex Argument in Z Domain
$\tilde{\cdot}$	Indicates the Complex Stretched Transmission Line Complements
L_{PML}	Total Thickness of the PML Medium
N_{PML}	Number of PML Layers
$\mathcal{F}(\cdot)$	Discrete Fourier Transform Operator
t	Time
σ_{max}	Peak PML Conductivity in the PML Medium

List of Abbreviations

CEM	Computational Electromagnetics
2D	Two Dimensional
3D	Three Dimensional
EM	Electromagnetic
IE	Integral Equation
BEM	Boundary Element Method
MOM	Method Of Moments
DE	Differential Equation
FDTD	Finite Difference Time Domain method
BPM	Beam Propagation Method
FEM	Finite Element Method
TLM	Transmission Line Modelling
UTLM	Unstructured Transmission Line Modelling
ABC	Absorbing Boundary Condition
PML	Perfectly Matched Layer
SC	Stretched Coordinate
UPML	Uniaxial Perfectly Matched Layer
SCN	Symmetrical Condensed Node
HSCN	Hybrid Symmetrical Condensed Node
SSCN	Super Symmetrical Condensed Node
CFS	Complex Frequency Shifted
TE	Transverse Electric
TM	Transverse Magnetic
TL	Transmission Line
PEC	Perfect Electric Conductor
JC	Jerusalem Cross
FSS	Frequency Selective Surface
PBC	Periodic Boundary Conditions

Contents

1	Introduction	1
1.1.	Computational Electromagnetics Methods	1
1.2.	Criteria for Effective Absorbing Boundary Conditions.....	5
1.3.	A Performance Appraisal of ABCs developed in TLM	7
1.4.	Research Aim	9
1.5.	Research Methodology	10
1.6	Outline of the Thesis	11
	References.....	12
2	The Perfectly Matched Layer	16
2.1	The Classical PML Equations	16
2.1.1	Split-field PML.....	17
2.1.2	The Uniaxial PML	25
2.1.3	The Stretched Coordinate PML	27
2.2	PML Advances.....	28
2.3	Limitations Of The PML.....	31
	References.....	34
3	Stretched-Coordinate PML in 2D TLM	39
3.1.	Introduction.....	39
3.2.	TLM Theory.....	41
3.2.1	TLM Shunt Node	43
3.2.2	TLM Series Node.....	48
3.2.3	Scatter and Connect Algorithms	50
3.2.4	Modelling Boundaries in TLM	54
3.3.	Stretched Coordinate PML Formulation in 2D TLM.....	55
3.3.1.	Modified Scatter and Connect Algorithm	59
3.3.2.	Fields in the Mapped Shunt Node PML	63
3.3.3.	Implementation Details	65
3.3.4.	Numerical Results	66
3.3.4.1	Influence of the PML conductivity profile	68
3.3.4.2	Influence of the number of PML layers NPML	71
3.3.4.3	Reflection Performance of the Mapped Shunt Node PML in Lossy and Dielectric Media	72

3.3.4.4	Comparison with Published 2D TLM-PML Schemes	73
3.3.4.5	Topical 2D Application: Scattering from NACA0015 Airfoil.....	74
3.4	Summary	76
	References.....	77
4	A Complex Domain Mapping of the SCN	80
4.1.	Introduction.....	80
4.2	The Symmetrical Condensed Node.....	82
4.2.1	SCN General Constitutive Relations	83
4.2.2	Scatter and Connect Algorithms	88
4.3	The Mapped SCN-PML	90
4.3.1	Modified Scatter Algorithms	96
4.3.2	Full Scatter Equations: 12-port Mapped SCN-PML	97
4.3.3	Full Scatter Equations: 15-port Mapped HSCN-PML.....	102
4.3.4	Modified Connect Algorithms	106
4.4	Summary.....	106
	References.....	107
	Appendix 4A – Definition of the total voltage V_j^{HSCN} in the mapped HSCN-PML	109
	Appendix 4B – Definition of the voltage $V_{ij}^{HSCN} \equiv Z_{ij} I_k^{HSCN}$ in the mapped HSCN-PML	111
5	Performance Characterization of the Mapped SCN-PML.....	112
5.1	Performance Of The Mapped SCN-PML For Normally Incident Waves.....	112
5.1.1	Influence Of The Conductivity Profile On The Mapped SCN-PML For Normally Incident Waves	114
5.1.2	Influence Of The Number Of PML Layers On The Mapped SCN-PML For Normally Incident Waves	118
5.2	Performance Of The Mapped SCN-PML For Oblique Wave Incidence	121
5.2.1	Influence Of The Conductivity Profile On The Mapped SCN-PML For Oblique Incidence Propagation	122
5.2.2	PML Tuning.....	124
5.3	Stability Of The Mapped SCN-PML	130
5.4	Summary	134
	References.....	136
6	Mapped SCN-PML in Practical Electromagnetic Simulations	138
6.1	Planar Periodic Structures	138

6.1.1 Simulation Setup.....	141
6.1.2 Numerical Results.....	142
6.2 Radiation and Scattering Applications	148
6.2.1 Metallic scatterer	149
6.2.2 Antenna Coupling	152
6.3. Inhomogeneous Media	156
6.4 Summary.....	160
References.....	161
7 Conclusions.....	163
7.1 Summary of the Work.....	163
7.2 Future Work.....	168
References.....	169

Chapter 1

Introduction

This chapter provides an introduction to the work carried out in this thesis and discusses the significance of effective computational domain truncation techniques. An appraisal of the absorbing boundary conditions implemented in TLM is provided which highlights the long standing issue of an ineffective domain truncation method. The research aims and methodology are briefly discussed. Finally the content of this thesis is outlined.

1.1. Computational Electromagnetics Methods

Since the mid-sixties, Computational Electromagnetics (CEM) has progressively emerged as the prominent scientific discipline concerned with studying electromagnetic (EM) field interaction in a variety of material and geometrical environments. This development has predominantly been driven by the availability of increasingly powerful computers as well as the growing complexity of real world applications. Before the advent of digital computers analytical methods were the preferred method to infer the EM response of physical systems. Through these an in-depth understanding of the problem at hand could be readily obtained therefore providing new insights on the physical phenomena involved. However, analytical techniques could only be applied to simplified structures, and although these methods are in itself of high accuracy their applications is limited. With the advent of personal computers came the development of sophisticated algorithms and tools which elicit the numerical solving of complex mathematical equations. The numerical approach employed by CEM therefore opens the door to deepening our understanding of electromagnetic problems with complexities that are rendered too difficult to be solved

directly. This has in turn enabled evaluations of such systems under adaptable conditions thus yielding performance and costs optimizations.

The broad scope of CEM techniques consists of numerical methods which solve Maxwell's equations in the differential or integral form. Each group can be further categorized based on the domain upon which the solutions are obtained, i.e. time domain or frequency domain. The main attractions of time domain methods over their frequency based counterpart are their suitability to transient problems as well as high computational efficiency gained when applied to wideband problems since the EM response over a range of frequencies can be obtained from a single simulation.

The integral equation (IE) based CEM methods are formulated based on deriving a Green's function which encapsulates the problem specific properties i.e. geometry, medium material, initial and boundary conditions. Radiation boundary conditions are therefore implicitly included in the formulation which makes them suitable for modelling problems with open boundaries for example an antenna on a platform or in the free space. In most cases, the computational burden incurred is low since discretization is only required on the sources of electromagnetic fields in the domain. A popular IE based method is the Boundary Element Method (BEM) which is also referred to as Method of Moments (MOM) [1.1], [1.2]. The BEM method involves casting Maxwell's equations into a "boundary-only" integral form from which numerical solutions can thus be obtained at the desired points in the solution space. The BEM is generally used to validate results from other numerical techniques. Whilst it is considered to be efficient in the modelling of problems with small surface to volume ratios, its main limitation is the inability to model field scattering from inhomogeneous media [1.2].

In contrast to IE methods, differential equation (DE) methods are derived directly from Maxwell's curl equations and therefore require little analytical pre-processing. They rely on a spatial discretization of the entire problem for which field samples are therefore obtainable at all points in space. This makes them suitable for the modelling of structures with complex geometrical and material features . Popular

DE based techniques include the Finite Difference Time-Domain (FDTD) method [1.1], [1.3], the Finite Element Method (FEM) [1.4], and the Transmission Line Modelling (TLM) method [1.1],[1.5],[1.6].

The FDTD method employs a direct centered difference approximations on the space and time derivatives of Maxwell's curls equations [1.1],[1.3]. This finite difference approximation is applied on staggered grids (Yee cells) to compute each component of the electric and magnetic vector fields. The computation of the fields are carried out using a leapfrog algorithm where, for example, the magnetic field components are computed first followed by electric field components. Conceptually this means that they are solved at different points in time. Both fields are also shifted in space by half a discretization step Δl . To ensure stability of the FDTD method the time step Δt is limited by the courant-stability criteria which for a uniform computational domain is given as [1.1],[1.3]

$$\Delta t \leq \frac{\Delta l_{min}}{c\sqrt{3}} \quad (1.1)$$

where c is the speed of light and Δl_{min} is the smallest mesh size modelled in the computational domain. According to (1.1) the overall computational time is thus significantly impacted by the choice of mesh grid. Whilst the classical FDTD method is capable of simulating complex geometry however the use of structured grids gives rise to stair casing approximations when modelling curved boundaries which reduces the accuracy of the solution obtained. An unstructured FDTD mesh implementation was recently proposed which employed the use of a hybrid primal mesh containing tetrahedral and hexahedral cells [1.7]. Although improvements in the computational efficiency was shown to be attainable with this approach however instabilities were also reported which were shown to be independent on the choice of the timestep.

The key attribute of frequency/time domain FEM [1.1],[1.4] technique is its capability to efficiently model curved geometries through the use of tetrahedral spatial discretization. This makes achieving accurate geometry representation attainable since each tetrahedral element can be individually scaled to fit the problem at hand.

Following the discretization the algorithm reduces the problem to a system of simultaneous linear equations which are then solved using efficient techniques for sparse matrices based on either direct methods or iterative methods. Whilst the flexibility of the element shapes is a key advantage of FEM, this however increases the complexity of discretization process, much more than the simple case of rectangular discretization. Furthermore, the presence of sliver triangles can also affect the accuracy and the stability of the method.

The time domain TLM method [1.5], whose continued development is the subject of this thesis, has extensively been demonstrated as an attractive and widely used method in simulating a large variety of EM problems. First introduced in 1971 by Johns and Beurle [1.6], the TLM method solves Maxwell's differential equations by mapping them to an equivalent, albeit approximate, set of transmission line equations for which exact solutions can be obtained. The physical propagation of EM waves is modelled by mapping the voltage and current pulses propagating on a network of interconnected transmission lines to electric and magnetic fields propagating in space. The temporal evolution of the fields is achieved by alternative scatter and connect operations, where incident voltages are scattered at the nodes that connect transmission lines and propagate to the adjacent nodes as incident voltages in the next time step. A key attraction of the TLM formulation is the guarantee of an unconditionally stable algorithm which is derived from the absence of the use of discrete differential operators in its development [1.6]. In contrast with FEM [1.4] and FDTD [1.3], the stability of the TLM algorithm is provable on a cell by cell basis and does not require an eigen analysis computation on the whole mesh.

It is important to note that no single numerical method is optimized for all problem cases. The choice of the specific technique employed is dependent on its suitability to the problem under study in relation to a number of important factors. For example, the accuracy attainable, ability to handle complex geometries and complex materials and the overall computational costs [1.1].

1.2. Criteria for Effective Absorbing Boundary Conditions

Differential numerical methods rely on a volumetric discretization of the problem domain which allows a realistic one to one mapping of geometric regions to discrete cells. However, due to the finite resources of computers the computational domain must be terminated. For problems involving naturally closed boundaries suitable boundary conditions can easily be applied on the edges of the computational domain e.g. magnetic or electric walls. A challenge however arises in truncating the computational domain of simulations involving waves propagating outwardly in unbounded regions e.g. an antenna radiating in free space. This can be physically interpreted as translating an infinite domain problem to a finite domain problem. An appropriate handling of such problems is a nontrivial task which if poorly attempted can result in the computation of inaccurate field solutions.

Over the years, several numerical schemes have been explored to truncate computational domains. These techniques, which are generally classified as absorbing boundary conditions (ABCs), are typically enforced at the edges of the computational domain to emulate an infinite computational space. A significant reduction in the size of the computational domain can therefore be attained, thus substantially improving the overall computational efficiency whilst maintaining high accuracy.

The effectiveness of an ABC is decided according to the following set of criteria:

- i. Strength of absorption of incident waves.
- ii. Guarantee of temporal numerical stability.
- iii. Geometric flexibility and application to wide variety of configurations.
- iv. Low computational costs – runtime and memory.
- v. Conceptual simplicity and ease of implementation.

vi. Ease of incorporation into legacy codes.

Intuitively, factors (i) and (ii) are considered as the principle criteria for determining an ABC's effectiveness since they directly influence the accuracy of the solutions computed in the interior domain. To mitigate the unavoidable numerical reflections which are generated at the interface between the medium and ABC, a highly absorbing ABC must be employed, one which particularly supports a total transmission for all frequencies, incident angles, and polarization of impinging propagating waves as well as for evanescent waves. Furthermore, the high absorption quality should not depend on the material properties of the interior domain, i.e. to the presence of lossy or anisotropic materials.

The stability of any numerical procedure is critical to obtaining meaningful results, and is a highly desired quality in an ABC. It is important to ensure that the stability performance of an already strongly stable CEM scheme is not compromised upon the integration of an ABC.

Factors (iii)-(vi) are the practical factors considered by the CEM worker, and whilst these inherently do not affect the quality of the solutions computed, they in turn influence the usability of a given CEM algorithm. They include conditions for high computational efficiency, in terms of runtime and memory usage, as well as the ease of implementation and incorporation into extant codes. In addition, the geometric flexibility of an ABC is a desirable quality. This benefit is especially realized in large scale EM scattering problems involving objects with complex geometric configurations for which additional computational whitespace would be otherwise required to obtain accurate results [1.8],[1.9].

It is true to say that no single method has been developed which meets all the criteria outlined above. Majority of the ABCs developed perform excellently in the continuous theory but deteriorate upon implementation into discrete models.

This thesis is focused on development of an effective domain truncation technique for the TLM method. Therefore, in the next section the performance of the ABCs developed in TLM method shall be reviewed in terms of their overall effectiveness. This review shall highlight a longstanding yet important problem in TLM which is the lack of a sufficiently stable, highly accurate and computationally practical ABC. Hence, the main concern of this thesis is the address of this crucial problem.

1.3. A Performance Appraisal of ABCs developed in TLM

In the TLM method, the simplest approach to simulating open boundary problems involves terminating the transmission line mesh with the intrinsic characteristic impedance of the medium modelled by the mesh [1.5]. In the literature, this method is referred to as the matched termination or matched boundary. It is still commonly employed in TLM simulations due to its simplicity, unconditional stability and effectiveness in absorbing waves incident on the boundary from a near normal angle. A limitation with the matched boundary ABC, however, is its poor absorption of oblique incidence waves. To address this the variable impedance boundary condition VIBC [1.10] was developed which was based on varying the impedance of the mesh boundary to match the analytically predicted impedance of an incoming plane wave therefore obtaining reflection coefficient equal to zero. Whilst the VIBC obtained better accuracy than the matched boundary ABC its performance is heavily reliant on the accuracy of the prediction algorithm and its success is also limited to applications involving plane wave propagation.

Global ABCs have been implemented in TLM. These aim to implement the exact absorbing boundary conditions and as such the field solutions are a function of the past time-history as well as the field solutions in the whole computational domain. For this reason significantly high accuracy is attainable. The most popular of these was demonstrated for the 3D TLM symmetrical condensed node based on the Johns Matrix technique [1.11],[1.12]. This involved precomputing the discrete Greens

function (impulse response) for each node on the boundary and performing a convolution during the TLM simulation with each incident wave at the node. Although these guarantee stability and demonstrate an ability to perfectly absorb outgoing waves, they are computationally impractical due to the high computational expense incurred. Compared to global ABCs, the computational demand of local ABCs are significantly lower since only the fields in the vicinity of the boundary plane are required to implement the absorption condition.

The development of local ABCs has been explored in 2D and 3D TLM. Amongst the proposed local ABCs the techniques derived from Engquist-Majda [1.13] one wave equations gained the most popularity because of their simplicity. These techniques were based on employing rational approximations of pseudo-differential operators. Such approximations include the use of Taylor or Padé approximants [1.14]. A TLM implementation of the Engquist-Majda's one-way wave equation [1.13] was implemented in [1.15]. The formulation demonstrated that the second order Padé approximation of one-way conditions was sufficient in terminating 3D TLM geometries however its performance was poor in the 2D case. In the same work the relationship between the stability and the order of truncation of the one-way wave equation and discrete boundary conditions were also investigated. The results showed that higher order boundary conditions (with orders greater than 2) introduced instabilities in both methods, this conclusion was found to be consistent with those reported by Higdon in [1.16]. The performance of analytical ABCs based on Higdon's absorbing condition and Taylor's expansion algorithm was compared in [1.17]. The validity of both methods was demonstrated by computing the reflection coefficient in an infinite rectangular waveguide. The results obtained show that reflection coefficients lower than -35 dB is attainable across the bandwidth of operation with both ABCs. Similar to the ABCs based on the one-way wave equation, instabilities were also reported for which various design suggestions were provided to attain an improved stability performance. Of all the analytical ABCs demonstrated in TLM the Super Absorbing Boundary Condition (SABC) proposed by [1.18] demonstrated an improvement in the accuracy, stability and computational efficiency when applied to Higdon ABC. Nonetheless, a major drawback with local ABCs methods is their weak absorption of near-grazing incident waves and inability to absorb evanescent waves,

such that most reflect completely the evanescent fields. Under such circumstances, the ABCs must be placed at a considerable distance (approximately 2 wavelengths) away from the region of interest, in order that the evanescent fields decrease naturally to a sufficiently small level. Local ABCs are therefore considered to be ineffective in practical applications.

A non-analytical physical ABC can be derived by appending a lossy media to the edges of the computational domain. This results in the attenuation of outgoing propagating waves according to the medium's conductivity and thickness. The obvious limitation with this approach is the high reflections expected at the boundary interface due to the impedance mismatch. The perfectly matched Layer (PML) [1.19],[1.20] addresses this limitation by matching the impedance of an absorption layer with the interior media. Originally demonstrated in the FDTD method [1.20] through a splitting of fields, reflections below -120 dB was shown to be attainable for wide angles, frequency and polarization of incidence waves. An additional attraction of the PML is its conceptual simplicity and the ease of integration into legacy CEM codes. The success and simplicity of the PML has encouraged different revisions and extensions of the original proposal and has resulted in various formulations beyond the initial FDTD technique [1.21]-[1.27]. Compared to the numerously developed FDTD PML formulations, only a handful of formulations have been proposed for TLM method [1.24]-[1.28] all of which to some degree demonstrate the PMLs capability to truncate TLM mesh. The performance of these schemes are properly demonstrated in several applications in Chapter 6. Nonetheless, a critical limiting factor with TLM-PML formulations is the weak temporal stability reported which severely limits its application in a broad class of problems [1.24]-[1.28].

1.4. Research Aim

It is now generally recognized that the PML, once optimized, can yield significant improvements to the overall performance of CEM simulations compared to other local ABCs. It is imperative that such benefits are also realized in the TLM method. Developing a stable and efficient TLM-PML formulation however presents a unique challenge for TLM developers. Unlike the finite difference method where

differential operators are straightforwardly discretized by central-differencing approximations, the TLM method relies on the derivation of a suitable circuit to field equivalence in the PML medium which, in a similar fashion to the classical TLM development, ensures an unconditionally stable algorithm. This thesis therefore aims to implement a PML formulation in 2D and 3D TLM simulations which demonstrates improved effectiveness and temporal stability in a broad class of electromagnetic applications. Particular consideration is made on the implementation approach taken in order to address the issues relating to the weak temporal stability demonstrated by previously developed TLM-PML schemes [1.24]-[1.28].

1.5. Research Methodology

Many mathematical equations reveal new interesting insights and capabilities on the underlying physical phenomena upon a transformation of coordinate systems. For this reason coordinate transformation techniques have long been explored in the mathematical analysis of a variety of engineering problems. In computational electromagnetics, complex domain displacements are widely utilized as a method to manipulate electromagnetic fields [1.29]-[1.31]. An example application of this methodology, one which is of interest in achieving the research aims, is the Stretched Coordinate (SC) PML formulation [1.21],[1.31]-[1.33] which achieves the reflectionless attenuation of propagating waves through an analytical continuation of Maxwell's equations solutions from real to complex space. Compared to other PML formulations (e.g. anisotropic/Uniaxial[1.23] and split-field PML [1.20]), the SC PML theory offers a more mathematically rigorous definition of the PML theory which has motivated its easy extension to curvilinear coordinates and conformal mesh terminations [1.32], [1.33]. Further motivated by its suitability to general media the SC PML theory will be basis of the TLM-PML formulation developed in this thesis.

The choice of the approach taken in implementing the PML is strongly influenced by the particular nature of the numerical method in which it is being deployed. Therefore, in order to maintain the efficacy of the TLM algorithm, the PML equation to be discretized must lend itself well to being mapped to an equivalent transmission line model. Ensuring this enables the derivations of suitable equivalent

field to circuit representations for the PML medium. This approach to a TLM-PML implementation avoids the direct discretization of the PML equations as employed by previously proposed TLM-PML schemes, and follows more closely to the classical mapping of wave equations to equivalent transmission line quantities thus ensuring an unconditionally stable algorithm.

1.6 Outline of the Thesis

The remainder of the thesis is organized as follows. Chapter 2 presents the PML theory from the split-field, stretched coordinate and anisotropic interpretations. The advances in the PML formulation are discussed as well as the limitations of the PML in both the continuous and discrete settings.

Chapter 3 introduces the TLM theory through the 2D shunt and series node where an analogy with the second-order wave equation is derived. Subsequently, a new framework for implementing the second-order stretched coordinate PML equations in TLM will be formulated for the 2D TLM shunt node. The proposed TLM-PML scheme is formulated based on mapping the second-order stretched coordinate PML equations to a suitable set of transmission line equations. This method is referred to as the mapped TLM-PML and when applied within the context of the shunt node it is specifically referred to as the mapped shunt-node PML. The effectiveness of the mapped shunt-node PML is investigated through a rectangular waveguide application. In particular the influence of the PML parameters on the reflection coefficient shall be demonstrated for a particular case of an infinitely long rectangular waveguide.

In Chapter 4, the TLM theory in the 3D setting is presented through the Symmetrical Condensed Node (SCN). Subsequently the theory of mapped TLM-PML framework described in Chapter 3 is extended to the SCN. Extensions to hybrid SCN (HSCN) nodes are also presented. When applied in this context the mapped TLM-PML is specifically referred to as the mapped SCN-PML or mapped HSCN-PML, respectively.

Chapters 5 and 6 demonstrate the formulation developed in Chapter 4 in a variety of 3D TLM problems, namely: the simulation of planar-periodic structures, radiation and scattering applications and in terminating materially inhomogeneous domains. A performance comparison with previously proposed split-field TLM-PML formulations [1.24],[1.25] and the matched boundary will be made where the superior temporal stability of the mapped SCN-PML will be demonstrated.

A summary of the work carried out in this thesis is presented in Chapter 7 followed by a discussion on further work.

References

- [1.1] T. Rylander, P. Ingelstrom, A. Bondeson, Computational Electromagnetics Springer Press, 2013.
- [1.2] R. F. Harrington, Field Computation by Moment Methods. New York: McMillan, 1968.
- [1.3] A. Taflove and S. C. Hagness, Computational Electrodynamics: the Finite Difference Time-Domain Method, 3rd ed. Norwood MA: Artech House, 2005.
- [1.4] J. Jin, The finite element method in electromagnetics. John Wiley & Sons, 1993.
- [1.5] C. Christopoulos, The Transmission-Line Modelling Method TLM. IEEE Press, 1995.
- [1.6] P. B. Johns, and R. L. Beurle, "Numerical solution of two dimensional scattering problems using a transmission line matrix", Proc. IEE,118,(9), pp. 1203-1208, 1971.
- [1.7] Gansen, M. El. Hachemi, S. Belouettar, *et al.*, "A 3D Unstructured Mesh FDTD Scheme for EM Modelling" *Arch Computat Methods Eng* **28**, 181–213, 2021.
- [1.8] L. C. Kempel and J. L. Volakis, "Conformal ABC's in radiation problems", 1994 URSI Radio Sci. Meeting Dig., pp. 166, 1994-June.
- [1.9] F. Teixeira, and W. Chew, "Analytical derivation of a conformal perfectly matched absorber for electromagnetic waves," *Microwave and Optical technology letters*, vol. 17, no. 4, pp. 231-236, 1998.

- [1.10] N.R.S Simons and E. Bridges, "Method for modelling free space boundaries in TLM situations," *Electron. Lett.*, vol. 26, pp. 453–455, 1990.
- [1.11] W.J.R. Hoefer, "The Discrete Time Domain Green's Function or Johns Matrix - A New Powerful Concept in Transmission Line Modeling (TLM)", *Int. J. of Nunt. Modeling*, vol. 2 pp. 215-225, 1989.
- [1.12] M. Righi and W. J. R. Hoefer, "Modal Johns matrices for waveguide components," in *Proc. 1st Int. Workshop Transmission Line Modeling (TLM)*, Victoria, B.C., Canada, Aug. 1–3, pp. 233–236, 1995.
- [1.13] B. Engquist and A. Majda, "Absorbing boundary conditions for the numerical simulation of waves," *Math. Comp.*, vol. 31, pp. 629-651, 1977.
- [1.14] A. Iserles, "A note on Pade approximation and generalized hypergeometric functions," *BIT*, v. 19, pp. 543-545, 1979.
- [1.15] J. A. Morente, J. A. Porti, and M. Khalladi, "Absorbing boundary conditions for the TLM Method," *IEEE Trans. Microwave Theory Tech.*, vol. 40, pp. 2095-2099, Nov. 1992.
- [1.16] R. L. Hidgon, "Absorbing boundary conditions for difference approximations of the multi-dimensional wave equation," *Math. Comp.*, vol. 47, pp. 437-459, Oct. 1986.
- [1.17] Z. Chen, M. M. Ney, and W. J. R. Hoefer, "Study of absorbing boundary conditions in the 3D-TLM symmetrical condensed node model," *MTT Symp. Dig.*, Albuquerque, NM, pp. 369-372, 1992.
- [1.18] N. Kukutsu and R. Konno, "Super absorption boundary condition for guided waves in the 3-D TLM simulation," *IEEE Microwave Guided Wave Lett.*, vol. 5, pp. 299–301, Sept. 1995.
- [1.19] J-P. Bérenger, *Perfectly Matched Layer (PML) for Computational Electromagnetics*, Morgan & Claypool publishers, 2007.
- [1.20] J-P. Bérenger, "A perfectly matched layer for the absorption of electromagnetic waves", *J. Comput. Phys.*, 114, (1), pp. 185–200, 1994.
- [1.21] W. C. Chew and W. H. Weedon, "A 3D perfectly matched medium from modified Maxwell's equations with stretched coordinates," *Microwave and Optical Tech. Lett.*, vol. 7, no. 13, pp. 599–604, 1994.

- [1.22] Z.S Sacks, D.M. Kingsland, R. Lee , J.F Lee,,: ‘A perfectly matched anisotropic absorber for use as an absorbing boundary condition’, IEEE Trans. Antennas and Propagation, 43, (12), pp. 1460–1463,1995.
- [1.23] S. Gedney,”An anisotropic PML for FDTD simulation of fields in lossy dispersive media”, Electromagn.,16, (3), pp.339-416,1996.
- [1.24] L. Maguer, and M. M. Ney, “Extended PML-TLM node: an efficient approach for full waveanalysis of open structures.” Int. J. Numer. Model, vol. 14, pp. 129–144, 2001.
- [1.25] J. L Dubard, and D. Pompei “Optimization of the PML efficiency in 3-D TLM method.” IEEE Transactions on Microwave Theory and Techniques; 48(7):1081–1087, 2000.
- [1.26] T. W. Kang, C. Christopoulos, and J. Paul, “Implementation of the stretched coordinate-based PML for waveguide structures in TLM”. International journal of numerical modelling electronic networks. Devices and fields. vol. 18, pp. 107-118, 2005.
- [1.27] C., Eswarappa, W.J.R.: Hofer, ‘Implementation of Bérenger absorbing boundary conditions in TLM by interfacing FDTD perfectly matched layers’, Electron. Lett. 31, (15), pp. 1264-1266, 1995.
- [1.28] N. Pena, M.M. Ney, “A new TLM node for Berenger’s perfectly matched layer”, IEEE Microwave and Guided Wave Lett., 6, (11), pp. 410-412, 1996.
- [1.29] B.-I. Popa and S. A. Cummer, “Complex coordinates in transformation optics,” Phys. Rev. A, vol. 84, 063837, 2011.
- [1.30] L. Felsen, “Complex-source-point solutions of the field equations and their relations to the propagation and scattering of Gaussian beams,” *Symp. Mathem.* **18**, p. 39-56, 1975.
- [1.31] F. L. Teixeira and W. C. Chew, “Complex space approach to perfectly matched layers: A review and some new developments,” Int. J. Numer. Model., vol. 13, pp. 441–455, 2000.
- [1.32] F. L. Teixeira and W. C. Chew, “Differential forms, metrics, and the reflectionless absorption of electromagnetic waves,” J. Electromagn. Waves Appl., vol. 13, no. 5, pp. 665–686, 1999

- [1.33] F. L. Teixeira and W. C. Chew, “Systematic derivation of anisotropic PML absorbing media in cylindrical and spherical coordinates,” *IEEE Microw. Guided Wave Lett.*, vol. 7, pp. 371–373, 1997.

Chapter 2

The Perfectly Matched Layer

This Chapter introduces the classical PML formulations namely the split-field, stretched coordinate and anisotropic approach. The advances in the PML formulation are also discussed as well as the limitations of the PML in both the continuous and discrete settings.

2.1 The Classical PML Equations

Since its first introduction in 1994, the PML has continually been recognized as the most effective and thus most widely employed domain truncation technique. The original split-field theory proposed by Berenger has been adapted and reformulated in a variety of ways. Nonetheless, in theory all PML interpretations demonstrate the following core properties [2.1]: i) an artificial medium surrounds the interior problem space, ii) a perfect transmission is achieved at the medium-to-PML interface (i.e. no reflections) for all incident angles and frequencies, and iii) all incident waves can be attenuated to a near zero value.

The focus of this thesis is the development of an effective PML implementation for the TLM method. In order to describe the discrete implementation proposed it is necessary to first describe the PML equations in the continuous setting. In this section the classical PML theory will thus be described. First, the details of original PML theory will be presented followed by the subsequent formulations which

were developed shortly afterwards. Section 2.2 will detail some of the key PML advances/extensions. For completeness, the chapter will conclude by discussing the limitations of the PML in the continuous and discrete space.

2.1.1 Split-field PML

All classical electromagnetic behavior can be described by Maxwell's equations which in the differential form are given as [2.2],

$$\nabla \cdot \bar{\bar{\epsilon}} \mathbf{E} = \rho, \quad (2.1a)$$

$$\nabla \cdot \bar{\bar{\mu}} \mathbf{H} = 0, \quad (2.1b)$$

$$-\nabla \times \mathbf{E} = \bar{\bar{\mu}} \frac{\partial \mathbf{H}}{\partial t} + \bar{\bar{\sigma}}_m \mathbf{H}, \quad (2.1c)$$

$$\nabla \times \mathbf{H} = \bar{\bar{\epsilon}} \frac{\partial \mathbf{E}}{\partial t} + \bar{\bar{\sigma}}_e \mathbf{E}, \quad (2.1d)$$

where \mathbf{E} and \mathbf{H} , represent the vectors of the electric field and magnetic field, respectively, $\bar{\bar{\mu}}$, $\bar{\bar{\epsilon}}$, $\bar{\bar{\sigma}}_m$ and $\bar{\bar{\sigma}}_e$ respectively are the permeability, permittivity and magnetic and electric conductivity tensors of the medium, and ρ is the total electric charge density.

Assuming a free space medium with anisotropic losses in Cartesian coordinates, the equations in (2.1c) and (2.1d) are fully expanded as:

$$\begin{aligned} \frac{\partial H_z}{\partial y} - \frac{\partial H_y}{\partial z} &= \epsilon_0 \frac{\partial E_x}{\partial t} + \sigma_{e_x} E_x, \\ \frac{\partial H_x}{\partial z} - \frac{\partial H_z}{\partial x} &= \epsilon_0 \frac{\partial E_y}{\partial t} + \sigma_{e_y} E_y, \\ \frac{\partial H_y}{\partial x} - \frac{\partial H_x}{\partial y} &= \epsilon_0 \frac{\partial E_z}{\partial t} + \sigma_{e_z} E_z. \end{aligned} \quad (2.2a)$$

$$\begin{aligned}
 \frac{\partial E_z}{\partial y} - \frac{\partial E_y}{\partial z} &= -\mu_0 \frac{\partial H_x}{\partial t} - \sigma_{m_x} H_x, \\
 \frac{\partial E_x}{\partial z} - \frac{\partial E_z}{\partial x} &= -\mu_0 \frac{\partial H_y}{\partial t} - \sigma_{m_y} H_y, \\
 \frac{\partial E_y}{\partial x} - \frac{\partial E_x}{\partial y} &= -\mu_0 \frac{\partial H_z}{\partial t} - \sigma_{m_z} H_z,
 \end{aligned} \tag{2.2b}$$

As its name suggests, the split-field PML involves splitting the field components into two subcomponents where the time evolution of each subcomponent is related to the spatial variations of other dual field components. The field splitting is thus given as

$$\begin{aligned}
 E_x &= E_{xy} + E_{xz}, & H_x &= H_{xy} + H_{xz}, \\
 E_y &= E_{yx} + E_{yz}, & H_y &= H_{yx} + H_{yz}, \\
 E_z &= E_{zx} + E_{zy}, & H_z &= H_{zx} + H_{zy},
 \end{aligned} \tag{2.3}$$

which upon substitution into (2.2a) and (2.2b) results in a total of 12 equations where independent conductivities are applied to the resulting subfield components. This obtains the following re-expression of (2.2a) and (2.2b),

$$\epsilon_0 \frac{\partial E_{xy}}{\partial t} + \sigma_y E_{xy} = \frac{\partial (H_{zx} + H_{zy})}{\partial y}, \tag{2.4a}$$

$$\epsilon_0 \frac{\partial E_{xz}}{\partial t} + \sigma_z E_{xz} = -\frac{\partial (H_{yz} + H_{yx})}{\partial z}, \tag{2.4b}$$

$$\epsilon_0 \frac{\partial E_{yz}}{\partial t} + \sigma_z E_{yz} = \frac{\partial (H_{xy} + H_{xz})}{\partial z}, \tag{2.4c}$$

$$\epsilon_0 \frac{\partial E_{yx}}{\partial t} + \sigma_x E_{yx} = -\frac{\partial (H_{zx} + H_{zy})}{\partial x}, \tag{2.4d}$$

$$\epsilon_0 \frac{\partial E_{zx}}{\partial t} + \sigma_x E_{zx} = \frac{\partial (H_{yz} + H_{yx})}{\partial x}, \tag{2.4e}$$

$$\epsilon_0 \frac{\partial E_{zy}}{\partial t} + \sigma_y E_{zy} = -\frac{\partial(H_{xy} + H_{xz})}{\partial y}, \quad (2.4f)$$

$$\mu_0 \frac{\partial H_{xy}}{\partial t} + \sigma_y^* H_{xy} = -\frac{\partial(E_{zx} + E_{zy})}{\partial y}, \quad (2.4g)$$

$$\mu_0 \frac{\partial H_{xz}}{\partial t} + \sigma_z^* H_{xz} = \frac{\partial(E_{yz} + E_{yx})}{\partial z}, \quad (2.4h)$$

$$\mu_0 \frac{\partial H_{yz}}{\partial t} + \sigma_z^* H_{yz} = -\frac{\partial(E_{xy} + E_{xz})}{\partial z}, \quad (2.4i)$$

$$\mu_0 \frac{\partial H_{yx}}{\partial t} + \sigma_x^* H_{yx} = \frac{\partial(E_{zx} + E_{zy})}{\partial x}, \quad (2.4j)$$

$$\mu_0 \frac{\partial H_{zx}}{\partial t} + \sigma_x^* H_{zx} = -\frac{\partial(E_{yx} + E_{yz})}{\partial x}, \quad (2.4k)$$

$$\mu_0 \frac{\partial H_{zy}}{\partial t} + \sigma_y^* H_{zy} = \frac{\partial(E_{xy} + E_{xz})}{\partial y}, \quad (2.4l)$$

where parameters $\sigma_x, \sigma_y, \sigma_z$ and $\sigma_x^*, \sigma_y^*, \sigma_z^*$ are the PML conductivities, which satisfy the impedance matching condition [2.1], [2.3]

$$\frac{\sigma_i}{\epsilon_0} = \frac{\sigma_i^*}{\mu_0}, \quad (i = x, y, z). \quad (2.5)$$

Since the split field formulation models the PML as a lossy medium the electric and magnetic conductivities employed in (2.2) can be replaced by the notations used in (2.4) representing the PML conductivity. In this manner the PML conductivities are thus used to achieve the desired field attenuation along the desired spatial direction. For example, the attenuation of the x polarised electric field along the y -axis E_{xy} is achieved using the conductivity σ_y .

Substituting the plane wave solution into (2.4), where the field subcomponents take the form,

$$\psi = \psi_0 e^{j\omega t} e^{-j(k_x x + k_y y + k_z z)}, \quad (2.6)$$

obtains 12 equations relating the angular frequency ω and the wave numbers k_x, k_y, k_z . For example, the first two equations in (2.4) yield

$$\omega \epsilon_0 \left(1 + \frac{\sigma_y}{j\omega \epsilon_0}\right) E_{0xy} = -k_y (H_{0zx} + H_{0zy}), \quad (2.7a)$$

$$\omega \epsilon_0 \left(1 + \frac{\sigma_z}{j\omega \epsilon_0}\right) E_{0xz} = k_z (H_{0yz} + H_{0yx}), \quad (2.7b)$$

From (2.7) the following parameter can be defined [2.10],

$$S_i = 1 + \frac{\sigma_i}{j\omega \epsilon_0}, \quad S_i^* = 1 + \frac{\sigma_i^*}{j\omega \mu_0} \quad (i = x, y, z). \quad (2.8)$$

Equations (2.7a) and (2.7b) can be merged into a single equation by first dividing both sides with S_y and S_z and by combining $E_{0x} = E_{0xz} + E_{0xy}$ and $H_{0z} = H_{0zx} + H_{0zy}$. By similarly applying this to (2.4c) – (2.4d) the following set is obtained,

$$\omega \epsilon_0 E_{0x} = -\frac{k_y}{S_y} H_{0z} + \frac{k_z}{S_z} H_{0y}, \quad (2.9a)$$

$$\omega \epsilon_0 E_{0y} = -\frac{k_z}{S_z} H_{0x} + \frac{k_x}{S_x} H_{0z}, \quad (2.9b)$$

$$\omega \epsilon_0 E_{0z} = -\frac{k_x}{S_x} H_{0y} + \frac{k_y}{S_y} H_{0x}, \quad (2.9c)$$

$$\omega\mu_0 H_{0x} = \frac{k_y}{S_y^*} E_{0z} - \frac{k_z}{S_z^*} E_{0y}, \quad (2.9d)$$

$$\omega\mu_0 H_{0y} = \frac{k_z}{S_z^*} E_{0x} - \frac{k_x}{S_x^*} E_{0z}, \quad (2.9e)$$

$$\omega\mu_0 H_{0z} = \frac{k_x}{S_x^*} E_{0y} - \frac{k_y}{S_y^*} E_{0x}. \quad (2.9f)$$

Given the following,

$$\mathbf{k}_s = \left(\frac{k_x}{S_x}, \frac{k_y}{S_y}, \frac{k_z}{S_z} \right), \quad (2.10a)$$

$$\mathbf{k}_s^* = \left(\frac{k_x}{S_x^*}, \frac{k_y}{S_y^*}, \frac{k_z}{S_z^*} \right), \quad (2.10b)$$

then (2.9) can be rewritten more compactly as

$$\epsilon_0 \omega \mathbf{E}_0 = -\mathbf{k}_s \times \mathbf{H}_0 \quad (2.11a)$$

$$\mu_0 \omega \mathbf{H}_0 = \mathbf{k}_s^* \times \mathbf{E}_0 \quad (2.11b)$$

where \mathbf{E}_0 and \mathbf{H}_0 are vectors of the components E_{0x}, E_{0y}, E_{0z} and H_{0x}, H_{0y}, H_{0z} respectively.

From (2.11) it is clear that the \mathbf{E} and \mathbf{H} fields are perpendicular and the wave vector \mathbf{k}_s is also perpendicular to both \mathbf{E} and \mathbf{H} , as is the case in a vacuum. Substituting \mathbf{H}_0 from (2.11b) into (2.11a) yields,

$$\epsilon_0 \mu_0 \omega^2 \mathbf{E}_0 = -\mathbf{k}_s \times (\mathbf{k}_s^* \times \mathbf{E}_0), \quad (2.12)$$

which according to vector identity $A \times (B \times C) = -C(A \cdot B) + B(A \cdot C)$ can be re-expressed as,

$$\epsilon_0 \mu_0 \omega^2 \mathbf{E}_0 = -(\mathbf{k}_s \cdot \mathbf{E}_0) \cdot \mathbf{k}_s^* + (\mathbf{k}_s \cdot \mathbf{k}_s^*) \cdot \mathbf{E}_0. \quad (2.13)$$

Since \mathbf{k}_s is perpendicular to the \mathbf{E} field, then $\mathbf{k}_s \cdot \mathbf{E}_0 = 0$ and (2.13) reduces to

$$(\epsilon_0 \mu_0 \omega^2 - \mathbf{k}_s \cdot \mathbf{k}_s^*) \mathbf{E}_0 = 0. \quad (2.14)$$

This results in the following expression for the dispersion,

$$\epsilon_0 \mu_0 \omega^2 = \frac{k_x^2}{S_x S_x^*} + \frac{k_y^2}{S_y S_y^*} + \frac{k_z^2}{S_z S_z^*}, \quad (2.15)$$

Equation (2.15) is the 3D equation of an ellipsoid which when solved with respect to the wave numbers obtains the following,

$$k_x = \frac{\omega}{c} \sqrt{S_x S_x^*} \sin\theta \cos\phi, \quad (2.16a)$$

$$k_y = \frac{\omega}{c} \sqrt{S_y S_y^*} \sin\theta \sin\phi, \quad (2.16b)$$

$$k_z = \frac{\omega}{c} \sqrt{S_z S_z^*} \cos\theta, \quad (2.16c)$$

here ϕ and θ show the orientation of \mathbf{k}_s .

By substituting (2.16) into the field solution in (2.5), the field subcomponents take the form,

$$\psi = \psi_0 e^{j\omega t} e^{-j\frac{\omega}{c}(x\sin\theta\cos\phi + y\sin\theta\sin\phi + z\cos\theta)} e^{-\frac{\sigma_x}{\epsilon_0 c} x\sin\theta\cos\phi} e^{-\frac{\sigma_y}{\epsilon_0 c} y\sin\theta\sin\phi} e^{-\frac{\sigma_z}{\epsilon_0 c} z\cos\theta} \quad (2.17)$$

Allowing ξ_x, ξ_y, ξ_z to be the angles that direction (ϕ, θ) forms with the axis of coordinates obtains a symmetrical expression for (2.17) given as,

$$\psi = \psi_0 e^{j\omega t} e^{-j\frac{\omega}{c}(x\cos\xi_x + y\sin\xi_y + z\cos\xi_z)} e^{-x\frac{\sigma_x}{\epsilon_0 c}\cos\xi_x} e^{-y\frac{\sigma_y}{\epsilon_0 c}\cos\xi_y} e^{-z\frac{\sigma_z}{\epsilon_0 c}\cos\xi_z} \quad (2.18)$$

Applying the PML impedance matching condition (2.5) on (2.8) results in $\mathbf{k}_s = \mathbf{k}_s^*$. Since the wave vector \mathbf{k}_s is perpendicular to both \mathbf{E} and \mathbf{H} then (2.11) can be written as,

$$\epsilon_0 \omega \|\mathbf{E}_0\| = \|\mathbf{k}_s\| \|\mathbf{H}_0\| \quad (2.19)$$

where $\|\cdot\|$ denotes the magnitude of the vector quantities.

Employing the relation in (2.15) and substituting into (2.19) obtains the impedance expression,

$$Z = \frac{\|\mathbf{E}_0\|}{\|\mathbf{H}_0\|} \quad (2.20)$$

i.e. the impedance in the PML medium is matched to the impedance of a vacuum.

Given the above derivations the following deductions can be made about the PML medium,

- i. The first 2 exponentials in (2.18) are similar to the waveform in a vacuum where the phase propagates in directions ξ_x, ξ_y, ξ_z with speed c , as is the case in a vacuum. It is also clear that the phase propagates perpendicular to the $\mathbf{E} - \mathbf{H}$ plane, as is the case in a vacuum.
- ii. By enforcing the matched impedance condition, the PML medium is matched to the vacuum. Therefore all incident waves are perfectly transmitted without any reflections.
- iii. The last three exponential terms in (2.18) contribute towards the attenuation of fields. It is clear that the attenuation along a particular axis-direction in the 3D PML is controlled by the value of conductivity set. For example, by setting $\sigma_x = \sigma_y = 0$ then the waves propagating along the x and y axis are not attenuated and only the waves propagating along the z direction are attenuated.

According to the above (and as more elaborately described in [2.1] and [2.3]), a plane wave incident on a PML layer with an arbitrary incident angle is perfectly transmitted across the PML medium without any reflections. Across the PML medium the wave experiences an attenuation along the directions as dictated by the attenuating terms in (2.18). Upon reaching the end of the PML medium, the residual wave is reflected back in the direction of the vacuum where a further attenuation is applied on the return path. The total reflection coefficient, for example in the z -direction, is given by,

$$R(\xi_z) = e^{-2L \frac{\sigma_z}{\epsilon_0 c} \cos \xi_z}, \quad (2.21)$$

where L is the PML thickness.

From (2.21) it is clear that the reduction of the total reflection can be achieved by choosing a wider PML medium or by setting a sufficiently high value of PML conductivity. Indeed, it is desirable to set the PML thickness to be as small as possible since this reduces the computational costs contributed from the PML region. For this reason, in the continuous space the PML conductivity is set such that the residual wave component will be sufficiently attenuated so that it has no real contributions to the behavior observed in the physical domain. This behavior is different to what is observed in the discrete space, as will be discussed in the later sections of this chapter.

An important thing to note about the split-field PML interpretation is the manner in which the PML theory is realized. By employing a field splitting Maxwells equations are modified into the form shown in (2.4). Although the split-field PML medium can be viewed as a physical lossy medium the formulation in itself results in non-Maxwellian fields due to the modification of Maxwells equations. In theory this has no significant impact on the performance. However any implementation in numerical methods requires substantial modification of the underlying algorithm. Further, the orthogonal field splitting restricts its implementation to structured grids systems which thus limits its general usability.

2.1.2 The Uniaxial PML

Several PML interpretations were proposed shortly after Berenger's ground breaking split-field theory. These were primarily developed to address some of the limitations of the split-field PML particularly its non-Maxwellian form and to allow for the PMLs extensions to general media. A popular Maxwellian PML interpretation is the anisotropic PML or also commonly referred to as the uniaxial PML (UPML)[2.4], [2.5] which was first demonstrated in the frequency domain finite element method (FEM). The UPML theory implements the PML theory as an anisotropic medium but with the field solution derived in (2.18) scaled by \mathbf{S}_i .

Nonetheless, the desired nonreflective behavior is yet preserved by setting $\mathbf{S}_i = \mathbf{S}_i^*$ [2.4].

The following set of equations define the frequency domain representation of the UPML,

$$\omega\epsilon_0\bar{\bar{\epsilon}}_s\mathbf{E}'_0 = -\mathbf{k}^* \times \mathbf{H}'_0 \quad (2.22a)$$

$$\omega\mu_0\bar{\bar{\mu}}_s\mathbf{H}'_0 = \mathbf{k} \times \mathbf{E}'_0 \quad (2.22b)$$

where \mathbf{E}'_0 and \mathbf{H}'_0 denote scaled field solutions i.e. ($\mathbf{E}'_0 = \mathbf{S}_i\mathbf{E}_0$ and $\mathbf{H}'_0 = \mathbf{S}_i^*\mathbf{H}_0$) and as a result of the matched condition i.e. $\mathbf{S}_i = \mathbf{S}_i^*$ the permittivity and permeability tensors $\bar{\bar{\epsilon}}_s$ and $\bar{\bar{\mu}}_s$ are given as,

$$\bar{\bar{\epsilon}}_s = \bar{\bar{\mu}}_s = \begin{bmatrix} \frac{S_y S_z}{S_x} & 0 & 0 \\ 0 & \frac{S_z S_x}{S_y} & 0 \\ 0 & 0 & \frac{S_x S_y}{S_z} \end{bmatrix} \quad (2.23)$$

The propagation characteristics of the transmitted wave of the UPML medium has been demonstrated to be identical to that of the split-field PML medium. This thus implies some form of physical equivalence exists between both formulations, the proof of this is detailed in [2.4]. The main advantage of the UPML formulation is the ease of implementation into any numerical method which supports the definition of diagonally anisotropic material tensors. This makes it very suitable for FEM applications.

2.1.3 The Stretched Coordinate PML

So far in this chapter the split-field and UPML theory have been introduced where the attenuation mechanism of both formulations have been described. Another popular PML interpretation is the Stretched Coordinate (SC) PML [2.1],[2.6]. This employs a non-physical approach through an analytic continuation of Maxwell's equations from real space to a complex space defined within the absorbing layer. The SC PML theory modifies Maxwells Equation in frequency domain into the following form,

$$j\omega\epsilon_0\mathbf{E} = -\nabla^s \times \mathbf{H}, \quad (2.24a)$$

$$j\omega\mu_0\mathbf{H} = \nabla^s \times \mathbf{E}, \quad (2.24b)$$

where ∇^s is the spatial differential operator in the complex stretched space, which is given as

$$\nabla^s = \left(\frac{\partial}{S_x \partial x}, \quad \frac{\partial}{S_y \partial y}, \quad \frac{\partial}{S_z \partial z} \right), \quad (2.25)$$

and S_x, S_y, S_z are the coordinate stretching factors defined according to (2.8).

By substituting the plane wave solution (2.5) into (2.24) the full set of equations in (2.9) can be obtained where the wave vectors are transformed as shown in (2.10) i.e. $\mathbf{k} \rightarrow \mathbf{k}_s$ and $\mathbf{k}^* \rightarrow \mathbf{k}_s^*$. The SC PML equations in (2.24) can thus be re-expressed as (2.11). In a similar manner to the derivation shown in (2.12) - (2.19) the plane wave solution to SC-PML is also given as in the split-field PML(2.18). This shows that the SC PML interpretation is equivalent to the split-field approach however both interpretations differ in their implementation. The coordinate stretching shown in (2.25) is applied along each axis and through this oscillating fields become the exponentially decaying fields shown in (2.18). Attenuation along the desired direction

is obtained by setting the corresponding PML conductivities σ, σ^* greater than zero. In a similar fashion to the split-field and UPML formulations the SC PML layer is also perfectly matched to the interfacing computational domain which is governed by the standard Maxwell's equations.

In its original form, as shown in (2.24), the SC-PML results in non-Maxwellian fields since the form of Maxwell's equation is modified. However, owed to the robustness of the formulation these non-Maxwellian fields can be mapped to a set of Maxwellian fields in an anisotropic medium representing the PML. The full derivation of the constitutive parameters for the Cartesian, cylindrical and spherical anisotropic PML media is presented in [2.7]. This demonstrates the equivalence between the UPML interpretation and SC-PML approach. The SC-PML offers a more elegant and mathematically rigorous interpretation of the PML and so it generalizes more easily to other wave equations, coordinate systems, and inhomogeneous media. This is the prime advantage of the SC-PML interpretation when compared to the other formulations presented.

2.2 PML Advances

To realize the benefit of the PML it must be applied to the simulation of unbounded wave propagation. A discrete representation of the continuous PML equations described in Section 2.1 is therefore sought suitable for implementation in a numerical method of choice. The first demonstration of the PML in the discrete setting was within the framework of FDTD method [2.3]. Due to the success shown it was quickly adapted for implementations in other numerical methods. Undoubtedly, to date, the PML usage is still more popularly used in FDTD due to the ease of implementation of the finite difference schemes as well as the superior absorption performance demonstrated.

It is worth noting that the SC PML interpretation has been the most instrumental in the PML extensions in numerical methods. The literature is abundant

on this subject, where the benefits of the PML have been realized in other domains of wave-physics beyond the electromagnetics domain [2.8]-[2.15].

Within the domain of electromagnetics the PML has been more popularly applied in finite difference and finite element methods. Some of the PML advances in both schemes are worth noting and are thus described below.

The classical PML theory which was designed to absorb planar electromagnetic waves was extended to cylindrical and spherical [2.16] coordinate systems shortly after its proposal. Indeed this was recognised as a major advancement since this extended the range of applicability of the PML. Nonetheless, employing a PML derived using these canonical coordinate systems was found to be less computationally efficient for most practical applications where a geometrically convex PML is required to minimize the so-called buffer region. To address this problem, the conformal PML [2.17] was proposed which adjusts the PML boundary shape according to the convex hull of the scatterer embedded in the computational domain. This way, the unwanted buffer region can be reduced and thus the memory requirement of simulation are reduced significantly. The conformal PML when deployed within an unstructured grid method yields a superior algorithm with improved geometry flexibility/handling. For this reason the most recent literature on the subject have been reported within the context of finite element-based methods [2.18]-[2.20].

To maximize the effectiveness of the PML, the PML media must match the interfacing physical media in the interior domain. The classical PML equations described in Sections 2.1 handle the simple case of terminating lossless vacuum or homogeneous dielectric media. To match more general media (i.e. either anisotropic, lossy or dispersive media) various re-formulations of equations (2.4), (2.22) and (2.24) have been proposed over the years. As previously mentioned, the split-field PML is modelled as a physical lossy medium and so the electric and magnetic conductivities are replaced by the PML conductivities (i.e. $\sigma_e \leftrightarrow \sigma$, $\sigma_m \leftrightarrow \sigma^*$) which are then used to achieve the necessary field attenuations. In practice this creates a challenge when

the split-field PML is required to match a lossy medium. A split-field PML capable of matching anisotropic and dispersive material has been demonstrated in [2.21] and [2.22], respectively. Both formulations failed to attract much attention because of the analytical effort involved since each anisotropic/dispersive material required unique PML constitutive parameters. On the other hand an extension of the SC-PML to match anisotropic and/or dispersive media (including lossy) with little analytical effort was demonstrated in [2.23]. Owing to the analytical continuation employed in the SC-PML the derivation shown in [2.23] revealed no conceptual difference from the dispersionless and isotropic case. This again highlights the benefits of the SC-PML interpretation. A uniaxial PML formulation has also been presented [2.24] which was successful in matching lossy and dispersive material media.

The advent of the PML has enabled the study of more complex geometries and media, especially within the FDTD and FEM methods. It can be argued that the continued advancement of the PML within these numerical method has contributed significantly to their overall usability since a higher accuracy can be achieved without compromising on the computational costs. The development of the PML outside of these schemes however pales in comparison, even within similarly popular finite difference based numerical algorithms. For example, within the finite difference beam propagation method (BPM) which finds much application in simulation of optoelectronics devices, the PML was first and only demonstrated in [2.25]. A modified dufort-Frankel BPM technique was proposed in [2.26] which for the first time reported the instability issues which arise in the usage of the PML in BPM. Similarly, as mentioned in Chapter 1, only a handful of TLM-PML [2.27]-[2.33] formulations have been proposed. The first demonstration of the PML in TLM was via a hybrid TLM-FDTD grid approach [2.27]. This was based on the non-Maxwellian PML formulation and was applied to the termination of the canonical rectangular waveguide test case. In this test case a reflection level below -55 dB was obtained across the full operating bandwidth. Uniform grid TLM-PML formulations have since been proposed for 2D and 3D TLM simulations [2.29]-[2.33]. These were also based on the split-field formulation, all of which have demonstrated a significant absorption of outgoing waves is attainable with the PML. However, instabilities inherent with the

TLM-PML schemes have also been reported in [2.28]-[2.33] which generally limits the application of PMLs in TLM.

2.3 Limitations Of The PML

In the continuous setting the PML equations boast of the property of being reflectionless and are generally recognized as a superior alternative to the local ABCs. However, upon discretization the limitations of the PML become evident. Firstly, the continuous and infinite medium is approximated by discrete finite layers. Truncating the PML to a finite thickness introduces a residual-wave which is propagated back into the computational domain. In theory, the attenuating ability of the PML increases proportionally with the PML conductivity and so the amplitude of the residual wave can be reduced to a near zero value. However, the discretisation of the PML equations modifies the phase velocities of the propagating waves and introduces numerical dispersion into the model [2.1],[2.3]. Consequently, this alters the “perfect” matching property and generates transitional reflections at the PML-to-media interface and between adjacent PML layers.

The transitional reflections generated by the discrete PML are particularly exacerbated by discontinuities in material properties across the PML-to-media interface. For this reason, a mitigating strategy to reduce the PML reflections involves introducing a smooth conductivity profile across the PML layers, such that the PML conductivity is gradually increased from a near zero value to a maximum value at the end of the PML. In practice, the parabolic and geometric conductivity smoothing functions are commonly employed due to the minimal reflections obtainable [2.3]. Indeed, another way to circumvent the discretization based reflections involves increasing the grid resolution. This is intuitive since the discrete PML equations become the exact PML equations in the limit when the grid resolution tends to zero. However, this is impractical since the computational costs of simulating with a fine grid often outweigh the benefit (i.e. higher accuracy).

An important observation to be made is the discrepancy in the PML performance across various numerical models. This behaviour is widely reported and

highlights the sensitivity of the continuous PML models to the underlying discretization technique employed. A clear demonstration of this is the appearance of instabilities in some numerical implementations whilst absent in others. According to the study carried out in [2.34],[2.35] for a given discretization the long time performance of the continuous PML model can either be strengthened or weakened. Careful consideration must therefore be given at the discretization stage to ensure appropriate temporal behaviour is maintained. A second example demonstrating the discrete PMLs susceptibility to the numerical approach employed is the superior absorption (approximately 40 dB higher) obtainable with the FDTD scheme compared to similar second-order accurate methods e.g. TLM [2.31]. In sharp contrast to the continuous PML, fewer attempts have been made to obtain closed-form expressions of the numerical reflection generated by the discretized PML. Optimisation of the PML with the aim of minimising the reflections generated is thus generally carried out for each application by tuning the PML parameters, i.e. the thickness of the PML layer, the conductivity across each PML layer and the conductivity profile.. The main difficulty in quantifying the discrete PMLs performance lies in the fact that a cascade of numerical reflections are generated as each wave passes through the PML layers. Keeping track of all reflections becomes increasingly challenging as the number of layers grows. In addition, such an analysis can only be performed for one frequency at a time, which further complicates the optimization effort.

A seldomly addressed but important limitation of the continuous PML is that their performance is severely degraded when waves are incident on them at near-grazing angles. Grazing angles of incidence are observed when a scatterer or a source is located close to the PML. They are also present in the simulation of elongated structures such as in waveguides. From the PML field solution derived in (2.17), it was shown that the attenuation rate depends on the $\cos \xi_i$ term. Wide angle incident waves are thus attenuated less than normally incident (i.e. $\xi_i = 0$) waves. Applications where the waves are propagating at a grazing angle will thus require a substantial increase in PML thickness to ensure these transitional reflections are substantially reduced.

In their present form the classical PML models (as described in Section 2.1) strongly absorb evanescent waves much more than purely travelling waves [2.1]. This however creates complications in finite methods since their absorption is much stronger than can be properly sampled in space i.e. shorter than a spatial step. As a result evanescent waves are thus strongly or entirely reflected by discrete PMLs [2.37],[2.38]. To mitigate this, an extension of the SC-PML was proposed which is referred to as the complex frequency shifted (CFS) PML [2.1],[2.39]-[2.40]. The CFS-PML adds a degree of freedom α_i to the complex stretch factor s_i . The stretch factor as defined in (2.7) is modified to,

$$s_i = 1 + \frac{\sigma_i}{\alpha_i + j\omega\epsilon_0}, \quad \text{for } i = x, y, z \quad (2.25)$$

By a careful choice of α_i the zero-frequency singularity (i.e. frequency dependent pole) can be shifted off the real axis onto the negative imaginary axis of the complex plane. In this way the CFS-PML acts as a low pass filter and thus enables a reasonable attenuation of both the travelling and low frequency evanescent waves. In addition to an improved absorption of low evanescent waves, the CFS-PML has also been demonstrated to improve the absorption of near-grazing incident fields.

2.4 Summary

To conclude, a general discussion of the behavior of the classical PML equations in the continuous and discrete domains was delivered in this chapter. The theory of the PML was presented through the split-field, uniaxial and stretched-coordinate PML interpretations. The main distinctions between each interpretation was highlighted. That is, the UPML offers a Maxwellian representation of the PML which has a physical basis of a diagonally anisotropic medium. Compared to the split-field, which relies on an orthogonal field splitting, both UPML and SC-PML have an advantage of being utilized in unstructured grids. Overall the SC-PML offers a more mathematically rigorous interpretation of the PML and has thus contributed significantly to re-formulations/advances of the PML as well as its extension beyond the electromagnetic domain.

Whilst in theory the PML offers an extraordinary solution to the challenge of domain truncation, its limitations are evident in practical use. The discretization process alters the “perfect” matching condition and generates spurious reflections which propagate into the interior domain. The performance discrepancy between different PML implementations also indicate a sensitivity to the underlying discretization approach taken. This phenomena is demonstrated by the difference in reflection performance observed across various numerical schemes as well as the degradation in temporal behavior observed in some methods.

Nonetheless, even with its limitations the PML is still widely recognized as the preferred domain termination technique. The continued advancement of the PML can significantly impact the overall usability of a numerical method providing that an effective implementation is attainable. This is particularly true for the TLM method.

References

- [2.1] J-P. Bérenger, *Perfectly Matched Layer (PML) for Computational Electromagnetics*, Morgan & Claypool publishers, 2007.
- [2.2] S. Ramo, J. R. Whinnery, and T. Van Duzer, *Fields and Waves in Communication Electronics*, 3rd ed. John Wiley & Sons, Inc., 1997.
- [2.3] J.P. Bérenger, “A perfectly matched layer for the absorption of electromagnetic waves”, *J. Comput. Phys.*, 114, (1), pp. 185–200, 1994.
- [2.4] S. D. Gedney, “An anisotropic perfectly matched layer absorbing medium for the truncation of FDTD lattices,” *IEEE Trans. Antennas Propagat.*, vol. 44, pp. 1630–1639, Dec. 1996.
- [2.5] Z. S. Sacks, D. M. Kingsland, R. Lee, and J. F. Lee, "A perfectly matched anisotropic absorber for use as an absorbing boundary condition," *IEEE Trans. Antennas Propagat.*, vol. 43, pp. 1460-1462, Dec. 1995.
- [2.6] W.C Chew, and W.H Weedon,. “A 3D perfectly matched medium from modified Maxwell’s equations with stretched coordinates”, *Microwave and Optical Tech. Lett.*,7, (13), pp. 599–604, 1994.

- [2.7] F. L. Teixeira and W. C. Chew, "Systematic derivation of anisotropic PML absorbing media in cylindrical and spherical coordinates," in *IEEE Microwave and Guided Wave Letters*, vol. 7, no. 11, pp. 371-373, Nov. 1997, doi: 10.1109/75.641424.
- [2.8] W. C. Chew and Q. H. Liu, "Perfectly matched layers for elastodynamics: A new absorbing boundary condition," *J. Comput. Acoust.*, vol. 4, no. 4, pp. 72–79, 1996.
- [2.9] W. C. Chew and Q. H. Liu, "Using perfectly matched layers for elastodynamics," *IEEE Antennas and Propagation Society International Symposium. 1996 Digest*, 1996, pp. 366-369 vol.1, doi: 10.1109/APS.1996.549614.
- [2.10] Q. H. Liu and J. Tao, "Perfectly matched layers for acoustic waves in viscous media: Applications to underwater acoustics," *J. Acoust. Soc. Amer.*, vol. 101, no. 5, pt. 2, p. 3182, May 1997.
- [2.11] H. Qi., 1996a: On absorbing boundary conditions for linearized Euler equations by a perfectly matched layer. *J. Comput. Phys.*, 129 , 201–219.
- [2.12] H. Qi., On the construction of PML absorbing boundary condition for the nonlinear Euler equations, *AIAA paper 2006-0798(2006)*.
- [2.13] C. Zheng. A perfectly matched layer approach to the nonlinear Schrödinger wave equations. *J. Comput. Phys.* 227 (2007), 537–556
- [2.14] E. Turkel and A. Yefet, Absorbing PML boundary layers for wave-like equations. *Appl. Numer. Math.* 27 (1998), 533–557
- [2.15] F. Arash; P. Babak; K. Loukas, "Time-domain hybrid formulations for wave simulations in three-dimensional PML-truncated heterogeneous media". *International Journal for Numerical Methods in Engineering.* 101 (3): 165–198, 2015.
- [2.16] F. L. Teixeira and W. C. Chew, "PML-FDTD in cylindrical and spherical grids," in *IEEE Microwave and Guided Wave Letters*, vol. 7, no. 9, pp. 285-287, Sept. 1997,
- [2.17] F. Teixeira, and W. Chew, "Analytical derivation of a conformal perfectly matched absorber for electromagnetic waves," *Microwave and Optical technology letters*, vol. 17, no. 4, pp. 231-236, 1998
- [2.18] M. Kuzuoglu, B. B. Dunder and R. Mittra, "Conformal perfectly matched absorbers in finite element mesh truncation," *IEEE Antennas and Propagation*

- Society International Symposium. Transmitting Waves of Progress to the Next Millennium. 2000 Digest. Held in conjunction with: USNC/URSI National Radio Science Meeting (C, 2000, pp. 1176-1179 vol.2,
- [2.19] S. Wang, X. Wei, Y. Zhou, Q. Ren, Y. Jia and Q. H. Liu, "High-Order Conformal Perfectly Matched Layer for the DGTD Method," in *IEEE Transactions on Antennas and Propagation*, doi: 10.1109/TAP.2021.3084625.
- [2.20] F. Hu and C. Wang, "DG-FETD modeling of EM structures with waveguide excitations," *Proceedings of the 2012 IEEE International Symposium on Antennas and Propagation, 2012*, pp. 1-2, doi: 10.1109/APS.2012.6349010.
- [2.21] I. Villo-Perez, S. Gonzalez Garcia, R. Gomez Martin, and B. Garcia Almedo, "Extension of Berenger's absorbing boundary condition to match dielectric anisotropic media," *IEEE Microwave Guided Wave Lett.*, vol. 7, pp. 302–3
- [2.22] T. Uno, Y. He, and S. Adachi, "Perfectly matched layer absorbing boundary condition for dispersive medium," *IEEE Microwave Guided Wave Lett.*, vol. 7, pp. 264–2.
- [2.23] F. L. Teixeira and W. C. Chew, "A general approach to extend Berenger's absorbing boundary condition to anisotropic and dispersive media," in *IEEE Transactions on Antennas and Propagation*, vol. 46, no. 9, pp. 1386-1387, Sept. 1998,
- [2.24] S. D. Gedney, "An anisotropic PML absorbing media for the FDTD simulation of fields in lossy and dispersive media," *Electromagn.*, vol. 16, pp. 399–415, July/Aug. 1996.
- [2.25] W. P. Huang, C. L. Xu, W. Lui, and K. Yokoyama, "The perfectly matched layer (PML) boundary condition for the beam propagation method," *IEEE Photon. Technol. Lett.*, vol. 8, pp. 649–651, 1996.
- [2.26] P. Sewell, T. M. Benson and A. Vukovic, "A stable DuFort-Frankel beam-propagation method for lossy structures and those with perfectly matched layers," in *Journal of Lightwave Technology*, vol. 23, no. 1, pp. 374-381, Jan. 2005.
- [2.27] C. Eswarappa, and W.J.R Hoefler, "Implementation of Bérenger absorbing boundary conditions in TLM by interfacing FDTD perfectly matched layers", *Electron. Lett.*, 31, (15), pp. 1264-1266, 1995.
- [2.28] N. Pena, and M.M. Ney "A new TLM node for Berenger's perfectly matched layer", *IEEE Microwave and Guided Wave Lett.*, 6, (11), pp. 410-412, 1996.

- [2.29] H.G. Dantanarayana, "Application of TLM for optical microresonators". PhD thesis, University of Nottingham, 2012
- [2.30] N. Pena and M. M. Ney, "Absorbing-boundary conditions using perfectly matched layer (PML) technique for three-dimensional TLM simulations," *IEEE Trans. Microwave Theory Tech.*, vol. 45, pp. 1749–1755, Oct. 1997.
- [2.31] J. L. Dubard, and D. Pompei "Optimization of the PML efficiency in 3-D TLM method." *IEEE Transactions on Microwave Theory and Techniques*; 48(7):1081–1087, 2000.
- [2.32] L. Maguer, and M. M. Ney, "Extended PML-TLM node: an efficient approach for full waveanalysis of open structures." *Int. J. Numer. Model.*, vol. 14 , pp. 129–144, 2001.
- [2.33] T. W. Kang, C. Christopoulos, and J. Paul, "Implementation of the stretched coordinate-based PML for waveguide structures in TLM". *International journal of numerical modelling electronic networks. Devices and fields*. Vol. 18, pp. 107-118, 2005.
- [2.34] S. Abarbanel, D. Gottlieb, and J. S. Hesthaven. "Long time behavior of the perfectly matched layer equations in computational electromagnetics", *J. Sci. Comput.* 17, no. 1–4, 405–422, 2002.
- [2.35] Bécache, E., P. G. Petropoulos, and S. D. Gedney (2004). On the long-time behaviour of unsplit perfectly matched layers, *IEEE Trans. Antennas Propag.* 52, no. 5, 1335–1342.
- [2.36] J. Wu, J. Nehrbass, and R. Lee, "A comparison of PML for TVFEM and FDTD," *Int. J. Num. Model.*, vol. 13, no. 2-3, pp. 233-244, 2000.
- [2.37] J. De Moerloose and M. A. Stuchly, "Behavior of Berenger's ABC for evanescent waves," in *IEEE Microwave and Guided Wave Letters*, vol. 5, no. 10, pp. 344-346, Oct. 1995.
- [2.38] J. P. Berenger, "Numerical reflection of evanescent waves by PMLs: Origin and interpretation in the FDTD case expected consequences to other finite methods", *Int. J. Numer. Modell.-Elect. Netw. Dev. Fields*, vol. 13, pp. 103-114, 2000.

- [2.39] M. Kuzuoglu and R. Mittra, "Frequency dependence of the constitutive parameters of causal perfectly matched anisotropic absorbers," in *IEEE Microwave and Guided Wave Letters*, vol. 6, no. 12, pp. 447-449, Dec. 1996.
- [2.40] J. - . Berenger, "Application of the CFS PML to the absorption of evanescent waves in waveguides," in *IEEE Microwave and Wireless Components Letters*, vol. 12, no. 6, pp. 218-220, June 2002.

Chapter 3

Stretched-Coordinate PML in 2D TLM

This chapter introduces the TLM theory for the two-dimensional (2D) shunt and series nodes where the analogy with the second-order wave equation is derived. Subsequently, a new framework for implementing the stretched coordinate PML equations in TLM will be formulated for the 2D TLM shunt node. The effectiveness of the proposed stretched coordinate TLM-PML scheme will be investigated on an example of wave propagation in the infinite rectangular waveguide where the impact of the PML parameters on the waveguide termination are investigated.

3.1. Introduction

Since the seminal paper by Johns and Beurle. [3.1], the TLM method has continually established itself as a powerful and effective method for numerically solving Maxwell's equations. Originally developed as a two-dimensional (2D) method based on transmission lines interconnected as shunt nodes, the TLM method solves Maxwell's differential equations by mapping to an equivalent set of transmission line equations. It is especially preferred because of the unconditional stability demonstrated [3.2] which has encouraged its application in a variety of complex electromagnetic problems.

As discussed in Chapter 1, open boundary problems in TLM require special boundary treatments to be applied at the edges of the computational domain in order to accurately simulate the conditions of an infinite propagating medium. The finite computational domain could therefore be terminated with either a simple matched

boundary [3.3], an analytical absorbing boundary condition (ABC) [3.4]-[3.5] or the Perfectly Matched Layer (PML) [3.6]-[3.9]. Due to the low absorption capability of the matched boundary and analytical ABC a significant distance (typically greater than twice the largest wavelength of interest) must exist between the boundary and the features of the problem in order to ensure that an accurate solution is obtained [3.10]. This substantially increases the overall computational burden. On the other hand, minimal reflections can be achieved with the PML over a wider frequency range and for wider angles of incidence [3.6]. To date, only a handful of PML formulations have been demonstrated in the TLM method. Included in these are three implementations [3.13]-[3.15] proposed for 2D TLM simulations. The first PML implementation was developed based on a coupling between the 2D TLM and a FDTD network [3.13]. A limitation with this formulation, however, is the non-unified approach taken which introduces parasitic reflections at the TLM-FDTD interface. A unified development was subsequently proposed and implemented for a 2D TLM hybrid node [3.14] which demonstrated better absorption properties than [3.13]. Both PML formulations in [3.13] and [3.14] have been developed based on Bérenger's original split-field interpretation [3.6] which, as discussed in Chapter 2, is not suitable for terminating lossy media. The implementation of an anisotropic 2D TLM-PML was demonstrated in [3.15], which was reported to be unstable.

Prior to the work carried out in this thesis, there had been no reports of a stretched coordinate (SC) PML implementation applicable to terminate 2D TLM grids. Owing to its suitability to general media, the SC PML [3.7] presents a more attractive implementation than the split-field PML [3.6]. However, the inherent complex frequency dependence requires an appropriate yet efficient time domain transformation which in the TLM method is a nontrivial task.

In light of the huge benefits attainable (i.e. in terms of the higher accuracy and lower computational demand gained) the goal of this chapter is to outline a framework for implementing an efficient stretched coordinate PML in TLM. A vital aspect of the development presented is the implementation approach taken to ensure that the unconditional stability of TLM is preserved. Such a formulation will first be developed and validated for the 2D TLM shunt node. Based on the duality of electromagnetics

the theory developed can also be straightforwardly extended to the 2D TLM series node.

The remainder of the chapter is structured as follows: Section 3.2 provides a brief introduction to the 2D TLM theory. The TLM shunt and series node which respectively model transverse electric (TE) and transverse magnetic (TM) propagation will be presented along with their scatter and connect equations. Section 3.3 presents a detailed derivation of the new stretched coordinate TLM-PML formulation which is implemented via a mapping approach for the shunt node. In subsection 3.3.4 the developed method is characterized using the canonical rectangular metal waveguide application. The influence of the PML control parameters will be investigated and the reflection performance compared with published 2D TLM-PML schemes. Section 3.4 summarizes the findings of this chapter.

3.2. TLM Theory

The objective of all numerical methods in Electromagnetics is to obtain approximate solutions to Maxwell's equations (or of equations derived from them) which satisfy specific boundary and initial conditions. A common approach taken by most methods involves a discretization over the function domain, which creates both space and time intervals upon which the field values can be computed. The TLM method models the physical propagation of fields using a wave scattering approach which is implemented by discretizing the spatial domain using a suitably selected network of interconnecting transmission lines [3.3]. Since the propagating medium is modelled as a transmission line network, the propagating waves are thus realized as voltage pulses travelling across transmission line junctions. The basis for such a physical discretization is a derived equivalence between the field variables in space and voltage impulses propagating on transmission lines. Field solutions are obtained by mapping Maxwell's equations to a network of equivalent transmission line equations for which exact solutions can be obtained by applying circuit theory.

A 2D Cartesian TL network is shown in Fig. 3.1 illustrating the processes underpinning the evolution of a voltage pulse in a TLM simulation. The solid lines

represent transmission lines which intersect at nodes. The separation between each node is defined using an elementary unit Δl which represents the mesh discretization length. The time taken for each pulse to travel from one node to the next is given according to the time step $\Delta t = \Delta l/u$ where u is the speed of propagation of the transmission line.

The first step in the TLM simulation involves an **initialisation** of the transmission line network. Through this process the initial and boundary conditions are set and the input sources are defined. The initialization can take different forms and in Fig. 3.1a a Dirac excitation of a point source is assumed. Upon the injection of energy into the grid, voltage pulses travel along the direction of adjacent transmission line arms to the nearest node centre where, due to the mismatch of impedance seen by each pulse at the line intersections, each pulse will experience a **scatter** as shown in Fig. 3.1b. This is an instantaneous process, where pulses incident on the lines are scattered/reflected along the transmission lines to adjacent nodes. Following a TLM scatter, the scattered pulses become the incident pulses to the neighboring transmission lines in the next time step. Given that the TLM scatter is instantaneous in time across the mesh, and assuming all pulses in the network experience the same line impedance, then it is sufficient to assume all scattered pulses arrive as incident pulses at the adjacent nodes at the next time step as shown in Fig.3.1c. The TLM **connect** process is therefore defined by the exchange of pulses from adjacent transmission lines. The condition which enforces the arrival of pulses at the same time is referred to as the time synchronism criterion [3.3]. This iterative process of scattering and connecting defines the manner in which voltage pulses are propagated across the TLM network. The scatter-connect iteration is therefore repeated as many times as is needed to simulate the propagation of voltage pulses across the network. The propagation of voltage impulses described above applies to 2D TLM network, however the principles applied are general and applicable to all dimensions of space as well as for all wave propagation phenomena.

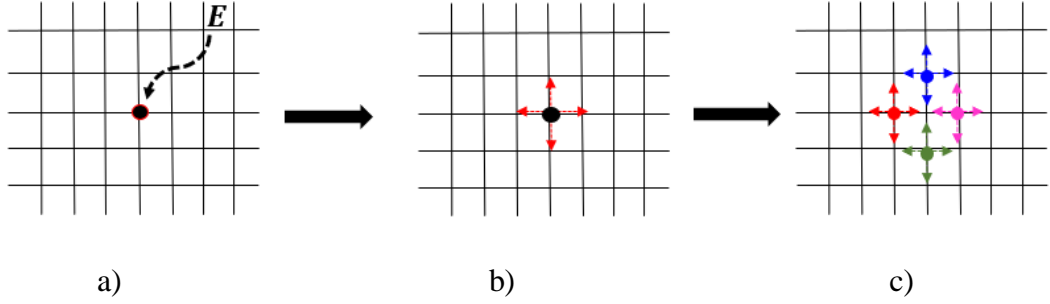


Figure. 3.1 A 2D TL network showing the (a) initialisation, (b) scattering and (c) connect process

An important aspect of the TLM method is the analogy between Maxwell's equations and equations for voltages and currents on a mesh of transmission lines. This concept shall be explored in the following subsections where the isomorphism between the 2D TLM nodes and Maxwell's equations is derived. The 2D TLM shunt and series node configurations which model TM and TE wave propagations will be discussed with their corresponding scatter algorithms presented.

3.2.1 TLM Shunt Node

Consider the differential form of Maxwell's equations as presented in (2.1) and expanded in (2.2a) and (2.2b) for Faraday's and Ampere's law. In the 2D setting, assuming that there are no spatial variations in the z -direction (i. e. $\frac{\partial}{\partial z} = 0$), only the propagation of the Transverse Electric (TE) or the Transverse Magnetic (TM) modes is supported.

For TM-modes, $H_z=0$ and the only non-zero field components are E_z , H_x and H_y . To maintain the simplicity in this discussion the material tensors are assumed to be isotropic i.e. $\mu_x = \mu_y = \mu_z = \mu$, $\epsilon_x = \epsilon_y = \epsilon_z$ and magnetic sources are assumed to be absent $\sigma_m = 0$. Therefore equations (2.2a) and (2.2b) are reduced to:

$$\frac{\partial E_z}{\partial y} = -\mu \frac{\partial H_x}{\partial t}, \quad (3.1a)$$

$$\frac{\partial E_z}{\partial x} = \mu \frac{\partial H_y}{\partial t}, \quad (3.1b)$$

$$\frac{\partial H_y}{\partial x} - \frac{\partial H_x}{\partial y} = \epsilon_z \frac{\partial E_z}{\partial t} + \sigma_{ez} E_z. \quad (3.1c)$$

Differentiating equations (3.1a) and (3.1b) with respect to y and x , respectively, and adding them together obtains

$$\frac{1}{\mu} \frac{\partial^2 E_z}{\partial x^2} + \frac{1}{\mu} \frac{\partial^2 E_z}{\partial y^2} = \frac{\partial}{\partial t} \left(\frac{\partial H_y}{\partial x} - \frac{\partial H_x}{\partial y} \right) \quad (3.2)$$

Substituting the right side of (3.1c) into (3.2) obtains,

$$\frac{1}{\mu} \frac{\partial^2 E_z}{\partial x^2} + \frac{1}{\mu} \frac{\partial^2 E_z}{\partial y^2} = \epsilon_z \frac{\partial^2 E_z}{\partial t^2} + \sigma_{ez} \frac{\partial E_z}{\partial t}, \quad (3.3)$$

which represents the 2D wave equation for the propagation of the E_z electric field component in a 2D xy plane.

The circuit equations isomorphic to (3.2) and (3.3) are given as [3.1]

$$-\frac{1}{\Delta l} \frac{\partial I_x}{\partial x} - \frac{1}{\Delta l} \frac{\partial I_y}{\partial y} = 2C_t^z \frac{\partial V_z}{\partial t} + G_{ez} \frac{\partial V_z}{\partial t}, \quad (3.4)$$

$$\frac{(\Delta l)^2}{L_t^x} \frac{\partial^2 V_z}{\partial x^2} + \frac{(\Delta l)^2}{L_t^y} \frac{\partial^2 V_z}{\partial y^2} = 2C_t^z \frac{\partial^2 V_z}{\partial t^2} + G_{ez} \frac{\partial V_z}{\partial t}, \quad (3.5)$$

respectively, where Δl denotes a discretization length, L_t^x and L_t^y represents the total x and y -directed node inductance, respectively, and C_t^z and V_z denote the total z -directed node capacitance and voltage, respectively, and G_{ez} represents the conductance in the node.

Equations (3.4) and (3.5) represent the law which govern the x and y -propagations of voltage V_z and currents I_x and I_y across an equivalent 2D transmission line structure referred to as a shunt node [3.3]. The transmission line representation of the shunt node is illustrated in Fig. 3.2 which shows two transmission lines with line

admittances given as $Y_i \{ i \in x, y \}$. As shown both lines are intersected at the node centre. An open circuit stub admittance Y_{oz} is connected at the node centre to handle the additional admittance required by the node. As shown, each i -directed transmission line supports the propagation of incident V^i and reflected V^r pulses to and from each TLM node centre. The circuit representation to the shunt node model is presented in Fig. 3.3 which shows the node inductance associated with each transmission line. The node capacitance is also shown to be common to both the x - y transmission lines.

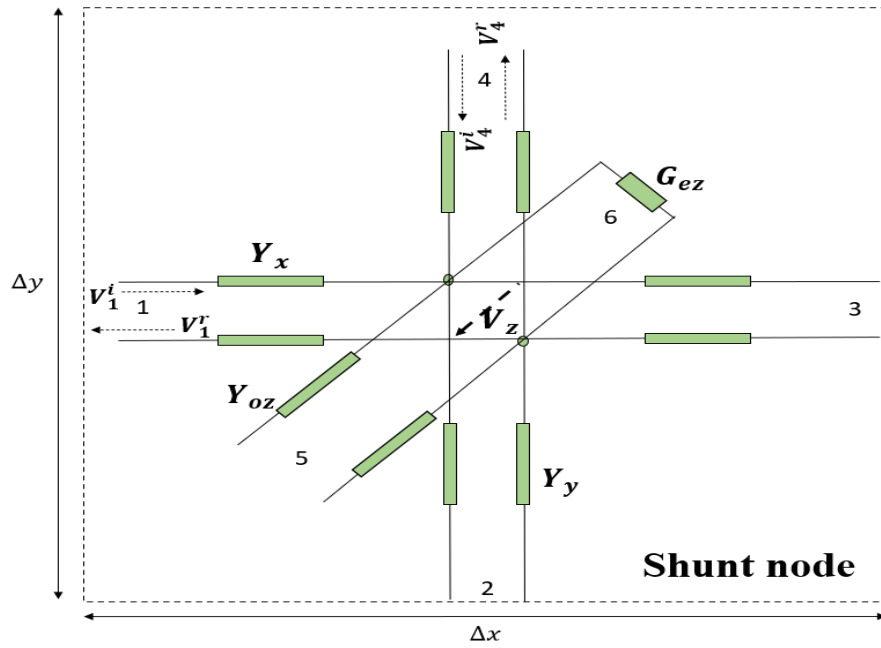


Figure 3.2 Transmission line structure of the shunt node with the capacitive stub at port 5 and lossy stub at port 6.

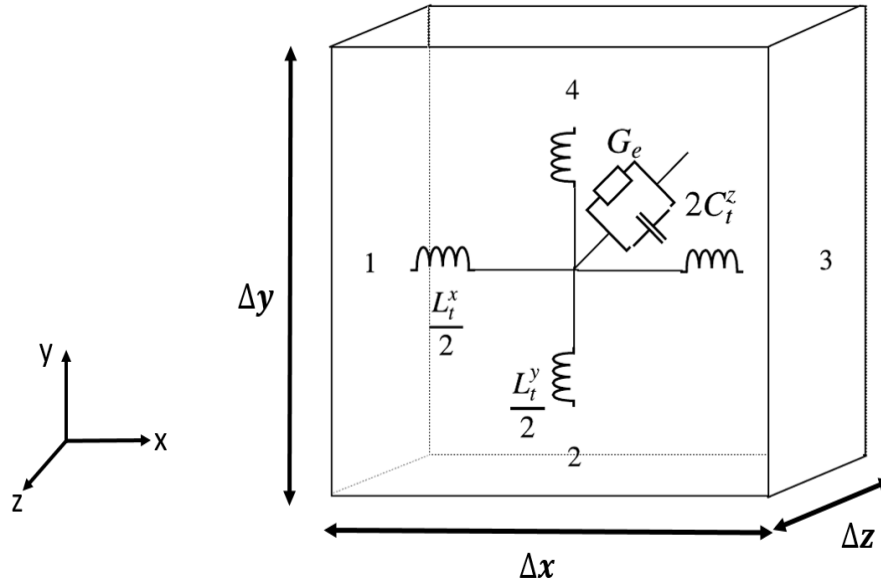


Figure 3.3 The TLM shunt node modelling a block of space with dimensions $\Delta x = \Delta y = \Delta z = \Delta l$.

By comparing the forms of (3.1c) with (3.4) and (3.3) with (3.5) the following equivalence can be established between the field and circuit parameters of the node:

$$\begin{aligned}
 -V_z &= E_z \Delta l, \\
 I_y &= H_x \Delta l, & I_x &= H_y \Delta l, \\
 L_t^x &= \mu \Delta l, & L_t^y &= \mu \Delta l, \\
 C_t^z &= \epsilon_z \Delta l, & G_{ez} &= \sigma_{ez} \Delta l.
 \end{aligned} \tag{3.6}$$

The total inductances L_t^x and L_t^y and capacitance C_t^z in the shunt node are comprised of the sum of the contributions from the distributed inductance and capacitance along each transmission line, as well as contributions from stubs. Traditionally, the TLM stubs are added to each node to make up the node deficits which would otherwise be incorporated in the transmission lines. Therefore, it follows that [3.17]

$$L_t^x = L_y \Delta l,$$

$$L_t^y = L_x \Delta l,$$

$$C_t^z = C_x \Delta l + C_y \Delta l + C_{oz}, \quad (3.7)$$

where C_i and L_i denote the distributed line capacitance and inductance along the i -directed lines, and C_{oz} denotes a capacitive stub. Equations (3.7) represent the general constitutive relations for the shunt node which by substituting parameters from (3.6) yields a relation that allows the appropriate modelling of the medium.

According to transmission line relations, the line admittances Y_i and transit time Δt_i can be defined as follows

$$\Delta t_i = \Delta l \sqrt{L_i C_i}, \quad (3.8)$$

$$Y_i = \sqrt{\frac{C_i}{L_i}}. \quad (3.9)$$

Note that the TLM time synchronism criterion enforces the time step Δt_i to be the same throughout the mesh, therefore $\Delta t_i = \Delta t$. In the stubs, pulses have to make a round trip [3.3], thus requiring the transit time along the length of a stub to be equal to $\Delta t/2$. This results in the following expression for the stub admittance

$$Y_{oz} = \frac{2C_{oz}}{\Delta t}. \quad (3.10)$$

Employing the expressions $C_i \Delta l = Y_i \Delta t$ the general constitutive relation in (3.7) can be re-expressed in terms of line admittances as

$$\epsilon_z \frac{\Delta l}{\Delta t} = Y_x + Y_y + \frac{Y_{oz}}{2}. \quad (3.11)$$

Generally, the transmission line admittances are set to the impedance of the background medium for which in free space $Y_x = Y_y = \frac{Y_o}{\sqrt{2}} = \sqrt{\frac{\epsilon_o}{2\mu_o}}$ [3.3], therefore the

stub admittance handles all deficits on the R.H.S of (3.11). Rearranging (3.11) therefore obtains an expression for the stub admittance in terms of the time step and material permittivity

$$Y_{oz} = 2Y_o(\epsilon_{rz} \frac{\Delta l}{c\Delta t} - \sqrt{2}), \quad (3.12)$$

where ϵ_{rz} represents the relative permittivity of the material, and c denotes the speed of light. In order to ensure stability the stub values must be positive. Hence the time step for the shunt node is determined as $\Delta t \leq \epsilon_{rz} \frac{\Delta l}{c\sqrt{2}}$ since this is the condition which ensures this in (3.12).

3.2.2 TLM Series Node

Following a similar procedure to that described in Section 3.2.1, it can be shown [3.3] that an alternative structure referred to as the series node models the propagation of the TE-modes. Intuitively the circuit's z -directed current I_z is mapped to the z -polarized magnetic field H_z and since $E_z = 0$ then the x and y -directed electric fields, E_x and E_y are mapped to the propagation of the V_x and V_y voltage components, respectively. The transmission line schematic of the series node is shown Fig. 3.4 where ports 5 and 6 are the connections to the inductive and lossy stubs, respectively.

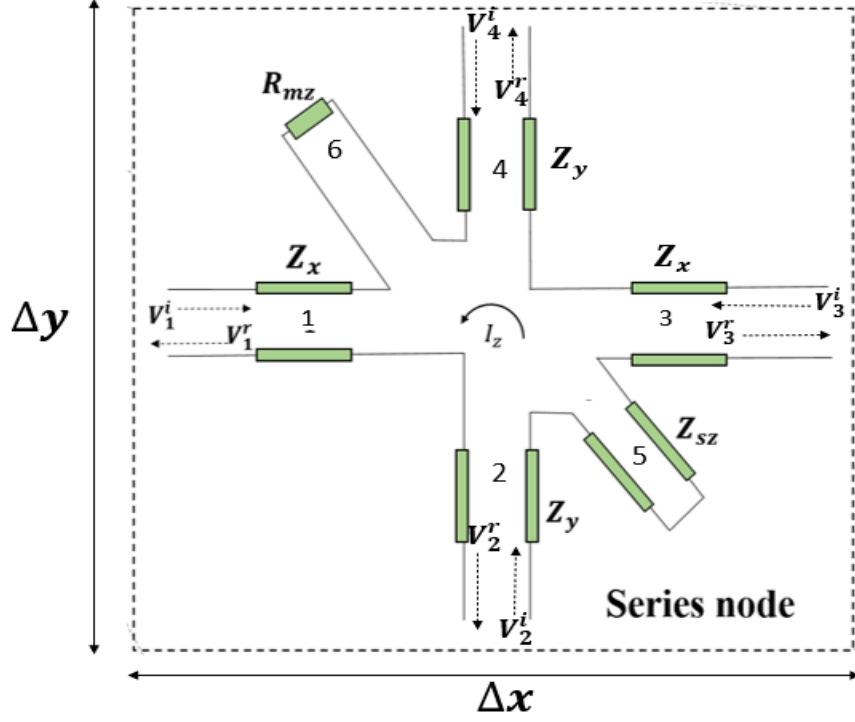


Figure 3.4 Transmission line structure of the series node showing the inductive stub at port 5 and lossy stub at port 6.

The field to circuit equivalence for TE mode propagation is given as [3.3]

$$\begin{aligned}
 I_z &= H_z \Delta l, \\
 -V_y &= E_y \Delta l, & -V_x &= E_x \Delta l, \\
 C_t^x &= \epsilon \Delta l, & C_t^y &= \epsilon \Delta l, \\
 L_t^z &= 2\mu_z \Delta l, & R_{mz} &= \sigma_{mz} \Delta l.
 \end{aligned} \tag{3.13}$$

This yields a general constitutive relation for the series node given in terms of line impedances as [3.17]

$$\mu_z \frac{\Delta l}{\Delta t} = Z_x + Z_y + \frac{Z_{sz}}{2}, \tag{3.14}$$

where Z_{sz} represents the impedance of the inductive stubs. Assuming the transmission lines model a free space background medium then $Z_x = Z_y = Z_0 \sqrt{2}$ [3.3]. Therefore the value of the inductive stub impedance is similarly used to model additional required impedances and is given as

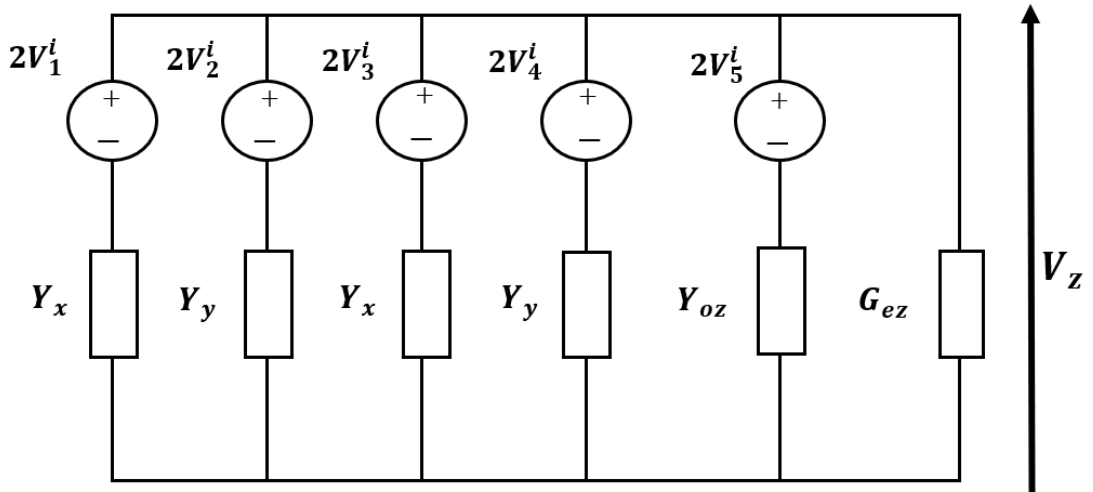
$$Z_{sz} = 2Z_o(\mu_{rz} \frac{\Delta l}{c\Delta t} - \sqrt{2}). \quad (3.15)$$

3.2.3 Scatter and Connect Algorithms

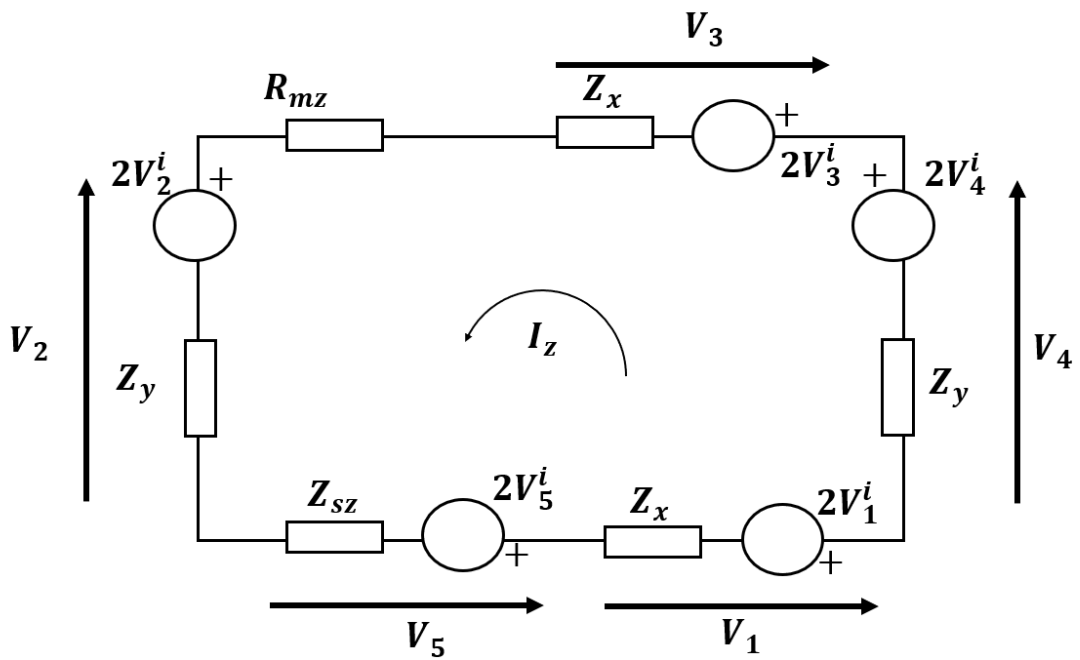
Based on the physical connection of transmission lines the total voltage on each line is given by the sum of the incident and reflected pulses $V = V^i + V^r$ [3.3]. Since the TLM algorithm is a time stepping algorithm at each time step a pulse V^i is incident on each transmission line whose value is determined either by a source excitation or is taken as the pulse V^r scattered from an adjacent transmission line in the previous time step. The scattering process therefore represents a central component of the TLM algorithm as it defines the process for computing the reflected pulses V^r .

By obtaining the total voltage at the node the reflected voltage can be easily calculated. A key advantage of the 2D TLM models is their ability to represent a node by an equivalent electrical circuit. This enables the total node voltage, and thus the scattering matrix, to be straightforwardly obtained upon a circuit analysis of the Thevenin equivalent circuits [3.3].

The Thevenin equivalent circuits for the series and shunt node are respectively shown in Figs. 3.5a and 3.5b.



(a)



(b)

Figure 3.5 Thevenin equivalent models of 2D TLM nodes:

(a) Shunt node circuit (b) Series node circuit.

By a simple circuit analysis of Fig. 3.5a (assuming $Y_x = Y_y = Y_{TL}$) the following expression for the total voltage for the shunt node is

$$V_z = 2 \frac{V_1^i + V_2^i + V_3^i + V_4^i + \hat{Y}_{oz} V_5^i}{4 + \hat{G}_{ez} + \hat{Y}_{oz}}, \quad (3.16)$$

where \hat{Y}_{oz} and \hat{G}_{ez} represent normalized quantities given as,

$$\hat{Y}_{oz} = \frac{Y_{oz}}{Y_{TL}}, \quad \hat{G}_{ez} = \frac{G_{ez}}{Y_{TL}}.$$

Applying the relation $V^r = V - V^i$ on each port results in the scattering equation for the shunt node at the time step N as

$$\begin{bmatrix} {}_N V_1^r \\ {}_N V_2^r \\ {}_N V_3^r \\ {}_N V_4^r \\ {}_N V_5^r \end{bmatrix} = \begin{bmatrix} 2\alpha - 1 & 2\alpha & 2\alpha & 2\alpha & 2\hat{Y}_{oz}\alpha \\ 2\alpha & 2\alpha - 1 & 2\alpha & 2\alpha & 2\hat{Y}_{oz}\alpha \\ 2\alpha & 2\alpha & 2\alpha - 1 & 2\alpha & 2\hat{Y}_{oz}\alpha \\ 2\alpha & 2\alpha & 2\alpha & 2\alpha - 1 & 2\hat{Y}_{oz}\alpha \\ 2\alpha & 2\alpha & 2\alpha & 2\alpha & 2\hat{Y}_{oz}\alpha - 1 \end{bmatrix} \begin{bmatrix} {}_N V_1^i \\ {}_N V_2^i \\ {}_N V_3^i \\ {}_N V_4^i \\ {}_N V_5^i \end{bmatrix}, \quad (3.17)$$

with

$$\alpha = \frac{1}{4 + \hat{G}_{ez} + \hat{Y}_{oz}}.$$

However, in the series node V represents the total voltage at each port n which is given as $V_n = V_n^i - I_z Z_{TL}$. Assuming $Z_x = Z_y = Z_{TL}$, then the loop current I_z is given as

$$I_z = 2 \frac{V_1^i + V_4^i - V_3^i - V_2^i + V_5^i}{4Z_{TL} + R_{mz} + Z_{sz}} \quad (3.18)$$

with

$$\hat{Z}_{sz} = \frac{Z_{sz}}{Z_{TL}}, \quad \hat{R}_{mz} = \frac{R_{mz}}{Z_{TL}},$$

this results in the following expression for the scattering equation

$$\begin{bmatrix} {}_N V_1^r \\ {}_N V_2^r \\ {}_N V_3^r \\ {}_N V_4^r \\ {}_N V_5^r \end{bmatrix} = \begin{bmatrix} 1 - 2\gamma & 2\gamma & 2\gamma & -2\gamma & -2\gamma \\ 2\gamma & 1 - 2\gamma & -2\gamma & 2\gamma & 2\gamma \\ 2\gamma & -2\gamma & 1 - 2\gamma & 2\gamma & 2\gamma \\ -2\gamma & 2\gamma & 2\gamma & 1 - 2\gamma & -2\gamma \\ 2\gamma \hat{Z}_{sz} & 2\gamma \hat{Z}_{sz} & 2\gamma \hat{Z}_{sz} & -2\gamma \hat{Z}_{sz} & 1 - 2\gamma \hat{Z}_{sz} \end{bmatrix} \begin{bmatrix} {}_N V_1^i \\ {}_N V_2^i \\ {}_N V_3^i \\ {}_N V_4^i \\ {}_N V_5^i \end{bmatrix}, \quad (3.19)$$

with

$$\gamma = \frac{1}{4 + \hat{R}_{mz} + \hat{Z}_{sz}},$$

The TLM connect process represents the exchange of the voltages between the adjacent nodes where reflected voltages from adjacent nodes become incident at the neighbor nodes at the next time step $N+1$ as

$$\begin{aligned} {}_{N+1} V_1^i(x + \Delta x, y) &= {}_N V_3^r(x, y), \\ {}_{N+1} V_3^i(x - \Delta x, y) &= {}_N V_1^r(x, y), \\ {}_{N+1} V_2^i(x, y + \Delta y) &= {}_N V_4^r(x, y), \\ {}_{N+1} V_4^i(x, y - \Delta y) &= {}_N V_2^r(x, y), \\ {}_{N+1} V_5^i(x, y) &= {}_N V_5^r(x, y), \end{aligned} \quad (3.20)$$

where the L.H.S represents the incident voltages at each port in a node at the next time step $N+1$, and the R.H.S represents the reflected voltages from adjacent nodes computed at the time step N .

In TLM, losses in the form of electric σ_e and magnetic σ_m conductivities are respectively modelled using lossy stubs G_{ez} and R_{mz} which are terminated by their own characteristic impedances. Their main contribution is the removal of energy from the node, for this reason no pulse is incident from them on the node. This explains the absence of associated voltage sources in port 6 of the Thevenin circuits shown in Figs. 3.5a and b.

3.2.4 Modelling Boundaries in TLM

In the TLM method simple boundaries can be modelled as straightforward modifications of the connect equations (3.20). For the case where a physical boundary is located on the port 3 for example, then the connect equation for the port is modified as follows:

$${}_N V_3^i(x, y) = \Gamma_{N-1} V_3^r(x, y), \quad (3.21)$$

where Γ represents the reflection coefficient calculated as

$$\Gamma = \frac{Z_s - Z_{TL}}{Z_s + Z_{TL}}, \quad (3.22)$$

where Z_s denotes the impedance of the boundary at the port 3 and Z_{TL} is the characteristic impedance of the line. In the specific case of the short circuit or perfect metallic boundary, it is assumed that the boundary impedance is $Z_s = 0$, and reflection coefficient is $\Gamma = -1$. For the specific case of open circuit of a perfect magnetic wall, the boundary impedance is $Z_s \rightarrow \infty$ and the reflection coefficient is given as $\Gamma = 1$.

A more interesting case is the representation of open boundaries using the concept of a matched impedance. By setting the boundary impedance equal to the transmission line impedance $Z_s = Z_{TL}$ a fictitious open boundary can be represented as $\Gamma = 0$. This approach is commonly referred to as the Matched boundary or Matched termination and, although it offers a highly efficient solution to simulating open boundaries, it is however only effective in applications with waves impinging normally on the boundary. In problems with oblique incident waves reflections are generated at the boundary which inevitably propagate back into the solution space.

3.3. Stretched Coordinate PML Formulation in 2D TLM

In the previous section, the core principles of TLM theory were introduced. The remainder of this chapter shall focus on the formulation for developing the stretched coordinate PML in 2D TLM.

According to the theory presented in Chapter 2, the attenuation of propagating fields is achieved in the stretched coordinate PML by imposing an analytic continuation which maps real to complex space $\mathbb{R} \rightarrow \mathbb{C}$. In the Cartesian coordinate system the new complex metric is thus obtained by the following transformation [3.7]

$$\begin{aligned}\partial x &\rightarrow \tilde{\partial}x = S_x \partial x, \\ \partial y &\rightarrow \tilde{\partial}y = S_y \partial y,\end{aligned}\tag{3.23}$$

where ∂x and ∂y are the differential lengths along each coordinate axis, $\tilde{}$ indicates the complex stretched complements. Variable S_i denotes a frequency dependent complex stretch factor given as

$$S_i = 1 + \frac{\sigma_{si}}{j\omega}, \quad \text{with} \quad \sigma_{si} = \frac{\sigma_i}{\epsilon_0},\tag{3.24}$$

where σ_{si} represents a positive real variable and $\sigma_i \geq 0$ is a conductivity parameter used to control the attenuation of the incident fields in a PML.

Consider the case for TM mode propagation which is modelled by the TLM shunt node. By substituting the spatial derivatives given in (3.23) into the 2D wave equation (3.3) the second order stretched coordinate PML equation is obtained as:

$$\frac{1}{\mu_y} \frac{1}{S_x^2} \frac{\partial^2 E_z}{\partial x^2} + \frac{1}{\mu_x} \frac{1}{S_y^2} \frac{\partial^2 E_z}{\partial y^2} = \epsilon_z \frac{\partial^2 E_z}{\partial t^2} + \sigma_{ez} \frac{\partial E_z}{\partial t}.\tag{3.25}$$

The TLM implementation of (3.25) can be achieved in a number of different ways. However, since the TLM algorithm models the physical behavior of wave

propagations a crucial point to maximize the efficacy of the SC PML implementation is to apply the coordinate stretching directly to the numerical algorithm itself. This ensures that the dispersion error attributable to the discretization is impedance matched by the PML. This also guarantees that the highly desired unconditional stability of the TLM node is preserved following the PML implementation. For this reason a TLM implementation of the SC PML is not sought for the form presented in (3.25), but rather equation (3.26) is manipulated into a suitable form to reveal the transformation of the transmission line parameters in terms of the geometric change prescribed by (3.27).

This is achieved by multiplying both sides of (3.25) with $S_x S_y$. This results in a re-expression of the SC PML equation given as

$$\frac{1}{\mu_x} \frac{S_y}{S_x} \frac{\partial^2 E_z}{\partial x^2} + \frac{1}{\mu_y} \frac{S_x}{S_y} \frac{\partial^2 E_z}{\partial y^2} = \epsilon_z S_x S_y \frac{\partial^2 E_z}{\partial t^2} + \sigma_{ez} S_x S_y \frac{\partial E_z}{\partial t}. \quad (3.26)$$

Comparing the forms of (3.26) and (3.3) enables the spatial transformation given in (3.23) to be mapped on to the circuit expressions as given in (3.5). This yields

$$\frac{(\Delta l)^2}{L_t^x} \frac{S_y}{S_x} \frac{\partial^2 V_z}{\partial x^2} + \frac{(\Delta l)^2}{L_t^y} \frac{S_x}{S_y} \frac{\partial^2 V_z}{\partial y^2} = 2S_x S_y C_t^z \frac{\partial^2 V_z}{\partial t^2} + S_x S_y G_{ez} \frac{\partial V_z}{\partial t}. \quad (3.27)$$

Equivalent circuit parameters in the stretched domain are thus given as

$$\begin{aligned} \tilde{L}_t^x &= \frac{S_x}{S_y} L_t^x = \frac{S_x}{S_y} \mu_x \Delta l, \\ \tilde{L}_t^y &= \frac{S_y}{S_x} L_t^y = \frac{S_y}{S_x} \mu_y \Delta l, \\ \tilde{C}_t^z &= S_x S_y C_t^z = S_x S_y \epsilon_z \Delta l, \\ \tilde{G}_{ez} &= S_x S_y G_{ez} = S_x S_y \sigma_{ez} \Delta l. \end{aligned} \quad (3.28)$$

According to (3.28), the complex coordinate stretching in (3.23) maps the standard shunt node defined in real space to a PML shunt node defined in complex

space. Hence the transformed node is referred to as the **mapped shunt node**. In accordance with the TLM general constitutive relation (3.7), which separates the total node parameters into contributions from distributed line components, it is clear that with the mapped shunt node each distributed line component undergoes a similar transformation to its associated node parameters. Therefore, the distributed line inductances \tilde{L}_x and \tilde{L}_y in the mapped shunt node are transformed in a similar manner as the total inductances, thus yielding

$$\begin{aligned}\tilde{L}_x &= \frac{S_x}{S_y} L_x, \\ \tilde{L}_y &= \frac{S_y}{S_x} L_y,\end{aligned}\tag{3.29}$$

where \tilde{L}_x and \tilde{L}_y represent the inductance distributed along the x and y -directed lines in the mapped shunt node and L_x and L_y denote the x and y -directed line inductances in the standard shunt node.

Likewise, the distributed line capacitances are transformed in a similar way to C_t^z to yield

$$\begin{aligned}\tilde{C}_x &= S_x S_y C_x, \\ \tilde{C}_y &= S_x S_y C_y, \\ \tilde{C}_{oz} &= S_x S_y C_{oz},\end{aligned}\tag{3.30}$$

where \tilde{C}_x and \tilde{C}_y denote the capacitance distributed along the x - and y -directed lines, respectively, and \tilde{C}_{oz} denotes the stub capacitance in the mapped shunt node.

Following from (3.29)-(3.30), the propagation delays experienced by pulses propagating along the x - and y -directed lines of the mapped shunt node are given as

$$\tilde{\Delta}t_x = \Delta l \sqrt{\tilde{L}_x \tilde{C}_x} = \Delta l \sqrt{L_x \frac{S_x}{S_y} S_x S_y C_x} = S_x \Delta t,$$

$$\tilde{\Delta}t_y = \Delta l \sqrt{\tilde{L}_y \tilde{C}_y} = \Delta l \sqrt{L_y \frac{S_y}{S_x} S_x S_y C_y} = S_y \Delta t, \quad (3.31)$$

where $\tilde{\Delta}t_x$ and $\tilde{\Delta}t_y$ are the timesteps associated with the x and y directed transmission lines, respectively. Expanding (3.31) reveals the complex form of the propagation delay which is given as follows

$$\begin{aligned} \tilde{\Delta}t_x &= \Delta t S_x = \Delta t \left(1 + \frac{\sigma_{sx}}{j\omega} \right), \\ \tilde{\Delta}t_y &= \Delta t S_y = \Delta t \left(1 + \frac{\sigma_{sy}}{j\omega} \right). \end{aligned} \quad (3.32)$$

The resulting characteristic admittances in the mapped shunt node are given as

$$\begin{aligned} \tilde{Y}_x &= \sqrt{\frac{S_x S_y C_x}{\frac{S_x}{S_y} L_x}} = Y_x S_y, \\ \tilde{Y}_y &= \sqrt{\frac{S_x S_y C_y}{\frac{S_y}{S_x} L_y}} = Y_y S_x, \end{aligned} \quad (3.33)$$

The characteristic admittance of the capacitive stubs Y_{oz} experiences a similar stretching to C_{oz} and is thus given as

$$\tilde{Y}_{oz} = Y_{oz} S_x S_y. \quad (3.34)$$

The equivalent circuit representing the mapped shunt node is illustrated in Fig. 3.6 which takes a similar form to the regular shunt node shown in Fig. 3.5b but employs the use of transformed characteristic admittances and conductance. It should be noted that the circuit and transmission line parameters of the mapped shunt node reduce to the standard shunt node parameters when $\sigma_i = 0$, i. e. $S_x = S_y = 1$.

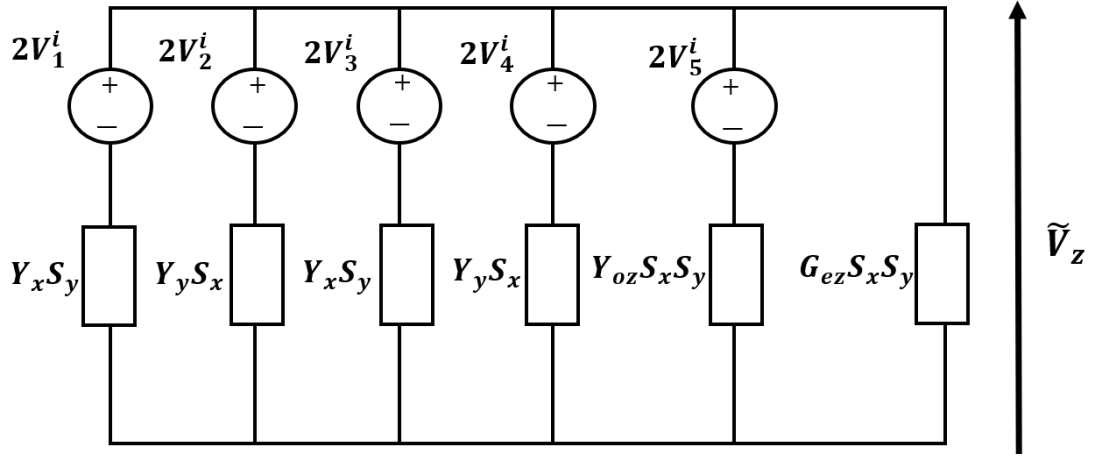


Figure 3.6 Thevenin equivalent circuit of the mapped shunt node.

3.3.1. Modified Scatter and Connect Algorithm

The developments made in the previous sub-section have described how the complex stretching of space in the PML medium transforms the 2D TLM circuit parameters to equivalent complex frequency components in the stretched coordinates. This section outlines the resulting modifications to the TLM scatter algorithms following the complex domain stretching.

In the 2D shunt TLM node, the reflected voltage at each port n is given by

$$V_n^r = \tilde{V}_z - V_n^i, \quad (3.35)$$

where V_n^i is the voltage incident on port n and \tilde{V}_z is the total voltage in the mapped shunt node.

Assume that the link line admittances are equal i.e. $Y_x = Y_y = Y_{TL}$. By a simple circuit analysis of Fig. 3.7 the following expression is obtained

$$\tilde{V}_z = 2 \frac{S_y(V_1^i + V_3^i) + S_x(V_2^i + V_4^i) + S_x S_y \hat{Y}_{oz} V_5^i}{2S_y + 2S_x + S_x S_y (\hat{G}_{ez} + \hat{Y}_{oz})}, \quad (3.36)$$

where the stub admittance Y_{oz} and node conductance G_{ez} respectively are normalised to the line admittance as follows $\hat{Y}_{oz} = \frac{Y_{oz}}{Y_{TL}}$ and $\hat{G}_{ez} = \frac{G_{ez}}{Y_{TL}}$.

In its present form the total voltage \tilde{V}_z as defined in (3.36) is a complex and frequency dependent variable and requires transformation to a time domain representation. In the TLM method the standard approach to incorporate frequency dependent quantities involves the use of digital filters [3.18]. This requires the following transformation

$$j\omega \rightarrow s \rightarrow \frac{2(1-z^{-1})}{\Delta t(1+z^{-1})} \rightarrow [N\Delta t]. \quad (3.37)$$

where s and z are the Laplace and Z-transform variables, respectively.

Upon an s-domain transformation ($j\omega \rightarrow s$) the stretch factors become $S_x = 1 + \frac{\sigma_{sx}}{s}$, $S_y = 1 + \frac{\sigma_{sy}}{s}$ which, when substituted into (3.36), yield the expression

$$\tilde{V}_z[s] = \frac{M(s)}{N(s)}, \quad (3.38)$$

where

$$M(s) = 2s(s + \sigma_{sy})(V_1^i + V_3^i) + 2s(s + \sigma_{sx})(V_2^i + V_4^i) + 2(s + \sigma_{sx})(s + \sigma_{sy})\hat{Y}_{oz}$$

and

$$N(s) = s(4s + 2\sigma_{sy} + 2\sigma_{sx}) + (s + \sigma_{sx})(s + \sigma_{sy})(\hat{Y}_{oz} + \hat{G}_{ez}).$$

By applying the bilinear transformation $s \rightarrow \frac{2(1-z^{-1})}{\Delta t(1+z^{-1})}$ to (3.38) the following Z-transform representation is obtained,

$$\tilde{V}_z[z] = \alpha^{PML} \begin{bmatrix} Y_{st}(V_z - 2V_z z^{-1} + V_z z^{-2}) + \\ \sigma_{sy}\Delta t(V_1^i + V_3^i - V_1^i z^{-2} - V_3^i z^{-2}) + \\ \sigma_{sx}\Delta t(V_2^i + V_4^i - V_2^i z^{-2} - V_4^i z^{-2}) + \\ AV_5^i + BV_5^i z^{-1} + CV_5^i z^{-2} + \\ D\tilde{V}_z z^{-1} - E\tilde{V}_z z^{-2} \end{bmatrix}, \quad (3.39)$$

where V_z represents the voltage in the standard shunt node given as

$$V_z = 2 \frac{V_1^i + V_2^i + V_3^i + V_4^i + \hat{Y}_{oz} V_5^i}{Y_{st}},$$

and the coefficients are given as

$$\begin{aligned} Y_{st} &= 4 + G, \\ G &= \hat{Y}_{oz} + \hat{G}_{ez}, \\ A &= \hat{Y}_{oz} \left(\sigma_{sx} \Delta t + \sigma_{sy} \Delta t + \frac{\sigma_{sx} \sigma_{sy} \Delta t^2}{2} \right), \\ B &= \hat{Y}_{oz} \sigma_{sx} \sigma_{sy} \Delta t^2, \\ C &= \hat{Y}_{oz} \left(-\sigma_{sx} \Delta t - \sigma_{sy} \Delta t + \frac{\sigma_{sx} \sigma_{sy} \Delta t^2}{2} \right), \\ D &= 8 + G \left(2 - \frac{\sigma_{sx} \sigma_{sy} \Delta t^2}{2} \right), \\ E &= 4 + G - \left(1 + \frac{G}{2} \right) (\sigma_{sx} \Delta t + \sigma_{sy} \Delta t) + \frac{G \sigma_{sx} \sigma_{sy} \Delta t^2}{4}, \\ \alpha^{PML} &= \frac{Y_{st}}{4 + G + \left(1 + \frac{G}{2} \right) (\sigma_{sx} \Delta t + \sigma_{sy} \Delta t) + \frac{G \sigma_{sx} \sigma_{sy} \Delta t^2}{4}}, \end{aligned}$$

To obtain a discrete time domain representation of $\tilde{V}_z[z]$ an inverse Z-transform is performed on (3.39) where z^{-p} indicates the use of the sample at the p^{th} previous time step, $(N - p)\Delta t$, denoted as “ ${}_{N-p}$ ”. This yields a compact formulation

$${}_{N}\tilde{V}_z = \alpha^{PML} {}_{N}V_z + {}_{N}V_z^{PML}, \quad (3.40)$$

where the PML voltage ${}_{N}V_z^{PML}$ represents a digital filter attributed to the analytical continuation given as

$${}_{N}V_z^{PML} = \frac{\alpha^{PML}}{Y_{st}} \left[\begin{aligned} &Y_{st} ({}_{N-2}V_z - 2 {}_{N-1}V_z) + \\ &+ \sigma_{sy} \Delta t ({}_{N}V_1^i + {}_{N}V_3^i - {}_{N-2}V_1^i - {}_{N-2}V_3^i) + \\ &\sigma_{sx} \Delta t ({}_{N}V_2^i + {}_{N}V_4^i - {}_{N-2}V_2^i - {}_{N-2}V_4^i) + \\ &A {}_{N}V_5^i + B {}_{N-1}V_5^i + C {}_{N-2}V_5^i + \\ &+ D {}_{N-1}\tilde{V}_z - E {}_{N-2}\tilde{V}_z \end{aligned} \right], \quad (3.41)$$

Substituting (3.40) into (3.35) yields a general expression for the reflected voltage at each port n which is given as

$${}_N V_n^r = \alpha^{PML} {}_N V_Z - {}_N V_n^i + {}_N V_Z^{PML}. \quad (3.42)$$

The TLM scatter process for the mapped shunt node can also be succinctly expressed by the scattering matrix

$$\begin{bmatrix} {}_N V_1^r \\ {}_N V_2^r \\ {}_N V_3^r \\ {}_N V_4^r \\ {}_N V_5^r \end{bmatrix} = \begin{bmatrix} 2\alpha^{PML} - 1 & 2\alpha^{PML} & 2\alpha^{PML} & 2\alpha^{PML} & 2\hat{Y}_{oz}\alpha^{PML} \\ 2\alpha^{PML} & 2\alpha^{PML} - 1 & 2\alpha^{PML} & 2\alpha^{PML} & 2\hat{Y}_{oz}\alpha^{PML} \\ 2\alpha^{PML} & 2\alpha^{PML} & 2\alpha^{PML} - 1 & 2\alpha^{PML} & 2\hat{Y}_{oz}\alpha^{PML} \\ 2\alpha^{PML} & 2\alpha^{PML} & 2\alpha^{PML} & 2\alpha^{PML} - 1 & 2\hat{Y}_{oz}\alpha^{PML} \\ 2\alpha^{PML} & 2\alpha^{PML} & 2\alpha^{PML} & 2\alpha^{PML} & 2\hat{Y}_{oz}\alpha^{PML} - 1 \end{bmatrix} \begin{bmatrix} {}_N V_1^i \\ {}_N V_2^i \\ {}_N V_3^i \\ {}_N V_4^i \\ {}_N V_5^i \end{bmatrix} + {}_N V_Z^{PML}. \quad (3.43)$$

which reduces to the standard nodal voltage ${}_N \tilde{V}_Z = {}_N V_Z$ as expressed in (3.17) when $\sigma_{sx} = \sigma_{sy} = 0$.

Following a TLM scatter each reflected voltage impulse V^r becomes the incident impulse on the adjacent transmission line at the next time step. As shown in Section 3.2.3, the connect equation for the standard shunt node has the following form

$$V_a^i(x + \Delta x, y, t) = V_b^r(x, y, t - \Delta t_x). \quad (3.44)$$

Since, the time delay in (3.44) can be interpreted through a Fourier transform as a phase shift i.e. $\mathcal{F}(t - \Delta t_x) \rightarrow e^{-j\omega\Delta t_x}$, therefore (3.44) can be represented as

$$V_a^i(x + \Delta x, y) = V_b^r(x, y)e^{-j\omega\Delta t_x}. \quad (3.45)$$

As discussed in Section 3.3, the process of mapping the TLM node transforms the transmission line propagation delay from a real valued to a complex valued

parameter. Therefore by substituting $\Delta t_x \rightarrow \tilde{\Delta t}_x = \Delta t \left(1 + \frac{\sigma_{sx}}{j\omega} \right)$, into (3.45) the form for the connect equation of the mapped shunt node is given as

$$V_a^i(x + \Delta x, y) = V_b^r(x, y) e^{-j\omega \Delta t_x} e^{-\Delta t \sigma_{sx}}. \quad (3.46)$$

By comparing (3.46) with (3.45) it is clear that in the mapped shunt node the connect equation is modified through the introduction of a scaling factor $e^{-\Delta t \sigma_{sx}}$ which is shown to be applied as an attenuation of the reflected pulses propagating along the axis of the coordinate stretching. For this reason the TLM criterion of impulse synchronism [3.12]-[3.13] is maintained since the real component of the time delay is the same for all directions. The full connect equation in the mapped shunt node is thus given as

$$\begin{aligned} {}_{N+1}V_1^i(x + \Delta x, y) &= {}_N V_3^r(x, y) e^{-\Delta t \sigma_{sx}}, \\ {}_{N+1}V_3^i(x - \Delta x, y) &= {}_N V_1^r(x, y) e^{-\Delta t \sigma_{sx}}, \\ {}_{N+1}V_2^i(x, y + \Delta y) &= {}_N V_4^r(x, y) e^{-\Delta t \sigma_{sy}}, \\ {}_{N+1}V_4^i(x, y - \Delta y) &= {}_N V_2^r(x, y) e^{-\Delta t \sigma_{sy}}, \\ {}_{N+1}V_5^i(x, y) &= {}_N V_5^r(x, y). \end{aligned} \quad (3.47)$$

3.3.2. Fields in the Mapped Shunt Node PML

As with the regular TLM node, the fields are obtained at the node centre. The electric and magnetic field components are given according to the field equivalence derived in (3.6)

$$\tilde{E}_z = -\frac{\tilde{V}_z}{\Delta l}, \quad (3.48a)$$

$$\tilde{H}_y = \frac{\tilde{I}_x}{\Delta l}, \quad \tilde{H}_x = \frac{\tilde{I}_y}{\Delta l}, \quad (3.48b)$$

where \tilde{I}_x and \tilde{I}_y , respectively, denote the currents flowing along the x - and y -directed transmission lines of the mapped shunt node which according to the current-voltage relation $\tilde{I} = \tilde{Y}V$ are given as

$$\tilde{I}_x = S_y Y_x (V_1^i - V_3^i), \quad \tilde{I}_y = S_x Y_y (V_4^i - V_2^i). \quad (3.49)$$

Equation (3.49) can also be re-expressed as

$$\tilde{I}_x = S_y I_x, \quad \tilde{I}_y = S_x I_y, \quad (3.50)$$

In order to obtain the time domain expressions for the currents \tilde{I}_x and \tilde{I}_y the variable transformation (3.37) must be applied to (3.50) in a similar manner to the derivation given in (3.38)-(3.41) for \tilde{V}_z .

Therefore, upon a s-domain transformation ($j\omega \rightarrow s$) the stretch factors become $S_x = 1 + \frac{\sigma_{sx}}{s}$, $S_y = 1 + \frac{\sigma_{sy}}{s}$ which, when substituted into (3.50) yield the expression

$$\begin{aligned} \tilde{I}_x &= S_y I_x = \left(1 + \frac{\sigma_{sy}}{s}\right) I_x, \\ \tilde{I}_y &= S_x I_y = \left(1 + \frac{\sigma_{sx}}{s}\right) I_y. \end{aligned} \quad (3.51)$$

By applying the bilinear transformation $s \rightarrow \frac{2}{\Delta t} \frac{1-z^{-1}}{1+z^{-1}}$ to (3.51) and upon an inverse Z-transformation the following time domain expressions for the currents are obtained

$$\begin{aligned} {}_N \tilde{I}_x &= \frac{{}_N I_x (2 + \sigma_{sy} \Delta t) + {}_{N-1} I_x (\sigma_{sy} \Delta t - 2) + 2 {}_{N-1} \tilde{I}_x}{2}, \\ {}_N \tilde{I}_y &= \frac{{}_N I_y (2 + \sigma_{sx} \Delta t) + {}_{N-1} I_y (\sigma_{sx} \Delta t - 2) + 2 {}_{N-1} \tilde{I}_y}{2}. \end{aligned} \quad (3.52)$$

Substituting equations (3.52) into (3.48b) allows the magnetic field components in mapped shunt node to be obtained.

3.3.3. Implementation Details

A key benefit of the mapped shunt node PML is the unified formulation it offers which allows an easy interfacing with the regular shunt node. By setting the PML conductivities to zero $\sigma_i = 0$, the mapped shunt node reduces to the standard shunt node. However, this is not the suggested mode of usage since the auxiliary variables introduced by the complex coordinate stretching result in a higher computational burden than necessary. The mapped shunt node PML is therefore only applied at the boundaries of the computational domain as depicted in Fig. 3.7. When used as a PML node the x and y conductivities, σ_x and σ_y , respectively, must be set according to the direction and strength of attenuation that is required. The different layouts of the PML surrounding the 2D computational domain are shown in Fig. 3.7. Particular attention must be given to the corner regions where attenuation in both x and y direction is simultaneously required. This region represents an overlap of PML layers and is implemented by setting $\sigma_x > 0, \sigma_y > 0$.

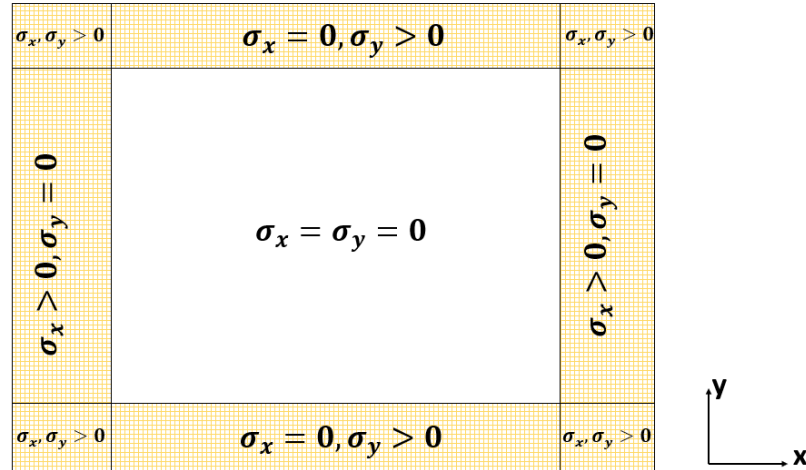


Figure 3.7 The PML layer specification surrounding the 2D computational domain. The values of σ_x and σ_y correspond to the degree of attenuation applied to the fields propagating in the x - and y -directions, respectively.

Finally, the overall computational procedure of the mapped shunt node follows the standard TLM schematic [3.3] but with the additional requirement to compute the PML voltage V_z^{PML} (3.40) and scale the reflected voltages by an attenuation factor $e^{-\Delta t \sigma_{si}}$.

3.3.4. Numerical Results

Following the developments made in the previous sections, various numerical experiments shall now be carried out to characterize the mapped shunt node PML. The objective is to examine the impact of the PML control parameters, e.g. type of the conductivity profile, the number of layers N_{PML} , and the theoretical reflection factor R_{th} , on the overall reflections generated by the PML.

The PML theoretical reflection factor R_{th} for normally incident waves is defined according to the relationship [3.10]

$$R_{th} = e^{-\frac{2\sigma_u L_{PML}}{(n+1)\epsilon_0 c}}, \quad (3.53)$$

where c is the wave velocity in free space, ϵ_0 is the permittivity of free space, n is the conductivity profile for which $n = 0, 1, 2$ and 3 denote a constant, linear, parabolic and cubic conductivity profile, respectively, σ_u is the conductivity at the outer layer of the PML. The total thickness of the PML medium is denoted as L_{PML} which is discretized into a total of N_{PML} layers according to $N_{PML} = \frac{L_{PML}}{\Delta l}$.

By rearranging (3.53), σ_u can be expressed as a function of the reflection to obtain

$$\sigma_u = -\frac{(n+1)\epsilon_0 c}{2L_{PML}} \ln(R_{th}) \quad (3.54)$$

The actual conductivity σ_p implemented at each TLM-PML node with index P can be expressed as a function of R_{th} and is given as [3.10],

$$\sigma_p(1) = -\frac{\epsilon_0 c}{2^n \Delta l N_{PML}^{n+1}} \ln R_{th}, \quad (3.55)$$

$$\sigma_p(P > 1) = \sigma_p(1) [(P)^{n+1} - (P-1)^{n+1}], \quad (3.56)$$

where $\sigma_p(1)$ denotes the conductivity of the first layer at the PML-Medium interface and $\sigma_p(P > 1)$ is the conductivity applied at subsequent PML layers for $1 < P \leq N_{PML}$.

To ensure a reliable and benchmarkable test, the mapped shunt node PML is applied to terminate the length of a WR28 rectangular metal waveguide. The configuration of the simulated waveguide is shown in Fig. 3.8 where the PML medium is applied at both ends of the waveguide to simulate an infinitely long guide. Hence the desired attenuation is for the fields propagating in the x direction (i.e. $\sigma_x > 0, \sigma_y = 0$). This simulation set up represents the canonical test for ABCs since the absorption performance for a wide range of incident angles and frequencies can be evaluated.

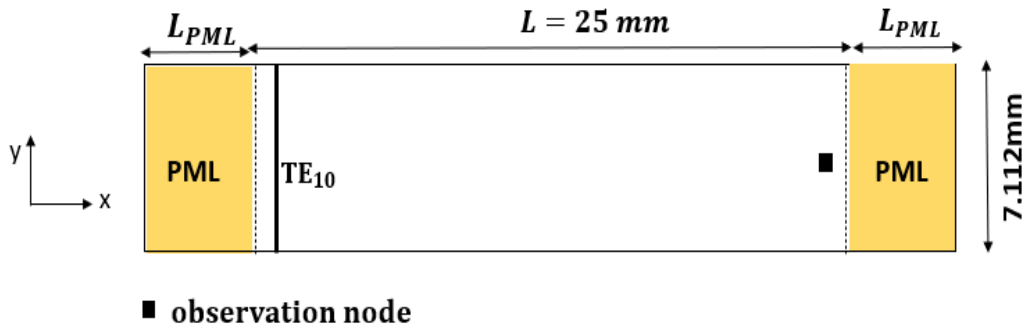


Figure 3.8 Geometry of the rectangular waveguide WR28

Unless otherwise stated, the geometry of the waveguide throughout the investigation carried out is 7.112 mm x 25 mm and this was uniformly discretized using $\Delta l = 0.22$ mm. The fundamental TE_{10} mode was excited at one end of the waveguide with an amplitude modulated Gaussian pulse with a centre frequency of 32.5 GHz and a bandwidth of 15 GHz. The observation point (shown as a black square in Fig. 3.8) was positioned at the other end of the guide—one node away from between the medium filling the waveguide (assumed to be air) and the PML interface.

The total field at the observation node, E_z , is a sum of the incident and the field reflected from the PML boundary. The reflection generated in the waveguide by the PML was computed using the reference waveguide which is identical to the one in Fig. 3.8 but with the length extended such that the reflections do not propagate back to the observation point within the time period of the simulation. The incident field, E_z^{ref} , was obtained from the reference structure. The reflected field at the observation node was thus extracted by subtracting the incident field E_z^{ref} from the total field E_z . This results in the following calculation for the reflection coefficient given in the frequency domain :

$$R_{dB}(f) = 20 \log_{10} \frac{\mathcal{F}(E_z(t) - E_z^{ref}(t))}{\mathcal{F}(E_z^{ref}(t))} = 20 \log_{10} \frac{\mathcal{F}(E_z^r(t))}{\mathcal{F}(E_z^{ref}(t))}, \quad (3.57)$$

where E_z denotes the z-polarized electric field value, and E_z^{ref} denotes the same quantity but obtained in the reference structure, $\mathcal{F}(\cdot)$ represents a discrete Fourier transform operator, and f represents the frequency.

3.3.4.1 Influence of the PML conductivity profile

In the discrete space, the sharp variation in the material properties from the medium to the PML layer generates high reflections which propagate back into the interior domain. Along with this, inter-node reflections arise due to the mismatch of transmission line impedance across adjacent PML nodes. To mitigate these effects, the conductivity across the PML must be gradually increased from a near zero value $\sigma_p(1) \sim 0 S/m$ at the first layer to a maximum value σ_{max} at the end layer. For illustrative purposes, a graph of different conductivity profiles across a PML with $R_{th}(dB) = -50 dB$ is shown in Fig. 3.9. As shown, the cubic and parabolic profiles provide a smoother grading than the linear and constant profiles and have a $\sigma_p(1)$ value closer to zero. The inverse relationship between the PML conductivity σ_p and $R_{th}(dB)$ is demonstrated in Fig. 3.10 As shown, a lower theoretical reflection level $R_{th}(dB) \rightarrow -\infty$ results in a higher conductivity $\sigma_p(1)$. This will in turn cause the propagating

waves to experience a larger variation at the medium to PML interface which is expected to increase the transitional reflections.

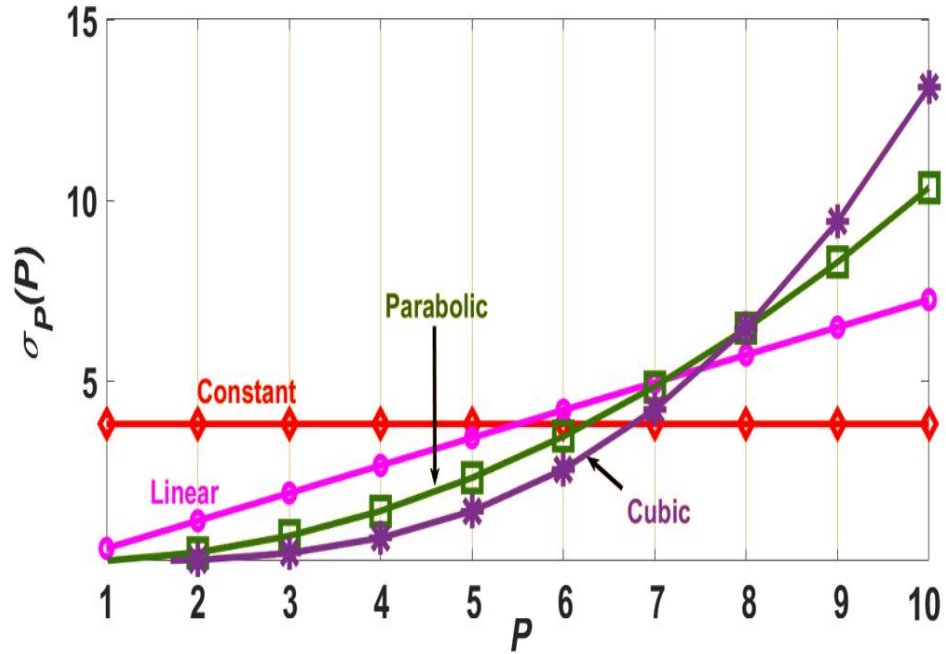


Figure 3.9 Constant, linear, parabolic and cubic conductivity profiles applied across a 10 layer PML with theoretical reflection factor $R_{th}(dB) = -50 dB$.

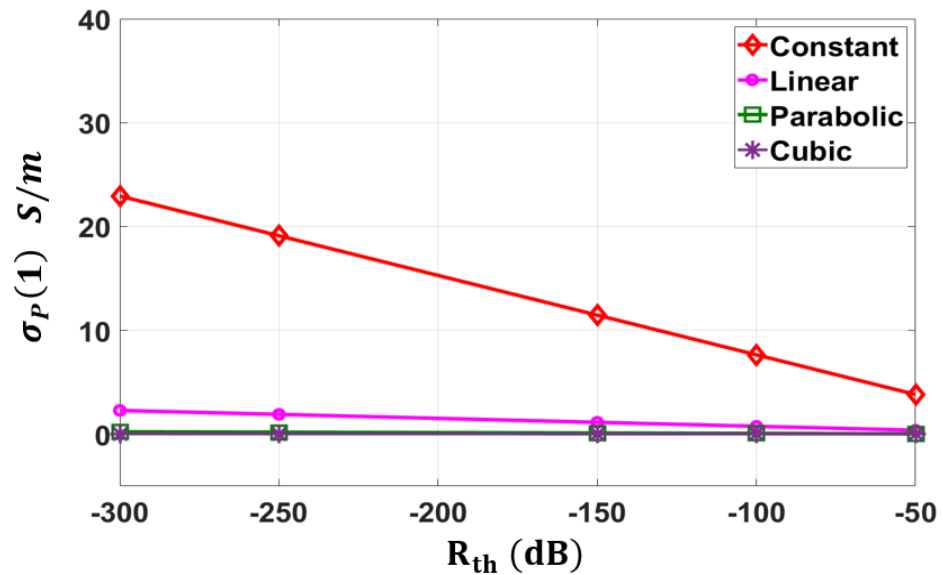


Figure 3.10 Plot showing the relationship between the conductivity at the first layer $\sigma_P(1)$ and theoretical reflection factor $R_{th}(dB)$ for different conductivity gradings

The first investigation therefore examines the influence on PML performance of the conductivity gradings across the PML medium. The profiles studied were the constant, linear, parabolic and cubic gradings respectively. In this test, the waveguide was truncated by 25 layers of a mapped shunt node PML backed by a PEC boundary and the theoretical reflection factor was set to $R_{th} = -100$ dB. The reflection coefficients obtained from the conductivity profiles studied are plotted as a function of frequency in Fig. 3.11. As expected, the highest reflection is demonstrated by the uniform conductivity profile with a reflection coefficient in the range of -59 dB to -70 dB across the bandwidth of operation. The reflections produced when employing the uniform conductivity profile solely arise at the medium-to-layer interface, and whilst the absorption at the interface can be improved by lowering the conductivity and substantially increasing the PML thickness this results in a significant increase in computational costs. The benefits of a graded conductivity profile are shown in Fig. 3.11 by the lower reflection levels achieved compared to the constant profile case. The best performing conductivity profile is shown to be the parabolic grading which is in agreement with the findings generally reported [3.6],[3.10]. Consequently, the parabolic profile is used for the subsequent investigations.

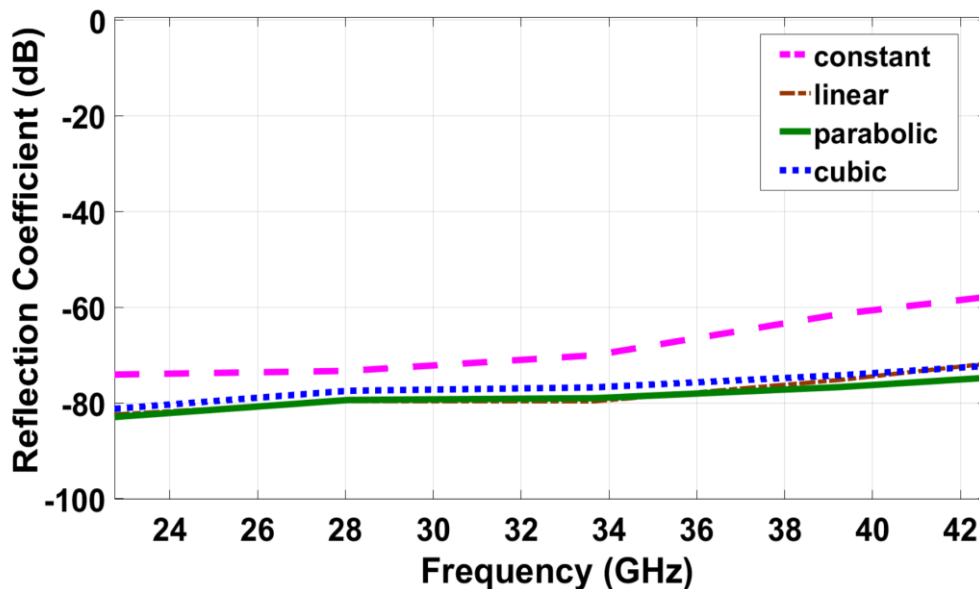


Figure 3.11 Numerical reflection coefficients of the mapped shunt node PML with conductivity profiles: uniform, linear, parabolic, cubic, as simulated for the waveguide WR28 structure shown in Fig. 3.10 filled with air.

3.3.4.2 Influence of the number of PML layers N_{PML}

Next, the effect of the number of PML layers N_{PML} on the overall reflection behaviour is evaluated. The simulation configuration was maintained as in the previous study. The relationship between the numerical reflections and the theoretical reflection factor for different number of PML layers is shown in Fig. 3.12. As shown, the reflections generated by the mapped shunt node PML can be significantly reduced for a given theoretical reflection factor R_{th} (dB) by increasing the number of PML layers used. This is largely due to the increase in the damping experienced as the waves propagate through the medium. However, from the same plot, it can also be seen that an optimal value of R_{th} (dB) exists which achieves the lowest reflections for a given choice of N_{PML} . For example, when $N_{PML} = 25$, the optimal value of R_{th} (dB) is shown to be approximately -100 dB and any further decrease in the value of R_{th} (dB) results in an increase in the numerical reflections. Generally, finding the optimum R_{th} (dB) for a given N_{PML} is not straightforward and in most cases requires a tuning process as will be described in more details in Chapter 5. The appropriate design choice to be made is therefore decided based on the trade-off between the accuracy required and the computational expense incurred from increasing the value of N_{PML} .

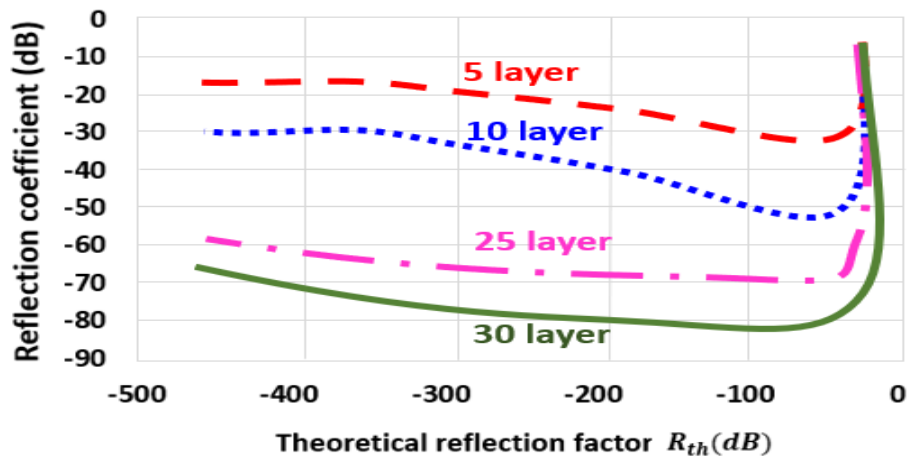


Figure 3.12 Numerical reflection coefficients obtained using the mapped shunt node PML as a function of theoretical reflection factor R_{th} (dB) for different number of PML layers N_{PML} for the simulated termination of waveguide WR28 as shown in Fig. 3.8.

3.3.4.3 Reflection Performance of the Mapped Shunt Node PML in Lossy and Dielectric Media

The reflections generated by the mapped shunt node PML in a lossy dielectric host were investigated by simulating the same waveguide but filled with the following materials: (a) $\epsilon_r = 1, \sigma_e = 0 \text{ S/m}$ (freespace); (b) $\epsilon_r = 5, \sigma_e = 0 \text{ S/m}$; (c) $\epsilon_r = 1, \sigma_e = 0.5 \text{ S/m}$ and (d) $\epsilon_r = 5, \sigma_e = 0.5 \text{ S/m}$. In this test, the waveguide was truncated by 25 PML layers backed by a PEC boundary. The theoretical reflection factor was set to $R_{th}(dB) = -100 \text{ dB}$. The results for numerical reflections are presented in Fig. 3.13 and show that good absorption performance ($>70 \text{ dB}$) is maintained even when incorporating lossy media, whilst an increase in the medium's relative permittivity (i.e. $\epsilon_r > 1$) is shown to reduce the overall absorption (i.e. higher reflection).

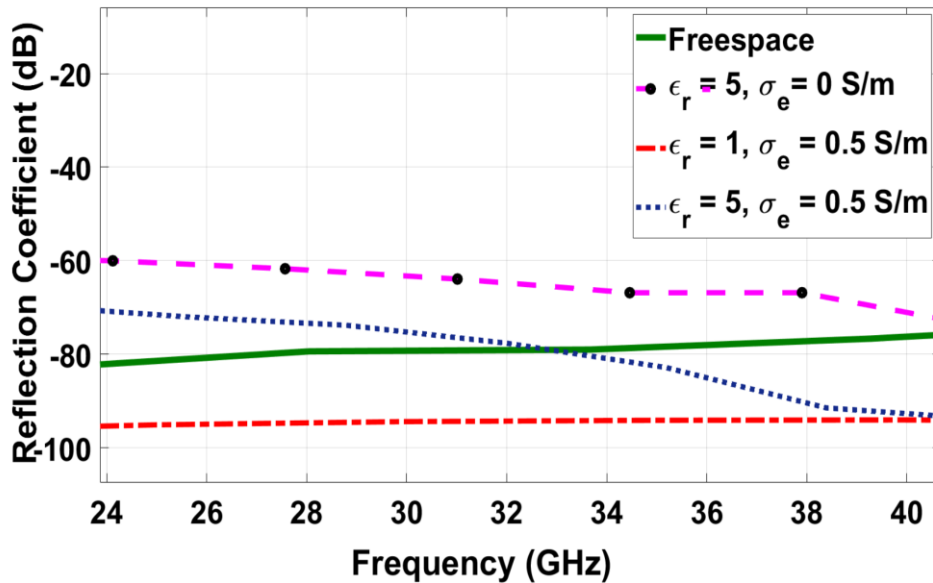


Figure 3.13 Numerical reflection coefficient of the mapped shunt node PML for a WR28 waveguide filled with lossy dielectric media

3.3.4.4 Comparison with Published 2D TLM-PML Schemes

The reflections generated by the mapped shunt node PML were compared against the results obtained from waveguides terminated by the split-field TLM-PML formulation presented in [3.14] and a conventional TLM matched boundary [3.3]. As shown in Fig. 3.14, both PML schemes demonstrate better absorption (>50 dB) compared to the matched boundary termination and better absorption (>15 dB) than the split-field TLM-PML reported in [3.13]. Whilst the matched termination offers the most computationally efficient method to truncate TLM meshes, its absorption performance is however severely degraded by waves incident on the boundary at an oblique angle. This explains the high reflections generated in this case. It can be seen from Fig. 3.14, that a comparable level of absorption is achieved by both PML schemes where reflection levels lower than -76 dB are obtained in the mapped shunt node PML over the entire band of operation. Nevertheless, a clear advantage of the mapped TLM-PML formulation is its applicability to terminating both lossless and lossy dielectric media. In such applications, the split field based TLM-PML schemes [3.13] – [3.14] fail since the node conductance G_{ez} is naturally employed by these formulations to enforce the attenuation of propagating modes in the x and y directions. Hence G_{ez} cannot be employed to suitably model the electric losses represented by the electric conductivity σ_{ez} .

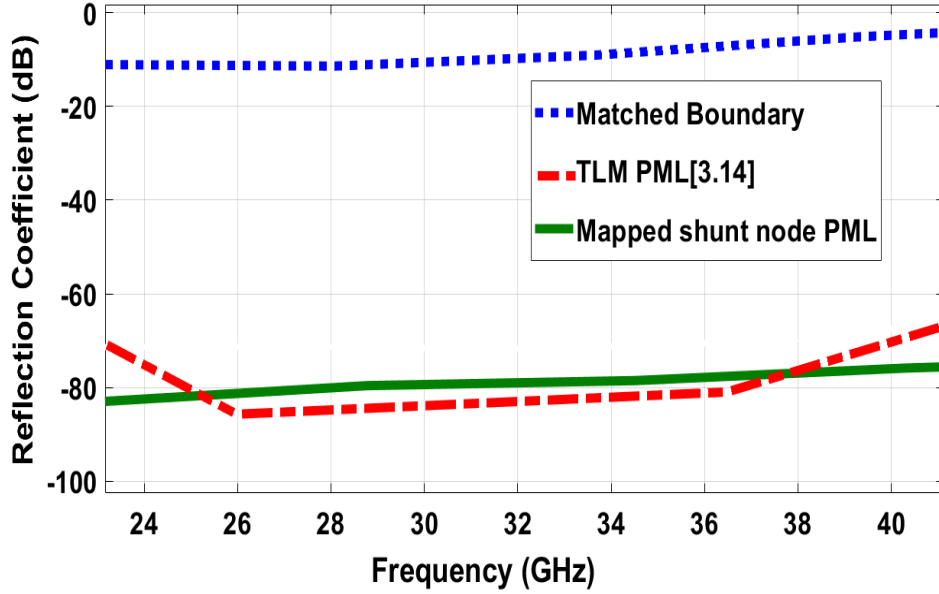


Figure 3.14 Numerical reflection coefficients extracted from a TLM simulation of an empty WR28 rectangular waveguide with various boundary conditions applied.

3.3.4.5 Topical 2D Application: Scattering from NACA0015 Airfoil

For further illustrative purposes the mapped shunt node PML was applied to a topical wave-structure application, involving the plane wave scattering of a PEC airfoil with profile Naca0015 [3.19].

The equation which defines the shape of the Naca0015 airfoil is given as

$$\pm y_t = 75(0.2969\sqrt{x} - 0.1260x - 0.3516x^2 + 0.2843x^3 - 0.1015x^4), \quad (3.58)$$

where y_t is the thickness given at a value of position $x \in [0,1]$.

The airfoil structure was placed in a $0.6 \text{ m} \times 2 \text{ m}$ computational domain which was uniformly meshed with $\Delta l = 5 \text{ mm}$. The plane wave was incident on the airfoil

along the x direction. Figures 3.15a and b show the electric field intensity (in dB) at time $t = 30$ ns, in simulations where a 10 layer mapped TLM-PML and matched boundary termination were applied, is shown in respectively. The high absorbing capability of the PML is clearly demonstrated by how quickly the overall energy is attenuated in Fig. 3.15b compared to Fig. 3.15a where the matched boundary is employed.

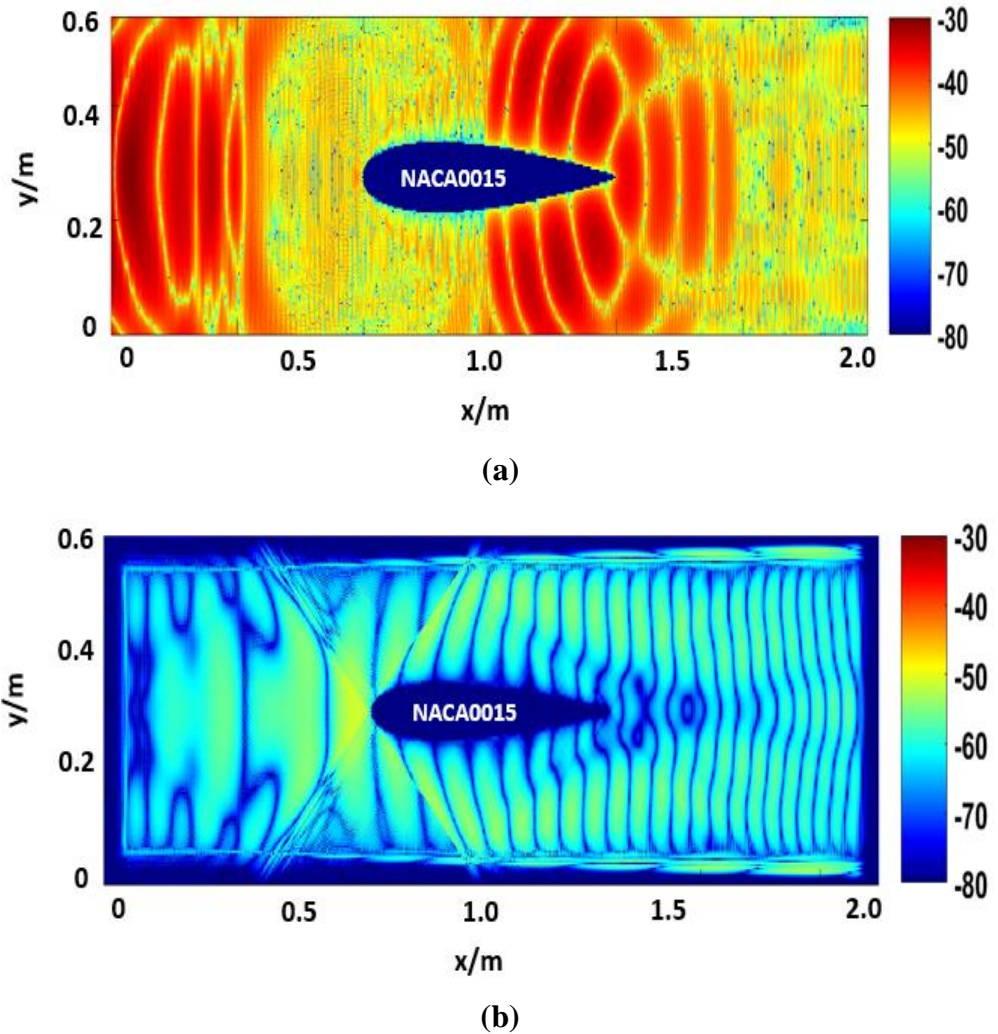


Figure 3.15 Scattered electric field intensity captured at $t = 30$ ns from a NACA0015 airfoil with (a) TLM matched boundary, (b) 20 layer PML applied at all edges of the domain

Finally, it is reported that numerical instability has not been observed in any of the investigations carried out in this work. This further demonstrates the utility of the proposed formulation.

3.4 Summary

This chapter introduced the TLM theory through its core principles. The 2D shunt and series TLM nodes were described and their analogy with Maxwell's equations was derived. Subsequently, this led to the development of a framework for implementing the SC PML in TLM which was formulated for the 2D TLM shunt node. The PML formulation was developed based on establishing an analogy between the equations describing the TLM shunt node and the modified (stretched) second-order wave equations.

The performance of the developed method was studied through a variety of numerical tests based on the canonical waveguide application. The first investigation carried out examined the influence of different conductivity gradings across the PML medium on the PML performance. The constant, linear, parabolic and cubic conductivity profiles were studied. The benefits of a graded conductivity profile were demonstrated by the comparatively lower reflection levels achieved compared to the constant profile case. The best performing conductivity profile is shown to be the parabolic grading which is in agreement with the findings generally reported [3.6],[3.10].

Next, the relationship between the numerical reflections and the theoretical reflection factor for different number of PML layers was investigated. Results show that the reflections generated by the mapped shunt node PML can be significantly reduced for a given theoretical reflection factor R_{th} (dB) by increasing the number of PML layers used. This behaviour arises because of the increase in the damping experienced as the waves propagate through the medium. However, it was also seen that an optimal value of the theoretical reflection factor R_{th} (dB) exists which achieves the lowest reflections for a given choice of N_{PML} .

The ability of the mapped shunt node PML in terminating lossy dielectric media was demonstrated. The numerical reflections generated show that good absorption performance (>70 dB) is maintained even when incorporating lossy media. As a final characterization test, the performance of the mapped shunt node PML was compared against the split-field TLM-PML formulation presented in [3.14] and a conventional TLM matched boundary [3.3]. Both PML schemes demonstrated better absorption (>50 dB) compared to the matched boundary termination. Nonetheless, the clear advantage of implementing a SC PML formulation, is the ability to terminate both lossless and lossy dielectric media. In such applications, the split field based TLM-PML schemes [3.13] – [3.14] fail since the node conductance G_{ez} is naturally employed by these formulations to enforce the attenuation of propagating modes in the x and y directions. Hence G_{ez} cannot be employed to suitably model the electric losses represented by the electric conductivity σ_{ez} .

For further illustrative purposes the strong absorbing capability of the mapped shunt node PML was demonstrated in a topical application, involving the plane wave scattering from a PEC airfoil with profile Naca0015. Compared to the matched boundary termination the scattered field in the computational domain was shown to be more rapidly attenuated when employing the mapped shunt-node PML.

No instabilities were observed in all the tests carried out, demonstrating the utility of the proposed formulation. Owing to the simplicity of the developed method its extension to more advanced 3D symmetrical condensed nodes shall be the subject of Chapter 4.

References

- [3.1] P. B. Johns, and R. L. Beurle, “Numerical solution of two dimensional scattering problems using a transmission line matrix”, Proc. IEEE, 118,(9), pp. 1203-1208, 1971.

- [3.2] P. B. Johns., “A simple, explicit and unconditionally stable numerical routine for the solution of the diffusion equations”, *Int. J. Numer. Methods Eng.*, vol. 11, pp. 1307-1328, 1977.
- [3.3] C. Christopoulos, “The transmission-line modeling method: TLM” (Institute of Electrical and Electronics Engineers, New York, 1995).
- [3.4] B. Engquist, and A. Majda, “Absorbing boundary conditions for the numerical simulation of waves,” *Math. Comp.*, vol. 31, pp. 629-651, 1977.
- [3.5] R. L. Hidgon, “Absorbing boundary conditions for difference approximations of the multi-dimensional wave equation,” *Math. Comp.*, vol. 47, pp. 437-459, Oct. 1986.
- [3.6] J.P. Bérenger, “A perfectly matched layer for the absorption of electromagnetic waves”, *J. Comput. Phys.*, 114, (1), pp. 185–200, 1994.
- [3.7] W.C Chew, and W.H Weedon,. “A 3D perfectly matched medium from modified Maxwell’s equations with stretched coordinates”, *Microwave and Optical Tech. Lett.*,7, (13), pp. 599–604, 1994.
- [3.8] Z. S. Sacks, D. M. Kingsland, R. Lee, and J. F. Lee, "A perfectly matched anisotropic absorber for use as an absorbing boundary condition," *IEEE Trans. Antennas Propagat.*, vol. 43, pp. 1460-1462, Dec. 1995.
- [3.9] S. D. Gedney, “An anisotropic perfectly matched layer absorbing medium for the truncation of FDTD lattices,” *IEEE Trans. Antennas Propagat.*, vol. 44, pp. 1630–1639, Dec. 1996.
- [3.10] J.P. Bérenger, ‘Perfectly matched layer (PML) for computational electromagnetics. Synthesis lectures on computational electromagnetics’, Morgan and Claypool, 2007
- [3.11] M. Kuzuoglu, and R. Mittra, "Mesh truncation by perfectly matched anisotropic absorbers in the finite-element method," *Microwave Opt. Technol. Lett.*, vol. 12, pp. 136-140, June 1996.
- [3.12] T. Rylander, and J-M. Jin. “Perfectly matched layer in three dimensions for the time-domain finite element method applied to radiation problems.” *IEEE Trans. Antennas Propagat.*, vol. 53(4), pp.1489–1499, April 2005.
- [3.13] C. Eswarappa, and W.J.R Hoefler, “Implementation of Bérenger absorbing boundary conditions in TLM by interfacing FDTD perfectly matched layers”, *Electron. Lett.*, 31, (15), pp. 1264-1266, 1995.

- [3.14] N. Pena, and M.M. Ney “A new TLM node for Berenger’s perfectly matched layer”, IEEE Microwave and Guided Wave Lett., 6, (11), pp. 410-412, 1996.
- [3.15] H.G. Dantanarayana, “Application of TLM for optical microresonators”. PhD thesis, University of Nottingham, 2012
- [3.16] W.J.R. Hoefer, “The transmission-line matrix method—Theory and applications”, IEEE Trans. Microwave Theory Tech., 33, pp. 882-893, 1985.
- [3.17] V. Trenkic, C. Christopoulos, and T.M. Benson “A unified approach to the derivation of TLM node parameters” in First International Workshop on TLM, Victoria, Canada, pp.23-26, 1995.
- [3.18] J.Paul , C. Christopoulos, and D.W.P. Thomas, “Generalized material models in TLM – Part 1: Materials with frequency dependent properties”, IEEE Trans. Antennas and Propagation, 50, (7), pp. 997-1004, 1995.
- [3.19] H. Akbiyik, H. Yavuz, and Y.E. Akansu , “Investigation of the effect of the plasma actuators vertically placed on the spanwise of NACA0015 airfoil” in Proc. 8th Int. Exergy, Energy Environ. Symp., pp. 593–597, 2013.

Chapter 4

A Complex Domain Mapping of the SCN

In this chapter, the 2D mapped TLM-PML theory is extended to 3D TLM problems. The symmetrical condensed node (SCN) variant of the 3D TLM node is considered due to its simplicity and popularity in practice. The theory described will include the derivation of the full scatter equations for the mapped 12-port standard SCN suitable for terminating homogenous media and the scatter equations for the mapped 15-port hybrid SCN effective in terminating general inhomogeneous and lossy media.

4.1. Introduction

Reducing the high computational demand of electromagnetic simulations is a prime motivator of majority of the CEM techniques developed today. In the case of 3D open boundary problems, it is critically important for the viability of large-scale computations to minimize the volume of free space that needs to be explicitly modelled; as well as to guarantee appropriate and highly accurate solutions are computed. The PML has been largely optimized for the 3D FDTD where various implementation approaches and PML extensions have been explored. On the other hand, the limited PML formulations in 3D TLM have all implemented the PML theory by imposing a direct modification of the field behavior at the TLM node centers. These models rely on the introduction of stubs to achieve the required field attenuations.

The pioneering 3D TLM-PML development was based on a coupling between the TLM-FDTD network [4.1]. This however suffered from a degradation in its absorption performance due to the non-physical reflections generated at the non-

uniform TLM-FDTD interface. A number of uniform TLM developments have since been proposed and demonstrated for the 3D TLM symmetrical condensed node (SCN). The initial development was proposed in [4.2] which implemented the PML by splitting each field component into two subcomponents and applying anisotropic electric/magnetic conductivities to attenuate along each direction of propagation. The process of field splitting resulted in an increase in total voltage stored per node. A second split-field based SCN-PML was developed in [4.3] which employed a direct discretization of (2.4) through a centered differencing and averaging of the PML equations. This demonstrated similar absorption performance to [4.2] and had the advantage of requiring less storage per node. A limitation with the formulation proposed in [4.3] however is the singularities that arise in the inductive stubs which prevents operation at the maximum time step permitted. The singularity issues reported in [4.3] were improved in [4.4] by introducing a damping factor to attenuate evanescent fields and this was shown to improve the temporal behavior by delaying the occurrence of instabilities. Nonetheless, due to the inherent limitation of the split-field PML theory the formulations proposed in [4.1]-[4.4] are less suitable to applications involving lossy media. Results from a stretched coordinate (SC) SCN-PML node have been demonstrated for terminating 3D waveguide structures [4.5]. This employed the use of the Z-transform to impose the frequency dependent stretch variables on the fields of the SCN node. The absorption behavior was shown to yield comparable results with previous SCN-PML schemes, however, a clear disadvantage with this implementation is the instabilities which arise. In addition, its application is limited since the extensions to terminating non-waveguide structures is not clear from the theory provided.

Whilst the published SCN-PML implementations show a good agreement in their absorption performance, with all obtaining absorption levels of approximately 65 dB, they also exhibit a weak temporal stability, which generate exponentially growing solutions in the problem domain. This phenomenon is practically unacceptable as it causes unphysical gain (instability) and its removal is a prime motivator of the work carried out in this thesis.

Chapter 3 presented a new framework for implementing the stretched coordinate PML in 2D TLM which was developed based on an analogy of mapping the TLM node to a complex stretched space. Unlike [4.5], which introduces the stretched coordinate PML theory as a correction of fields, in the proposed formulation the PML coordinate stretching is mapped onto transmission line constitutive parameters, namely characteristic impedances/admittances and the timestep. Therefore, leading to a derivation of transformed RLC parameters and subsequent modifications of the scatter and connect algorithms. Results from the canonical waveguide application demonstrated the effectiveness of the model compared to existing 2D TLM-PML schemes and the simple matched boundary condition. Additionally, no instability was reported. Owing to the excellent performance demonstrated, this chapter shall extend the mapping approach to the 3D TLM-PML case. The theory describing the complex domain mapping of the general symmetrical condensed node is thus presented.

Chapter 4 is structured as follows. In Section 4.2 the structure of the general SCN is presented and the underlying medium to circuit equivalence is introduced. The standard 18-port and 15-port hybrid SCN configurations are also presented based on general constitutive relations. In Section 4.3, a new configuration of the SCN is developed based on a direct mapping between Maxwell's equations in the stretched coordinate space and the transmission line parameters of the SCN. This implementation is referred to as the **mapped SCN-PML**. Modified scatter equations due to the mapping are presented in Section 4.3.1. The complete scatter equations for the mapped 12-port SCN and the mapped 15-port hybrid SCN are derived in sections 4.3.2 and 4.3.3, respectively. The full implementation details of mapped SCN-PML is presented in Section 4.3.4 and various strategies to optimize the computational efficiency are discussed. Section 4.4 summarizes the chapter.

4.2 The Symmetrical Condensed Node

The schematic of the SCN is shown in Fig.4.1 which describes the SCN topology mapped to a block of space with dimensions given as $\Delta x \times \Delta y \times \Delta z$ and material properties $\mu = \mu_r \mu_0$ and $\epsilon = \epsilon_r \epsilon_0$. This model accounts for all three

coordinate directions and field polarizations in a 3D geometry. The SCN introduces 12 voltages in the form of $V_{i\alpha j}$, where i represents the direction and j the polarization of the line for which $i, j \in \{x, y, z\}$ and $i \neq j$ and $\alpha \in \{n, p\}$ indicates the position of the line on the negative (n) or positive (p) side relative to the origin of coordinates at the center of the node. Each transmission arm supports the propagation of a pair of polarized fields. Therefore, there is an associated pair of characteristic impedances denoted as Z_{ij}, Z_{ik} (for which $i, j, k \in \{x, y, z\}$ and $i \neq j \neq k$ and corresponding admittances expressed as Y_{ij}, Y_{ik}) along each arm, which results in a total of 12 characteristic impedances per node. Each node supports the propagation of pulses to neighboring nodes via the 12 ports of the SCN where the node to node transition time is defined by the time step Δt [4.6]-[4.8].

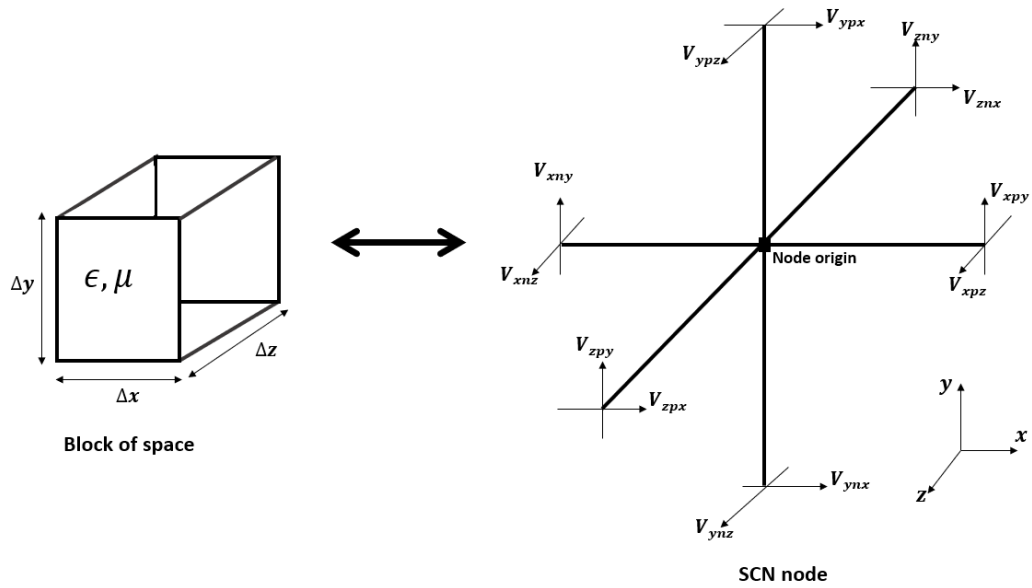


Figure 4.1. Diagram showing the topology of the Symmetrical Condensed Node (SCN) modelling a $\Delta x \times \Delta y \times \Delta z$ block of space.

4.2.1 SCN General Constitutive Relations

The correct modelling in TLM relies on establishing an appropriate equivalence between the material space and the TLM node circuit parameters. The

following equations have been shown to relate the total node capacitance C_t^j and inductance L_t^j with the geometric and material properties of the SCN node [4.6]-[4.8]

$$C_t^j = \epsilon_{jj} \frac{\Delta i \Delta k}{\Delta j}, \quad (4.1)$$

$$L_t^j = \mu_{jj} \frac{\Delta i \Delta k}{\Delta j}, \quad (4.2)$$

where indices $i, j, k \in \{x, y, z\}$ and $i \neq j \neq k$ denote the coordinate directions, ϵ_{jj} and μ_{jj} are the diagonal components of the permittivity and permeability tensors of the medium which have zero off diagonal elements (i.e. $\epsilon_{ij} = \mu_{ij} = 0$, for $i \neq j$). Given the compact form in (4.1)-(4.2) the total node capacitance and inductance, for example, in the x direction are therefore expressed as

$$C_t^x = \epsilon_{xx} \frac{\Delta y \Delta z}{\Delta x}, \quad (4.3)$$

$$L_t^x = \mu_{xx} \frac{\Delta y \Delta z}{\Delta x}, \quad (4.4)$$

According to the TLM general constitutive relation [4.8], the total capacitance and inductance are made up contributions from the distributed line inductances and capacitances as well as the stubs. This therefore results in the following relation

$$C_t^j = C_{ij} \Delta i + C_{kj} \Delta k + C_j^o, \quad (4.5)$$

$$L_t^j = L_{ik} \Delta i + L_{ki} \Delta k + L_j^s, \quad (4.6)$$

where L_{ik} and C_{ij} respectively denote the distributed line inductance and capacitance and L_j^s and C_j^o denote the inductive and capacitive stubs respectively.

Substituting (4.1) - (4.2) into (4.5) - (4.6) obtains the following equations for the j -direction

$$\epsilon_{jj} \frac{\Delta i \Delta k}{\Delta j} = C_{ij} \Delta i + C_{kj} \Delta k + C_j^o, \quad (4.7)$$

$$\mu_{jj} \frac{\Delta i \Delta k}{\Delta j} = L_{ik} \Delta i + L_{ki} \Delta k + L_j^s, \quad (4.8)$$

which after applying the transmission line relations $C_{ij} \Delta i = \Delta t Y_{ij}$ and $L_{ij} \Delta i = \Delta t Z_{ij}$ are re-expressed in terms of line admittances as follows

$$\epsilon_{jj} \frac{\Delta i \Delta k}{\Delta j \Delta t} = Y_{ij} + Y_{kj} + \frac{Y_j^o}{2}, \quad (4.9)$$

$$\mu_{jj} \frac{\Delta i \Delta k}{\Delta j \Delta t} = Z_{ik} + Z_{ki} + \frac{Z_j^s}{2}, \quad (4.10)$$

where parameter Y_j^o denotes the j polarised characteristic admittance of the open circuit stubs and Z_j^s denotes the j polarized characteristic impedance of the short circuit stubs. The transit time along the length of each stub is equal to $\frac{\Delta t}{2}$ since each pulse must make a round trip, therefore the relationship $\frac{Y_j^o \Delta t}{2} = C_j^o$ and $\frac{Z_j^s \Delta t}{2} = L_j^s$ holds. Traditionally the transmission line (TL) impedances are set to model the background medium and the stubs are introduced to handle deficiencies in the node.

From equations (4.9)-(4.10) two commonly used SCN configurations can be constructed, namely SCN and Hybrid SCN (HSCN) nodes which are now summarized:

SCN (18-port) : In the standard SCN configuration the transmission line impedances are constant and are set to model the intrinsic impedance of the background medium $Z_{ij} = Z_{jk} = Z_0$. Therefore the stub impedances and admittances are set by re-arranging equations (4.9) and (4.10) to obtain

$$Y_j^o = 2Y_0 \left(\epsilon_{rj} \frac{\Delta i \Delta k}{c \Delta j \Delta t} - 2 \right), \quad (4.11)$$

$$Z_j^s = 2Z_0 \left(\mu_{rj} \frac{\Delta i \Delta k}{c \Delta j \Delta t} - 2 \right), \quad (4.12)$$

where $c = \frac{1}{\sqrt{\epsilon_0 \mu_0}}$ and ϵ_{rj} and μ_{rj} are the relative permittivity and permeability, respectively, of the medium. From equations (4.11) and (4.12) all geometric and material inhomogeneity are compensated for by both stubs in a straightforward manner. This therefore results into six stub ports added into the structure of the SCN. To ensure stability, all stub values must be positive and as such a maximum time step is enforced by the relations

$$\Delta t \leq \frac{\epsilon_{rj} \Delta i \Delta k}{2c \Delta j}, \quad (4.13)$$

$$\Delta t \leq \frac{\mu_{rj} \Delta i \Delta k}{2c \Delta j}, \quad (4.14)$$

The TLM time synchronism criteria requires a constant time step is used across all nodes in the TLM mesh [4.8]. To ensure this, equations (4.13) and (4.14) are computed for all nodes in the TLM mesh and the smallest value is used to determine the maximum time step in the entire TLM simulation.

Hybrid SCN (15-port): Compared to the 18-port SCN, the hybrid symmetrical condensed node (HSCN) scheme supports the use of link lines to model the required inductance at the node [4.9]-[4.10]. This therefore eliminates the use of inductive stubs (i.e. $Z_j^s = 0$ since $L_j^s = 0$) thus reducing the number of node ports from 18 to 15. In this manner a reduction in memory usage is gained since there is no requirement to store and compute inductive stub voltages. In this scheme the open circuit stubs Y_j^o are used to model the node deficits. The resulting characteristic impedance/admittance of the link lines are therefore defined by imposing the condition $Z_j^s = 0$ and rearranging (4.9) – (4.10) to yield

$$Z_{ij} = Z_{ji} = Z_0 \mu_{rj} \frac{\Delta i \Delta k}{2c \Delta j \Delta t}, \quad (4.15)$$

$$Y_{ij} = Y_{ji} = \frac{1}{Z_{ij}} = \frac{1}{Z_{ji}}, \quad (4.16)$$

$$Y_j^o = Y_0 \left(\frac{2\epsilon_{rj}\Delta i\Delta k}{c\Delta j\Delta t} - \frac{4c\Delta t}{\Delta k} \left(\frac{\Delta k}{\mu_{rk}\Delta i} + \frac{\Delta i}{\mu_{ri}\Delta k} \right) \right), \quad (4.17)$$

Like the basic SCN, stability is achieved in the HSCN by ensuring the capacitive stubs Y_j^o are assigned non-negative values. To enforce this condition a maximum time step limit is defined given as

$$\Delta t \leq \frac{1}{2c} \sqrt{\frac{2\epsilon_{rj}}{\frac{1}{\mu_{rk}\Delta i^2} + \frac{1}{\mu_{ri}\Delta k^2}}}}, \quad (4.18)$$

Upon close inspection of equation (4.18) it can be shown that in the HSCN the maximum time Δt_{max} step achievable lies within the range of [4.11]

$$\frac{\Delta l}{2c} \leq \Delta t_{max} \leq \frac{\Delta l\sqrt{2}}{2c}, \quad (4.19)$$

where Δl represents the smallest node dimension. Comparing (4.14) to (4.19) a higher maximum time step can be achieved by the HSCN in some cases compared to the basic SCN. This fact as well as the lower memory requirement constitutes a major advantage of the HSCN over to the basic SCN.

All SCN configurations model losses using matched stubs which can be used to represent both electric and magnetic losses. Similar to the 2D nodes, a shunt conductance G_{ej} models j -directed electric conductivities using relations [4.8]

$$G_{ej} = \sigma_{ej} \frac{\Delta i\Delta k}{\Delta j}, \quad (4.20)$$

whilst the series resistance models j -directed magnetic conductivities according to the relation

$$R_{mj} = \sigma_{mj} \frac{\Delta i \Delta k}{\Delta j}. \quad (4.21)$$

Since all lossy stubs are assumed to be matched transmission lines (i.e. infinitely long link lines), then they reflect no voltage back to the node. The only contribution made by the lossy stubs is therefore to dissipate energy [4.7].

4.2.2 Scatter and Connect Algorithms

As discussed in Chapter 3, the TLM scatter and connect algorithms represent the central process through which the discrete implementation of Huygens principle is realized. Following the initial injection of energy into the network the TLM simulation process follows an iterative procedure of alternating between scattering at nodes and propagating each scattered pulse to link lines of adjacent nodes. Like the 2D TLM models the full scatter equation of the SCN can be derived using an equivalent network approach as described in [4.12], [4.13]. This approach develops on the understanding that the SCN topology is composed of constituent 2D shunt and series circuits representing the various field polarizations. As such, the 2D shunt and series circuits have some contributions to the scattering at each node. The overall scattering procedure in the SCN is compactly written as [4.12], [4.13]

$$\begin{aligned} V_{inj}^r &= V_j \pm I_k Z_{ij} - V_{ipj}^i, \\ V_{ipj}^r &= V_j \mp I_k Z_{ij} - V_{inj}^i, \\ V_{oj}^r &= V_j - V_{oj}^i, \\ V_{sj}^r &= I_j Z_{sj} - V_{sj}^i, \end{aligned} \quad (4.24)$$

where V_j and I_j denote the total j -directed voltage and current respectively which are computed using the 2D Thevenin circuits presented in chapter 3. The upper and lower signs are applied respectively as follows using the indices rule

$$(i, j, k) \in \{(x, y, z), (y, z, x), (z, x, y)\}$$

and

$$(i, j, k) \in \{(x, z, y), (y, x, z), (z, y, x)\}. \quad (4.25)$$

Like the 2D TLM nodes the connect procedure in the SCN involves a straightforward swapping of reflected pulses between link lines of adjacent nodes. The connect algorithm in the basic SCN is thus expressed as below [4.7]

$$\begin{aligned} N_{+1}V_{ynx}^i(x, y + \Delta y, z) &= N V_{ypx}^r(x, y, z), \\ N_{+1}V_{znx}^i(x, y, z + \Delta z) &= N V_{zpx}^r(x, y, z), \\ N_{+1}V_{xny}^i(x + \Delta x, y, z) &= N V_{xpy}^r(x, y, z), \\ N_{+1}V_{zny}^i(x, y, z + \Delta z) &= N V_{zpy}^r(x, y, z), \\ N_{+1}V_{ynz}^i(x, y + \Delta y, z) &= N V_{ypz}^r(x, y, z), \\ N_{+1}V_{xnz}^i(x + \Delta x, y, z) &= N V_{xpz}^r(x, y, z), \\ N_{+1}V_{ypz}^i(x, y - \Delta y, z) &= N V_{ynz}^r(x, y, z), \\ N_{+1}V_{zpy}^i(x, y, z - \Delta z) &= N V_{zny}^r(x, y, z), \\ N_{+1}V_{zpx}^i(x, y, z - \Delta z) &= N V_{znx}^r(x, y, z), \\ N_{+1}V_{xpz}^i(x - \Delta x, y, z) &= N V_{xnz}^r(x, y, z), \\ N_{+1}V_{xpy}^i(x - \Delta x, y, z) &= N V_{xny}^r(x, y, z), \\ N_{+1}V_{ypx}^i(x, y - \Delta y, z) &= N V_{ynx}^r(x, y, z), \end{aligned} \quad (4.22)$$

where the scattered pulse from the present time step N are as denoted as $N V_{\alpha j}^r$ and the pulses incident on a port in the next time step $N+1$ are denoted as $N_{+1} V_{\alpha j}^i$. In the stub loaded SCN configurations additional connect equations for inductive and capacitive stubs are computed as follows

$$\begin{aligned} N_{+1}V_{ox}^i(x, y, z) &= N V_{ox}^r(x, y, z), \\ N_{+1}V_{oy}^i(x, y, z) &= N V_{oy}^r(x, y, z), \\ N_{+1}V_{oz}^i(x, y, z) &= N V_{oz}^r(x, y, z), \\ N_{+1}V_{sx}^i(x, y, z) &= - N V_{sx}^r(x, y, z), \end{aligned}$$

$$\begin{aligned}
{}_{N+1}V_{sy}^i(x, y, z) &= - {}_N V_{sy}^r(x, y, z), \\
{}_{N+1}V_{sz}^i(x, y, z) &= - {}_N V_{sz}^r(x, y, z).
\end{aligned}
\tag{4.23}$$

4.3 The Mapped SCN-PML

In the previous section the general constitutive relation of the SCN was presented which led to the description of two commonly used SCN configurations. The remainder of this section shall derive a new configuration of the SCN which implements the theory of the stretched coordinate PML. This novel SCN-PML formulation, referred to as mapped SCN-PML, is an extension of the mapped approach described in Chapter 3 for the 2D TLM node.

As demonstrated in Chapter 3, the mapped approach implements the stretched coordinate PML theory as a transformation of the transmission line parameters. As illustrated in Fig. 4.2, the mapping process can be physically interpreted as stretching the basic TLM node about a point **O** (the node centre) from real to complex domain. This results in complex line admittances/impedances, complex propagation delay, and subsequently modified scatter-connect equations. It is important to note that the behavior at the node centre is unmodified in this scheme which thus ensures the characteristics of the basic TLM node is retained.

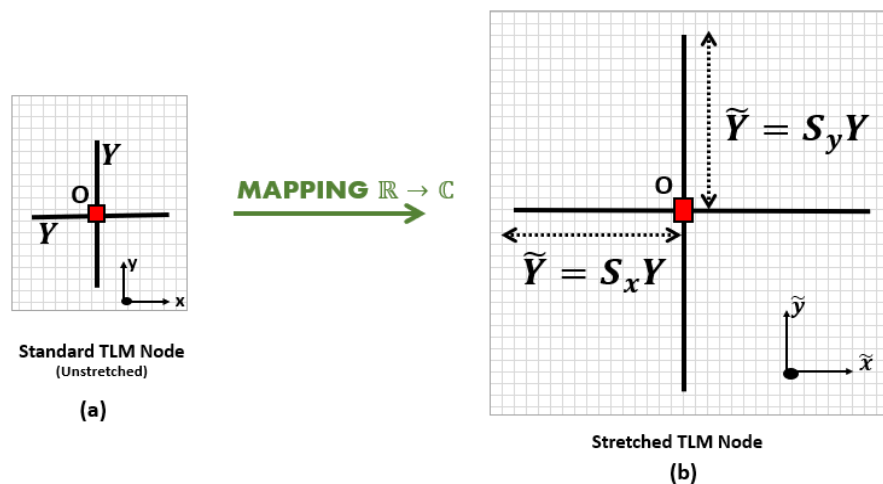


Figure 4.2. Diagram illustrating the process of mapping of the (a) standard 2D TLM node to the (b) Stretched 2D TLM node.

In order to formulate the mapped SCN-PML a general constitutive relation in the stretched coordinate domain must be established. This process relies on deriving a suitable medium-circuit equivalence as similarly shown in equations (4.1) and (4.2).

Consequently, consider the y -projections of Faraday's and Ampere's laws defined in (2.2), (2.3) which when given in a coordinate stretched space are expressed as

$$\frac{1}{S_z} \frac{\partial E_x}{\partial z} - \frac{1}{S_x} \frac{\partial E_z}{\partial x} = -\mu_y \frac{\partial H_y}{\partial t} - \sigma_{my} H_y, \quad (4.26)$$

$$\frac{1}{S_z} \frac{\partial H_x}{\partial z} - \frac{1}{S_x} \frac{\partial H_z}{\partial x} = \epsilon_y \frac{\partial E_y}{\partial t} + \sigma_{ey} E_y, \quad (4.27)$$

where S_x , S_y and S_z are coordinate stretch factors in x -, y - and z - directions which are compactly expressed as

$$S_i = 1 + \frac{\sigma_{si}}{j\omega}, \quad \sigma_{si}(i) = \frac{\sigma_i}{\epsilon_0} \geq 0, i = x, y, z, \quad (4.28)$$

where σ_i represents the conductivity profile along the i -coordinate axis that controls the rate of decay. The coordinate stretch factors employed in (4.26) and (4.27) theoretically support the desired reflection-free attenuation of propagating waves and are defined according to stretched coordinate PML [4.14].

In its present form equations (4.26) and (4.27) represent a modification of Maxwell's equation therefore the field solutions in the PML medium will not satisfy Maxwell's equations (i.e. non-Maxwellian fields arise), also no physical insight on the transformation of the PML medium parameters is revealed by both equations. In pursuit of a mapped SCN-PML formulation a suitable medium-circuit must be obtained therefore a re-expression of (4.26) and (4.27) must be sought.

By multiplying both sides of (4.26) and (4.27) with $S_z S_x$ the following equations are obtained,

$$\frac{\partial S_x E_x}{\partial z} - \frac{\partial S_z E_z}{\partial x} = -\frac{S_z S_x}{S_y} \mu_y \frac{\partial S_y H_y}{\partial t} - \frac{S_z S_x}{S_y} \sigma_{my} H_y S_y, \quad (4.29)$$

$$\frac{\partial S_x H_x}{\partial z} - \frac{\partial S_z H_z}{\partial x} = \frac{S_z S_x}{S_y} \epsilon_y \frac{\partial S_y E_y}{\partial t} + \frac{S_z S_x}{S_y} \sigma_{ey} E_y S_y, \quad (4.30)$$

both of which are a re-expression of (4.26) and (4.27) and represent Maxwell's equations but in a material space with complex anisotropic electric and magnetic properties. More importantly, this present form generates Maxwellian field solutions although with the following scaling applied on the fields,

$$E_i \rightarrow S_i E_i, \quad H_i \rightarrow S_i H_i.$$

In addition, the form adopted highlights the transformation of the medium parameters which are given as

$$\begin{aligned} \tilde{\mu}_y &= \frac{S_z S_x}{S_y} \mu_y, & \tilde{\epsilon}_y &= \frac{S_z S_x}{S_y} \epsilon_y, \\ \tilde{\sigma}_{my} &= \frac{S_z S_x}{S_y} \sigma_{my}, & \tilde{\sigma}_{ey} &= \frac{S_z S_x}{S_y} \sigma_{ey}, \end{aligned} \quad (4.31)$$

where the $\tilde{}$ is used to indicate parameters in the complex stretched space. The above transformation of the medium parameters reveals the geometry and material inter-relationship of Maxwell's equations which enables the form invariance property [4.15] where the solutions in a stretched coordinate space with free space material parameters are the same as solutions in an unstretched space but with more complex anisotropic material parameters. This interpretation is crucial to the TLM-PML development made here since according to the underlying TLM medium-circuit equivalence, the coordinate stretching is thus applied directly to the numerical algorithm. Therefore, by a mapping of the TLM circuit parameters, the TLM solution to Maxwell's equations is obtained but with the desired absorption behavior applied.

According to the TLM medium-to-circuit equivalence previously described in (4.1) and (4.2) the SCN circuit parameters in the stretched space are now given as

$$\begin{aligned}
 \tilde{L}_y^t &= \tilde{\mu}_y \Delta l = \frac{S_z S_x}{S_y} \mu_y \Delta l, \\
 \tilde{C}_y^t &= \tilde{\epsilon}_y \Delta l = \frac{S_z S_x}{S_y} \epsilon_y \Delta l, \\
 \tilde{R}_y &= \tilde{\sigma}_{my} \Delta l = \frac{S_z S_x}{S_y} \sigma_{my} \Delta l, \\
 \tilde{G}_y &= \tilde{\sigma}_{ey} \Delta l = \frac{S_z S_x}{S_y} \sigma_{ey} \Delta l,
 \end{aligned} \tag{4.32}$$

with

$$\Delta l = \frac{\Delta_z \Delta_x}{\Delta_y},$$

where \tilde{L}_y^t and \tilde{C}_y^t represent the mapped total inductance and capacitance along the y -direction, respectively, and \tilde{R}_y and \tilde{G}_y represent the mapped resistance and conductance along the y -directions, respectively.

By applying a similar process as described above to the x and z projections of Faraday's and Ampere's laws a general medium-circuit equivalence can be defined for the mapped SCN-PML which is expressed in compact notation as

$$\begin{aligned}
 \tilde{C}_i^t &= \frac{S_j S_k}{S_i} \epsilon_i \Delta l^i, & \tilde{L}_i^t &= \frac{S_j S_k}{S_i} \mu_i \Delta l^i, \\
 \tilde{G}_i &= \frac{S_j S_k}{S_i} \sigma_{ei} \Delta l^i, & \tilde{R}_i &= \frac{S_j S_k}{S_i} \sigma_{mi} \Delta l^i,
 \end{aligned} \tag{4.33}$$

with

$$\Delta l^i = \frac{\Delta_j \Delta_k}{\Delta_i},$$

Following the derivation of (4.33) the general constitutive relations in the mapped SCN-PML are therefore established as

$$\begin{aligned}\tilde{L}_j^t &= \tilde{L}_{ik}\Delta i + \tilde{L}_{ki}\Delta k + \tilde{L}_j^s, \\ \tilde{C}_j^t &= \tilde{C}_{ij}\Delta i + \tilde{C}_{kj}\Delta k + \tilde{C}_j^o,\end{aligned}\quad (4.34)$$

where each distributed inductance and capacitance in (4.34) undergoes a similar stretching as the corresponding L_j^t and C_j^t (4.33) to yield the following relations

$$\begin{aligned}\tilde{L}_{ik} &= \frac{S_i S_k}{S_j} L_{ik}, & \tilde{L}_j^s &= \frac{S_i S_k}{S_j} L_j^s, \\ \tilde{C}_{ij} &= \frac{S_i S_k}{S_j} C_{ij}, & \tilde{C}_j^o &= \frac{S_i S_k}{S_j} C_j^o.\end{aligned}\quad (4.35)$$

Following from (4.35), the propagation delay Δt_i are transformed to a complex variable $\tilde{\Delta t}_i$ according to the following rule

$$\begin{aligned}\tilde{\Delta t}_i &= \Delta i \sqrt{\tilde{L}_{ij} \tilde{C}_{ij}} = \Delta i \sqrt{\frac{S_i S_j}{S_k} L_{ij} \frac{S_i S_k}{S_j} C_{ij}} = S_i \Delta t_i, \\ &= \Delta t_i + j \left(\frac{\Delta t_i \sigma_{si}}{j\omega} \right),\end{aligned}\quad (4.36)$$

and the characteristic impedance (admittance) of the i -directed and j -polarized TLs in the mapped SCN-PML is given as

$$\tilde{Z}_{ij} = \sqrt{\frac{\frac{S_i S_j}{S_k} L_{ij}}{\frac{S_i S_k}{S_j} C_{ij}}} = \frac{S_j}{S_k} Z_{ij} = \frac{1}{\tilde{Y}_{ij}}.\quad (4.37)$$

The characteristic impedance/admittance of the stub lines experience a similar stretching to the corresponding L_j^s and C_j^o (4.35) parameters. Therefore, the transformed impedance of the short-circuit stub is given as

$$\tilde{Z}_{sj} = Z_{sj} \frac{S_i S_k}{S_j}, \quad (4.38)$$

and the transformed admittance open-circuit stub is given as

$$\tilde{Y}_{oj} = Y_{oj} \frac{S_i S_k}{S_j}. \quad (4.39)$$

The constituent 2D nodes which make up the mapped SCN-PML can be straightforwardly derived by applying the transformed admittance/impedance parameters derived in (4.37) to the shunt and series nodes shown in Chapter 3. This results in a total of six mapped shunt node and mapped series node defined within the topology of the mapped SCN. The Thèvenin circuits of both nodes is illustrated in Fig. 4.3 and 4.4.

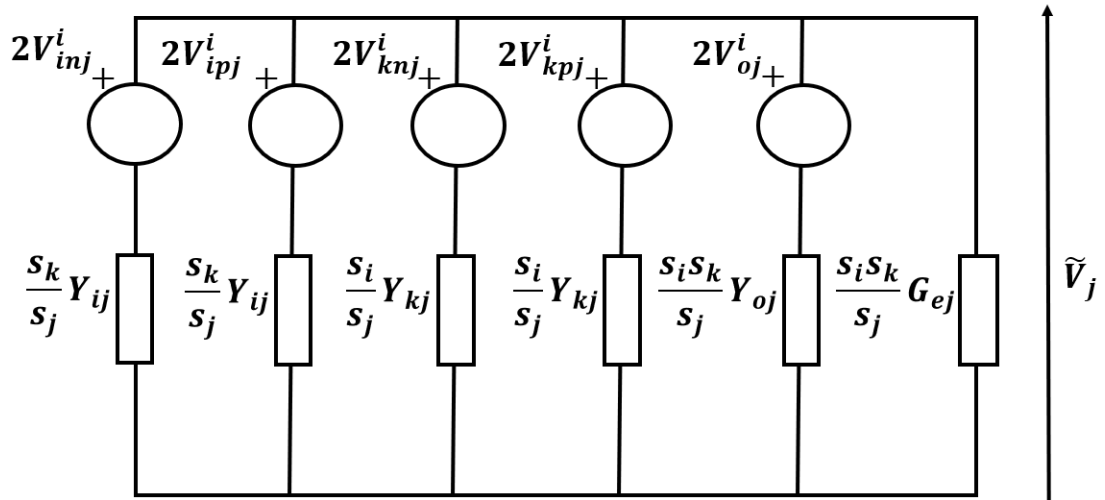


Figure 4.3. Thevenin equivalent circuit of the mapped shunt node PML.

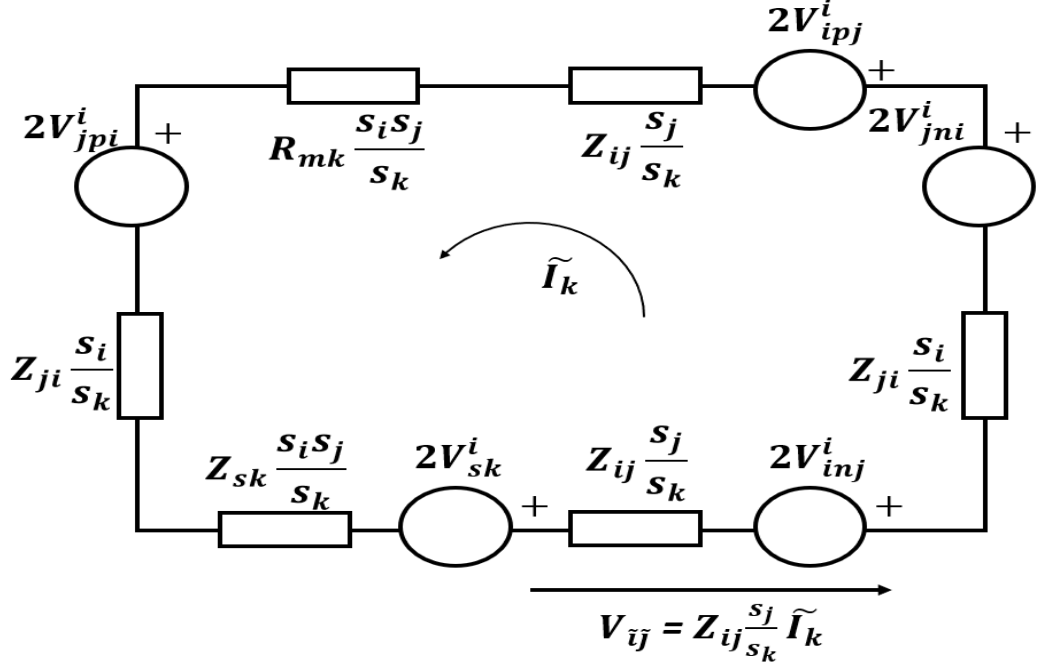


Figure 4.4. Thevenin equivalent circuit of the mapped series node PML.

4.3.1 Modified Scatter Algorithms

Like the standard (unstretched) SCN an equivalent network model approach is employed to derive the scatter equations of the mapped SCN-PML [4.12], [4.13]. The scattering procedure in the mapped SCN-PML can thus be written compactly as

$$\begin{aligned}
V_{inj}^r &= \tilde{V}_j \pm \tilde{I}_k \tilde{Z}_{ij} - V_{ipj}^i, \\
V_{ipj}^r &= \tilde{V}_j \mp \tilde{I}_k \tilde{Z}_{ij} - V_{inj}^i, \\
V_{oj}^r &= \tilde{V}_j - V_{oj}^i, \\
V_{sj}^r &= \tilde{I}_j \tilde{Z}_{sj} - V_{sj}^i,
\end{aligned} \tag{4.40}$$

where the upper and lower signs are similarly applied according to the indices rule shown in (4.25).

An expression for the equivalent voltage in the j -direction \tilde{V}_j can be easily obtained by applying circuit theory to the mapped shunt circuit (Fig.4.3) to give

$$\tilde{V}_j = 2 \frac{S_k Y_{ij} (V_{inj}^i + V_{ipj}^i) + S_i Y_{kj} (V_{kpj}^i + V_{knj}^i) + S_i S_k Y_{oj} V_{oj}^i}{2S_k Y_{ij} + 2S_i Y_{kj} + S_i S_k (G_{ej} + Y_{oj})}. \quad (4.41)$$

Similarly, an expression for the equivalent current in the k direction \tilde{I}_k is obtained from Fig.4.4 as

$$\tilde{I}_k = 2 \frac{(V_{inj}^i - V_{ipj}^i) + (V_{jpi}^i - V_{jni}^i) - V_{sk}^i}{\frac{S_j}{S_k} Z_{ij} + \frac{S_i}{S_k} Z_{ji} + \frac{S_i S_j}{S_k} (Z_{sk} + R_{mk})}. \quad (4.42)$$

As a result of the PML transformation factor $S_j = 1 + j \frac{\sigma_j}{\epsilon_0 \omega}$ the mapped SCN parameters presented thus far are defined as complex frequency parameters. As similarly described in Chapter 3, for an appropriate time domain TLM computation a bilinear transformation [4.16] must therefore be applied which enables a mapping of the complex frequency voltages/currents shown in (4.41) and (4.42) to discrete time domain representations. This transformation is particularly required to compute the full scatter equations.

According to the compact notation in (4.40) the full scatter equations for each link line in the SCN is obtained by computing the time domain representations of \tilde{V}_j and $\tilde{Z}_{ij} \tilde{I}_k$ and making appropriate substitutions in line with the indices rule (4.25).

Sections 4.3.2 and 4.3.3 below shall therefore focus on deriving the full scatter equations for the 12-port and 15-port Mapped SCN-PML. The approach taken is general and can be straightforwardly applied to the general case of the 18-port stub loaded SCN node and other hybrid SCN nodes.

4.3.2 Full Scatter Equations: 12-port Mapped SCN-PML

To permit a simpler presentation, and since the majority of the applications in which the PML is typically applied involve terminating materially homogeneous cubic

meshes i.e. $\Delta x = \Delta y = \Delta z$, the full scatter algorithm is first derived for the basic 12-port mapped SCN where $Z_{sj} = Y_{oj} = R_{mj} = G_{ej} = 0$, and $Z_{ij} = Z_0$.

Substituting the complex stretch factors $S_i = 1 + \frac{\sigma_{si}}{j\omega}$, $S_k = 1 + \frac{\sigma_{sk}}{j\omega}$ into (4.41) and setting $Y_{oj} = G_{ej} = 0$, and $Y_{ij} = Y_0$ obtains

$$\tilde{V}_j(j\omega) = \frac{(j\omega + \sigma_{sk})(V_{inj}^i + V_{ipj}^i) + (j\omega + \sigma_{si})(V_{kpj}^i + V_{knj}^i)}{2j\omega + \sigma_{sk} + \sigma_{si}}, \quad (4.43)$$

which upon applying the transformation $s \rightarrow j\omega$ and the bilinear transformation $s \rightarrow \frac{2}{\Delta t} \frac{1-z^{-1}}{1+z^{-1}}$ gives

$$\tilde{V}_j[z] = \alpha_j \left(\begin{array}{c} \frac{1}{2}(V_{inj}^i + V_{ipj}^i + V_{knj}^i + V_{kpj}^i) - \\ \frac{1}{2}(V_{inj}^i + V_{ipj}^i + V_{knj}^i + V_{kpj}^i)z^{-1} + \\ \frac{\sigma_{sk}\Delta t}{4} \left((V_{inj}^i + V_{ipj}^i) + (V_{inj}^i + V_{ipj}^i)z^{-1} \right) + \\ \frac{\sigma_{si}\Delta t}{4} \left((V_{knj}^i + V_{kpj}^i) + (V_{knj}^i + V_{kpj}^i)z^{-1} \right) + \\ \left(1 - \frac{(\sigma_{si} + \sigma_{sk})\Delta t}{4} \right) \tilde{V}_j z^{-1} \end{array} \right), \quad (4.44)$$

where α_j is given by

$$\alpha_j = \frac{4}{4 + (\sigma_{si} + \sigma_{sk})\Delta t}. \quad (4.45)$$

To obtain a discrete time domain representation of $\tilde{V}_j[z]$ an inverse Z-transform is performed on (4.44), where z^{-1} indicates use of samples in the previous time step $(N - 1)\Delta t$ and $N\Delta t$ denotes the current time step. This yields a compact formulation

$${}_N\tilde{V}_j = \alpha_j {}_N V_j + {}_N V_j^{PMLshunt}, \quad (4.46)$$

where ${}_N V_j$ represents the total voltage in the standard shunt circuit given as [4.7]

$${}_N V_j = \frac{{}_N V_{inj}^i + {}_N V_{ipj}^i + {}_N V_{knj}^i + {}_N V_{kpj}^i}{2}, \quad (4.47)$$

and ${}_N V_j^{PMLshunt}$ represents the PML voltages attributed to ${}_N \tilde{V}_j$ and is given as

$${}_N V_j^{PMLshunt} = \alpha_j \begin{pmatrix} -\frac{1}{2} {}_{N-1} (V_{inj}^i + V_{ipj}^i + V_{knj}^i + V_{kpj}^i) + \\ \frac{\sigma_{sk} \Delta t}{4} ({}_N (V_{inj}^i + V_{ipj}^i) + {}_{N-1} (V_{inj}^i + V_{ipj}^i)) + \\ \frac{\sigma_{si} \Delta t}{4} ({}_N (V_{knj}^i + V_{kpj}^i) + {}_{N-1} (V_{knj}^i + V_{kpj}^i)) + \\ \left(1 - \frac{(\sigma_{si} + \sigma_{sk}) \Delta t}{4}\right) {}_{N-1} \tilde{V}_j \end{pmatrix}. \quad (4.48)$$

Substituting the complex stretch factors $S_i = 1 + \frac{\sigma_{si}}{j\omega}$, $S_j = 1 + \frac{\sigma_{sj}}{j\omega}$ and $S_k = 1 + \frac{\sigma_{sk}}{j\omega}$ into (4.42) and setting $Z_{sk} = R_{mk} = 0$, and $Z_{ji} = Z_{ij} = Z_0$ obtains

$$\tilde{I}_k = 2(j\omega + \sigma_{sk}) \frac{(V_{inj}^i - V_{ipj}^i) + (V_{jpi}^i - V_{jni}^i)}{Z_0 (2j\omega + \sigma_{si} + \sigma_{sj})}. \quad (4.49)$$

Similarly, the discrete time form of the current \tilde{I}_k is obtained by applying the bilinear transformation to (4.49) to yield

$${}_N \tilde{I}_k = \alpha_k \begin{pmatrix} \left({}_N I_k - {}_{N-1} I_k + \frac{\sigma_{sk} \Delta t}{2} ({}_N I_k + {}_{N-1} I_k) \right) + \\ \left(1 - \frac{(\sigma_{si} + \sigma_{sj}) \Delta t}{4}\right) {}_{N-1} \tilde{I}_k \end{pmatrix}, \quad (4.50)$$

where ${}_N I_k$ represents the total k -directed current in the standard series circuit [4.7] given as

$${}_N I_k = \frac{({}_N V_{inj}^i - {}_N V_{ipj}^i) + ({}_N V_{kpj}^i - {}_N V_{knj}^i)}{2Z_0}. \quad (4.51)$$

The total voltage \tilde{V}_{ij} across the i -directed and j -polarized transmission line in the k -directed mapped series circuit (see Fig. 4.4) is given as

$$\tilde{V}_{ij} = \tilde{I}_k \tilde{Z}_{ij} = \tilde{I}_k Z_{ij} \frac{S_j}{S_k}. \quad (4.52)$$

By applying the bilinear transformation to (4.52) a compact formulation for $\tilde{I}_k \tilde{Z}_{ij} \equiv {}_N\tilde{V}_{ij}$ is obtained as

$$\tilde{I}_k \tilde{Z}_{ij} = {}_N\tilde{V}_{ij} = \alpha_k {}_N I_k Z_0 + {}_N V_{ij}^{PML_{series}}, \quad (4.53)$$

where ${}_N V_{ij}^{PML_{series}}$ represents the PML voltages in the mapped series circuit given as

$$\begin{aligned} & {}_N V_{ij}^{PML_{series}} \\ &= \alpha_k \left(Z_0 \left(-{}_{N-1} I_k + \frac{\sigma_{sk} \Delta t}{2} ({}_N I_k + {}_{N-1} I_k) \right) + \right. \\ & \quad \left. \left(1 - \frac{(\sigma_{si} + \sigma_{sj}) \Delta t}{4} \right) {}_{N-1} \tilde{V}_{ij} \right). \end{aligned} \quad (4.54)$$

Therefore, by substituting (4.46) and (4.53) into (4.40) the discrete time domain expression describing the scatter in the 12-port mapped SCN-PML is obtained. For example, the reflected voltage on the xnz transmission line is given as

$${}_N V_{xnz}^r = \alpha_z {}_N V_z - \alpha_y {}_N I_y Z_0 + {}_N V_{xnz}^{PML} - {}_N V_{xpz}^i, \quad (4.55)$$

where

$${}_N V_{xnz}^{PML} = {}_N V_z^{PML_{shunt}} - {}_N V_{xz}^{PML_{series}}, \quad (4.56)$$

Following the above derivation, the complete scatter equations for the 12-port mapped SCN are given below

$$\begin{aligned}
 V_{ynx}^r &= \alpha_x V_x - \alpha_z I_z Z_0 - V_{ypx}^i + V_{ynx}^{PML}, \\
 V_{znx}^r &= \alpha_x V_x + \alpha_y I_y Z_0 - V_{zpx}^i + V_{znx}^{PML}, \\
 V_{xny}^r &= \alpha_y V_y + \alpha_z I_z Z_0 - V_{xpy}^i + V_{xny}^{PML}, \\
 V_{zny}^r &= \alpha_y V_y - \alpha_x I_x Z_0 - V_{zpy}^i + V_{zny}^{PML}, \\
 V_{ynz}^r &= \alpha_z V_z + \alpha_x I_x Z_0 - V_{ypz}^i + V_{ynz}^{PML}, \\
 V_{xnz}^r &= \alpha_z V_z - \alpha_y I_y Z_0 - V_{xpz}^i + V_{xnz}^{PML}, \\
 V_{ypz}^r &= \alpha_z V_z - \alpha_x I_x Z_0 - V_{ynz}^i + V_{ypz}^{PML}, \\
 V_{zpy}^r &= \alpha_y V_y + \alpha_x I_x Z_0 - V_{zny}^i + V_{zpy}^{PML}, \\
 V_{zpx}^r &= \alpha_x V_x - \alpha_y I_y Z_0 - V_{znx}^i + V_{zpx}^{PML}, \\
 V_{xpz}^r &= \alpha_z V_z + \alpha_y I_y Z_0 - V_{xnz}^i + V_{xpz}^{PML}, \\
 V_{xpy}^r &= \alpha_y V_y - \alpha_z I_z Z_0 - V_{xny}^i + V_{xpy}^{PML}, \\
 V_{ypx}^r &= \alpha_x V_x + \alpha_z I_z Z_0 - V_{ypx}^i + V_{ypx}^{PML},
 \end{aligned} \tag{4.57}$$

with

$$\begin{aligned}
 \alpha_x &= \frac{4}{4 + (\sigma_{sz} + \sigma_{sy})\Delta t}, & \alpha_y &= \frac{4}{4 + (\sigma_{sz} + \sigma_{sx})\Delta t}, \\
 \alpha_z &= \frac{4}{4 + (\sigma_{sx} + \sigma_{sy})\Delta t},
 \end{aligned}$$

where V_x, V_y and V_z denote the total x, y and z -directed voltages in the standard SCN node, respectively, and I_x, I_y and I_z denote the total currents flowing in the x, y and z -directions in the standard SCN node, respectively [4.7]. The voltages V_{iaj}^{PML} represent the PML voltages associated with the reflected pulses on each TL which are given as

$$\begin{aligned}
 V_{ynx,ypx}^{PML} &= V_x^{PML_shunt} \mp V_{yx}^{PML_series}, \\
 V_{znx,zpx}^{PML} &= V_x^{PML_shunt} \pm V_{zx}^{PML_series}, \\
 V_{xny,xpy}^{PML} &= V_y^{PML_shunt} \pm V_{xy}^{PML_series}, \\
 V_{zny,zpy}^{PML} &= V_y^{PML_shunt} \mp V_{zy}^{PML_series}, \\
 V_{ynz,ypz}^{PML} &= V_z^{PML_shunt} \pm V_{yz}^{PML_series}, \\
 V_{xnz,xpz}^{PML} &= V_z^{PML_shunt} \mp V_{xz}^{PML_series},
 \end{aligned} \tag{4.58}$$

where the upper sign, for example in component $V_{A,B}^{PML}$, is applied to A-directed line and the lower sign is applied to the B-directed line. Note that for the case where $\sigma_i = \sigma_j = \sigma_k = 0$ then $V_j^{PML_shunt} = V_{ij}^{PML_series} = V_{i\alpha_j}^{PML} = 0$ and $\alpha_i = \alpha_j = \alpha_k = 1$ and the above becomes the standard SCN TLM scatter equations [4.7] for a simple medium.

4.3.3 Full Scatter Equations: 15-port Mapped HSCN-PML

The previous section derived the complete scatter equations required for implementing the 12-port mapped SCN-PML which is suitable for terminating lossless homogenous media. It is practically relevant to also develop the algorithms which enable a deployment of the PML in inhomogeneous anisotropic media. In such problems the PML layer must match the material property of the interfacing medium. As illustrated in Fig 4.5 this condition can be simulated by overlapping the material properties of the interfacing medium into the PML. Following a similar derivation to section 4.3.2 the algorithms suitable for such applications are presented in this section which are developed based on the mapping principles but are applied to the HSCN [4.9], [4.10].

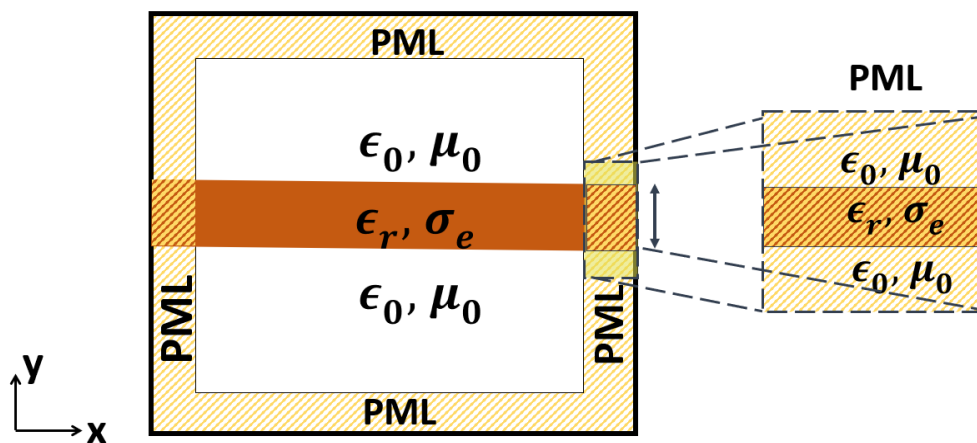


Figure 4.5. Diagram illustrating a infinitely extended lossy dielectric slab situated in a computational domain terminated by PML medium. The infinite extent of the slab is represented by overlapping the material properties of the interfacing medium into the PML.

The choice of usage of HSCN is made due to computational efficiency attainable which arises since less stubs are used and the overall number of PML auxiliary variables are thus reduced. Furthermore, compared to the Super Symmetrical Condensed Node (SSCN), which completely alleviates the use of stubs, a better dispersion characteristic is reported by the HSCN [4.17]-[4.18].

The complete scatter equations for the mapped HSCN-PML can be expressed by computing the time domain representations of \tilde{V}_j and $\tilde{Z}_{ij}\tilde{I}_k$ and making appropriate substitutions in line with the indices rule (4.25). However unlike the development shown in the previous section the capacitive stubs Y_{oj} and lossy elements G_{ej} and R_{mk} are set to non-zero values in this case and the inductive stub Z_{sk} is set to zero.

To distinguish between the expressions of the 12-port SCN and HSCN the superscript "HSCN" is employed in equations that follow.

Note that \tilde{V}_j^{HSCN} is equal to the total voltage expression \tilde{V}_j given in (4.41) which is a compact representation of the total z -directed voltage expression \tilde{V}_z solved in section 3.3.1 of chapter 3. Therefore, to avoid repetition the derivation of \tilde{V}_j^{HSCN} is avoided but rather the compact solution is presented

$${}_N\tilde{V}_j^{HSCN} = \alpha_j^{HSCN} {}_N V_j^{HSCN} + V_j^{PMLshuntHSCN}, \quad (4.59)$$

where the full definitions of the PML related parameters i.e. α_j^{HSCN} and $V_j^{PMLshuntHSCN}$ are given in appendix 4A.

By substituting $V_{sk}^i = Z_{sk} = 0$ into (4.42) the following expression for ${}_N\tilde{V}_{ij}^{HSCN} \equiv \tilde{Z}_{ij}\tilde{I}_k^{HSCN}$ is obtained

$${}_N\tilde{V}_{ij}^{HSCN} \equiv \tilde{Z}_{ij}\tilde{I}_k^{HSCN} = 2Z_{ij}S_k \frac{(V_{inj}^i - V_{ipj}^i) + (V_{jpi}^i - V_{jni}^i)}{S_j Z_{ij} + S_i Z_{ji} + S_i S_j R_{mk}}, \quad (4.60)$$

and upon substituting the stretch factors into (4.60) and applying the bilinear transformation a time domain expression of ${}_N\tilde{V}_{ij}^{HSCN} \equiv \tilde{Z}_{ij}\tilde{I}_k^{HSCN}$ is obtained

$${}_N\tilde{V}_{ij}^{HSCN} \equiv \tilde{Z}_{ij}\tilde{I}_k^{HSCN} = \beta_k^{HSCN} {}_N I_k^{HSCN} Z_{ij} + V_{ij}^{PMLseriesHSCN}, \quad (4.61)$$

where the definitions of ${}_N I_k^{HSCN}$, β_k^{HSCN} and $V_{ij}^{PMLseriesHSCN}$ are given in the appendix 4B.

Therefore, by substituting (4.59) and (4.61) into (4.40) the discrete time domain expression describing the scatter in the mapped HSCN-PML is obtained. For example, the reflected voltage on the xnz transmission line is given as

$$V_{xnz}^r = \alpha_z^{HSCN} V_z^{HSCN} - \beta_y^{HSCN} I_y^{HSCN} Z_{xz} - V_{xpz}^i - V_{xnz}^{PMLHSCN}, \quad (4.62)$$

where $V_{xnz}^{PMLHSCN}$ represents the PML voltages associated with the reflected pulses given as

$$V_{xnz}^{PMLHSCN} = V_{ij}^{PMLseriesHSCN} - V_j^{PMLshuntHSCN}. \quad (4.63)$$

Following the above description, the complete scatter equations for the mapped HSCN are given below

$$\begin{aligned} V_{ynx}^r &= \alpha_x^{HSCN} V_x^{HSCN} - \beta_z^{HSCN} I_z^{HSCN} Z_{yx} - V_{ypx}^i - V_{ynx}^{PMLHSCN}, \\ V_{znx}^r &= \alpha_x^{HSCN} V_x^{HSCN} + \beta_y^{HSCN} I_y^{HSCN} Z_{zx} - V_{zpx}^i - V_{znx}^{PMLHSCN}, \\ V_{xny}^r &= \alpha_y^{HSCN} V_y^{HSCN} + \beta_z^{HSCN} I_z^{HSCN} Z_{xy} - V_{ypx}^i + V_{xny}^{PMLHSCN}, \\ V_{zny}^r &= \alpha_y^{HSCN} V_y^{HSCN} - \beta_x^{HSCN} I_x^{HSCN} Z_{zy} - V_{zpy}^i - V_{zny}^{PMLHSCN}, \\ V_{ynz}^r &= \alpha_z^{HSCN} V_z^{HSCN} + \beta_x^{HSCN} I_x^{HSCN} Z_{yz} - V_{ypz}^i + V_{ynz}^{PMLHSCN}, \end{aligned}$$

$$\begin{aligned}
 V_{xnz}^r &= \alpha_z^{HSCN} V_z^{HSCN} - \beta_y^{HSCN} I_y^{HSCN} Z_{xz} - V_{xpz}^i - V_{xnz}^{PMLHSCN}, \\
 V_{ypz}^r &= \alpha_z^{HSCN} V_z^{HSCN} - \beta_x^{HSCN} I_x^{HSCN} Z_{yz} - V_{ynz}^i - V_{ypz}^{PMLHSCN}, \\
 V_{zpy}^r &= \alpha_y^{HSCN} V_y^{HSCN} + \beta_x^{HSCN} I_x^{HSCN} Z_{zy} - V_{zpy}^i + V_{zpy}^{PMLHSCN}, \\
 V_{zpx}^r &= \alpha_x^{HSCN} V_x^{HSCN} - \beta_y^{HSCN} I_y^{HSCN} Z_{zx} - V_{znx}^i - V_{zpx}^{PMLHSCN}, \\
 V_{xpz}^r &= \alpha_z^{HSCN} V_z^{HSCN} + \beta_y^{HSCN} I_y^{HSCN} Z_{xz} - V_{xnz}^i + V_{xpz}^{PMLHSCN}, \\
 V_{xpy}^r &= \alpha_y^{HSCN} V_y^{HSCN} - \beta_z^{HSCN} I_z^{HSCN} Z_{xy} - V_{xny}^i - V_{xpy}^{PMLHSCN}, \\
 V_{ypx}^r &= \alpha_x^{HSCN} V_x^{HSCN} + \beta_z^{HSCN} I_z^{HSCN} Z_{yx} - V_{ynx}^i + V_{ypx}^{PMLHSCN}, \\
 V_{ox}^r &= \alpha_x^{HSCN} V_x^{HSCN} + V_x^{PMLshuntHSCN} - V_{ox}^i, \\
 V_{oy}^r &= \alpha_y^{HSCN} V_y^{HSCN} + V_y^{PMLshuntHSCN} - V_{oy}^i, \\
 V_{oz}^r &= \alpha_z^{HSCN} V_z^{HSCN} + V_z^{PMLshuntHSCN} - V_{oz}^i,
 \end{aligned} \tag{4.64}$$

where the PML voltages associated with the reflected pulses on each link line are given as

$$\begin{aligned}
 V_{ynx,ypx}^{PMLHSCN} &= V_{yx}^{PMLseriesHSCN} \mp V_x^{PMLshuntHSCN}, \\
 V_{znx,zpx}^{PMLHSCN} &= V_{zx}^{PMLseriesHSCN} \pm V_x^{PMLshuntHSCN}, \\
 V_{xny,xpy}^{PMLHSCN} &= V_{xy}^{PMLseriesHSCN} \pm V_y^{PMLshuntHSCN}, \\
 V_{ynz,ypz}^{PMLHSCN} &= V_{yz}^{PMLseriesHSCN} \pm V_z^{PMLshuntHSCN}, \\
 V_{xnz,xpz}^{PMLHSCN} &= V_{xz}^{PMLseriesHSCN} \mp V_z^{PMLshuntHSCN}, \\
 V_{zny,zpy}^{PMLHSCN} &= V_{zy}^{PMLseriesHSCN} \mp V_y^{PMLshuntHSCN},
 \end{aligned} \tag{4.65}$$

where the upper sign, for example in component $V_{A,B}^{PMLHSCN}$, is applied to line A and the lower sign is applied to the line B.

4.3.4 Modified Connect Algorithms

According to equation (4.36), the process of mapping the TLM node transforms the time step Δt_i to a complex variable $\widetilde{\Delta t}_i = S_i \Delta t_i$. As shown the real part of the time step Δt_i is unchanged across each transmission line (*i. e.* $\Delta t = \Delta t_x = \Delta t_y = \Delta t_z$) therefore ensuring that pulse synchronism is maintained across the SCN network. However, as similarly described in Chapter 3, the imaginary component of $\widetilde{\Delta t}_i$ introduces an attenuation along each pulse propagating on the transmission line. The TLM connect process along each transmission line in the mapped SCN-PML is transformed from (4.22) to the following

$$\begin{aligned}
{}_{N+1}V_{ynx}^i(x, y + \Delta y, z) &= {}_N V_{ypx}^r(x, y, z) e^{-\sigma_{sy} \Delta t}, \\
{}_{N+1}V_{znx}^i(x, y, z + \Delta z) &= {}_N V_{zpx}^r(x, y, z) e^{-\sigma_{sz} \Delta t}, \\
{}_{N+1}V_{xny}^i(x + \Delta x, y, z) &= {}_N V_{xpy}^r(x, y, z) e^{-\sigma_{sx} \Delta t}, \\
{}_{N+1}V_{zny}^i(x, y, z + \Delta z) &= {}_N V_{zpy}^r(x, y, z) e^{-\sigma_{sz} \Delta t}, \\
{}_{N+1}V_{ynz}^i(x, y + \Delta y, z) &= {}_N V_{ypz}^r(x, y, z) e^{-\sigma_{sy} \Delta t}, \\
{}_{N+1}V_{xnz}^i(x + \Delta x, y, z) &= {}_N V_{xpz}^r(x, y, z) e^{-\sigma_{sx} \Delta t}, \\
{}_{N+1}V_{ypz}^i(x, y - \Delta y, z) &= {}_N V_{ynz}^r(x, y, z) e^{-\sigma_{sy} \Delta t}, \\
{}_{N+1}V_{zpy}^i(x, y, z - \Delta z) &= {}_N V_{zny}^r(x, y, z) e^{-\sigma_{sz} \Delta t}, \\
{}_{N+1}V_{zpx}^i(x, y, z - \Delta z) &= {}_N V_{znx}^r(x, y, z) e^{-\sigma_{sz} \Delta t}, \\
{}_{N+1}V_{xpz}^i(x - \Delta x, y, z) &= {}_N V_{xnz}^r(x, y, z) e^{-\sigma_{sx} \Delta t}, \\
{}_{N+1}V_{xpy}^i(x - \Delta x, y, z) &= {}_N V_{xny}^r(x, y, z) e^{-\sigma_{sx} \Delta t}, \\
{}_{N+1}V_{ypx}^i(x, y - \Delta y, z) &= {}_N V_{ypx}^r(x, y, z) e^{-\sigma_{sy} \Delta t}.
\end{aligned} \tag{4.66}$$

4.4 Summary

A PML implementation which maps the unconditionally stable symmetrical condensed node to a complex stretched domain was derived in this chapter. This method is based on the mapping approach introduced in Chapter 3 and thus implements the stretched coordinate PML theory by a transformation of the transmission line parameters. This approach to PML implementation was shown to result in a complex propagation delay and complex frequency dependent line

admittances/impedances. As such, both the standard scatter and connect equations are modified. The connect equations are shown to be modified by introducing an additional attenuation of propagation pulses. The modified scatter equations for the 12-port mapped SCN were derived since this represents the most common use case of the PMLs i.e. terminating homogenous media. Scatter equations for the mapped hybrid symmetrical condensed node were also derived which are suitable for terminating lossy inhomogeneous anisotropic media. A demonstration of the absorbing performance and stability of the mapped SCN-PML will follow in Chapters 5 and Chapter 6.

References

- [4.1] C. Eswarappa and W. J. R. Hofer, "Implementation of Berenger's ' absorbing boundary conditions in TLM by interfacing FDTD perfectly matched layers," *Electron. Lett.*, vol. 31, no. 15, pp. 1264–1266, July 1995.
- [4.2] N. Pena and M. M. Ney, "Absorbing-boundary conditions using perfectly matched layer (PML) technique for three-dimensional TLM simulations," *IEEE Trans. Microwave Theory Tech.*, vol. 45, pp. 1749–1755, Oct. 1997.
- [4.3] J. L. Dubard, and D. Pompei "Optimization of the PML efficiency in 3-D TLM method." *IEEE Transactions on Microwave Theory and Techniques*; 48(7):1081–1087, 2000.
- [4.4] L. Maguer, and M. M. Ney, "Extended PML-TLM node: an efficient approach for full waveanalysis of open structures." *Int. J. Numer. Model.*, vol. 14 , pp. 129–144, 2001.
- [4.5] T. W. Kang, C. Christopoulos, and J. Paul, "Implementation of the stretched coordinate-based PML for waveguide structures in TLM". *International journal of numerical modelling electronic networks. Devices and fields*. Vol. 18, pp. 107-118, 2005.
- [4.6] P. B. Johns, "A symmetrical condensed node for the TLM method," *IEEE Trans. Microwave Theory Tech.*, vol. MTT-35, no. 4, pp. 370-377, Apr. 1987.
- [4.7] C. Christopoulos, *The Transmission-Line Modeling Method: TLM*. IEE Press: Piscataway, NJ, 1995.

- [4.8] V. Trenkic, C. Christopoulos, and T. M. Benson, "Development of a general symmetrical condensed node for the TLM method," *IEEE Trans. Microwave Theory Tech.*, vol. 44, pp. 2129–2135, Dec. 1996.
- [4.9] R. A. Scaramuzza and A. J. Lowery, "Hybrid symmetrical condensed node for TLM method", *Electronics Letters*, vol. 26, no.23, pp. 1947{1949, Nov. 1990.
- [4.10] P. Berrini and K. Wu, "A pair of hybrid symmetrical condensed TLM nodes", *IEEE Microwave and Guided Wave Letters*, vol. 4, no. 7, pp. 244{246, July 1994.
- [4.11] V. Trenkic, C. Christopoulos and T. M. Benson, "On the time step in hybrid symmetrical condensed TLM nodes," in *IEEE Transactions on Microwave Theory and Techniques*, vol. 43, no. 9, pp. 2172-2174, Sept. 1995,
- [4.12] P. Naylor and R. Ait-Sadi, "Simple method for determining 3-D TLM nodal scattering in nonscalar problems." *Electron. Lett.*, vol. 28, no. 25, pp. 2353-2354, Dec. 1992.
- [4.13] V. Trenkic, C. Christopoulos, and T. M. Benson, "Simple and elegant formulation of scattering in TLM nodes," *Electron. Lett.*, vol. 29, no. 18, pp. 1651-1652, Sept. 1993.
- [4.14] W. C. Chew and W. H. Weedon, "A 3D perfectly matched medium from modified Maxwell's equations with stretched coordinates," *Microwave and Optical Tech. Lett.*, vol. 7, no. 13, pp. 599–604, 1994.
- [4.15] J. Ward and J. B. Pendry, "Refraction and geometry in Maxwell's equations," *J. Modern Optics*, vol. 43, no. 4, pp. 773–793, 1996.
- [4.16] J. Paul, C. Christopoulos, D.W.P. Thomas: "Generalized material models in TLM – Part 1: Materials with frequency dependent properties, *IEEE Trans. Ant. Prop.*, 50(7),pp. 997-1004, 1999.
- [4.17] V. Trenkic, C. Christopoulos and T. M. Benson, "New symmetrical super-condensed node for the TLM method," in *Electronics Letters*, vol. 30, no. 4, pp. 329-330, 17 Feb. 1994
- [4.18] M. Krumpholz, L. Roselli and P. Russer, "Dispersion characteristics of the TLM scheme with symmetrical super-condensed node," *Proceedings of 1995 IEEE MTT-S International Microwave Symposium, Orlando, FL, USA*, pp. 369-372 vol.2, 1995.

Appendix 4A – Definition of the total voltage ${}_N\tilde{V}_j^{HSCN}$ in the mapped HSCN-PML

The total voltage in the mapped HSCN-PML is compactly expressed as

$${}_N\tilde{V}_j^{HSCN} = \alpha_j^{HSCN} {}_N V_j^{HSCN} + V_j^{PMLshuntHSCN},$$

where α_j^{HSCN} and $V_j^{PMLshuntHSCN}$ are given as

$$\alpha_j^{HSCN} = \frac{Y_j}{2Y_j + y_{ij}\sigma_{sk}\Delta t + y_{kj}\sigma_{si}\Delta t + G_j(\sigma_{si} + \sigma_{sk})\Delta t + G_j b_j},$$

$$V_j^{PMLshuntHSCN} = \frac{\alpha_j^{HSCN}}{Y_j} \left(\begin{array}{l} Y_j (-2 {}_{N-1}V_j^{HSCN} + {}_{N-2}V_j^{HSCN}) + \\ \frac{y_{ij}\sigma_{sk}\Delta t}{2} ((V_{inj}^i + V_{ipj}^i) - {}_{k-2}(V_{inj}^i + V_{ipj}^i)) + \\ \frac{y_{kj}\sigma_{si}\Delta t}{2} ((V_{knj}^i + V_{kpj}^i) - {}_{k-2}(V_{knj}^i + V_{kpj}^i)) + \\ y_{oj}(a_j V_{oj}^i + b_j {}_{k-1}V_{oj}^i + c_j {}_{k-2}V_{oj}^i) + \\ d_j {}_{k-1}V_j^{HSCN} - e_j {}_{k-2}V_j^{HSCN} \end{array} \right),$$

With

$$Y_j = y_{ij} + y_{kj} + G_j, \quad G_j = \frac{Z_0 G_{ej} + y_{oj}}{2},$$

$$V_j^{HSCN} = \frac{((V_{inj}^i + V_{ipj}^i)y_{ij} + (V_{knj}^i + V_{kpj}^i)y_{kj} + V_{oj}^i y_{oj})}{Y_j},$$

$$b_j = \frac{\sigma_{si}\sigma_{sk}\Delta t^2}{2},$$

$$a_j = \frac{(\sigma_{sk} + \sigma_{si})\Delta t + b_j}{2},$$

$$c_j = - \frac{(\sigma_{sk} + \sigma_{si})\Delta t - b_j}{2},$$

$$d_j = 2Y_j - G_j b_j,$$

$$e_j = \frac{2Y_j - y_{ij}\sigma_{sk}\Delta t - y_{kj}\sigma_{si}\Delta t - G_j(\sigma_{si} + \sigma_{sk})\Delta t + G_j b_j}{2}.$$

Appendix 4B – Definition of the voltage ${}_N\tilde{V}_{ij}^{HSCN} \equiv \tilde{Z}_{ij}\tilde{I}_k^{HSCN}$ in the mapped HSCN-PML

$${}_N\tilde{V}_{ij}^{HSCN} \equiv \tilde{Z}_{ij}\tilde{I}_k^{HSCN} = \beta_k^{HSCN} {}_N I_k^{HSCN} Z_{ij} + V_{ij}^{PMLseriesHSCN},$$

where

$$V_{ij}^{PMLseriesHSCN} = \beta_k^{HSCN} \left(Z_{ij} \left(-2 {}_{N-1} I_k^{HSCN} + {}_{N-2} I_k^{HSCN} + \frac{\sigma_{sk}\Delta t}{2} (I_k^{HSCN} - {}_{N-2} I_k^{HSCN}) \right) - g_{ij\ k-1} \tilde{V}_{ij}^{HSCN} - h_{ij\ k-2} {}_N \tilde{V}_{ij}^{HSCN} \right),$$

with

$$I_k^{HSCN} = (V_{inj}^i - V_{ipj}^i) + (V_{jpi}^i - V_{jni}^i),$$

$$\beta_k^{HSCN} = \frac{2}{a_{ij} + b_{ij} + 2c_{ij}},$$

$$a_{ij} = 4Z_{ij} + R_{mk},$$

$$b_{ij} = \frac{\sigma_{si}\sigma_{sj}\Delta t^2 R_{mk}}{4Z_{ij}},$$

$$c_{ij} = \frac{(2Z_{ij} + R_{mk})(\sigma_{si} + \sigma_{sj})\Delta t}{4},$$

$$g_{ij} = b_{ij} - a_{ij},$$

$$h_{ij} = a_{ij} + b_{ij} - 2c_{ij}.$$

Chapter 5

Performance

Characterization of the

Mapped SCN-PML

In this chapter the performance of the mapped SCN-PML developed in Chapter 4 is characterized using the canonical 3D rectangular metal waveguide test case. The numerical reflections generated by the PML are examined for the cases of normal and oblique wave incidence and for different variations of the PML control parameters (i.e. conductivity profile, number of PML layers and reflection factor). The reflection performance and temporal stability of the mapped SCN-PML formulation is demonstrated by comparing against previously published SCN-PML schemes and the TLM matched boundary condition.

5.1 Performance Of The Mapped SCN-PML For Normally Incident Waves

The chapter begins with a systematic characterization of the mapped SCN-PML which is carried out for the case of plane waves impinged normally on the PML medium. This test case is important because it offers an isolated study of the continuous PML's perfect impedance matching condition upon the TLM space-time discretization [5.1]. In this application, the simple TLM matched boundary, achieves a perfect attenuation (i.e. reflection less) with no added increase in computational

expense; as such, this will serve as a benchmark upon which the efficiency of the SCN-PML implementations in [5.2] and [5.3] and the mapped SCN-PML are evaluated.

The tests carried out involved a wave guiding structure filled with air and truncated along the z -axis by either a PML medium or a matched boundary. This is as illustrated in Fig. 5.1 where the x , y and z dimensions are arbitrarily chosen as 6 mm, 3 mm and 12 mm, respectively. As shown in Fig. 5.1a, perfect magnetic conditions (PMC) were imposed on the x -boundary and perfect electric conditions (PEC) were imposed on the y -boundary to guide the propagating wave and to ensure the desired symmetry condition for plane wave propagation is maintained. For the test cases involving the PML, a N_{PML} layer PML media was applied along the z -axis at both ends of the structure which was backed by a PEC boundary, as shown in Fig. 5.1b. The PML conductivity along the z -axis was set greater than zero $\sigma_z > 0$ to achieve the desired attenuation. The value of σ_z was set as a function of the theoretical reflection factor R_{th} according to equations (3.55) and (3.56) as presented in Section 3.3.4. Since no attenuation was required along the x and y -axis the corresponding PML conductivities were set to zero (i.e. $\sigma_x = \sigma_y = 0$). A y -polarized TEM wave was launched by superimposing a sinusoidal modulated Gaussian pulse with a centre frequency of 30 GHz and bandwidth of 20 GHz across a plane located one node from the PML-medium interface. The observation node was set at the opposite end of the waveguide one node from the PML-medium interface. The entire problem domain was discretized using a uniform SCN mesh with a spatial discretization of $\Delta l = 0.25$ mm. All problems investigated were simulated at the maximum permissible time step $\Delta t = \frac{\Delta l}{2c}$ therefore no stubs were required in the mesh. In the PML region the 12-port mapped SCN-PML formulation described in Section 4.3.2 was employed for all tests carried out. This is because the computational domain interfacing the PML is isotropic and homogenous and can therefore modelled using the standard 12-port SCN. For anisotropic inhomogeneous or lossy media (or a combination of all) the 15-port mapped hybrid SCN would be most suitable.

The absorption performance of the PML was evaluated by extracting the numerical reflections generated using the reference solution method described in Section 3.3.4. This involved simulating a second identical wave guide but with a

length 100 mm which was set long enough such that the reflections do not propagate back to the observation point within the time period of the simulation. Numerical experiments which characterize the mapped SCN-PML based on different PML parameters follows.

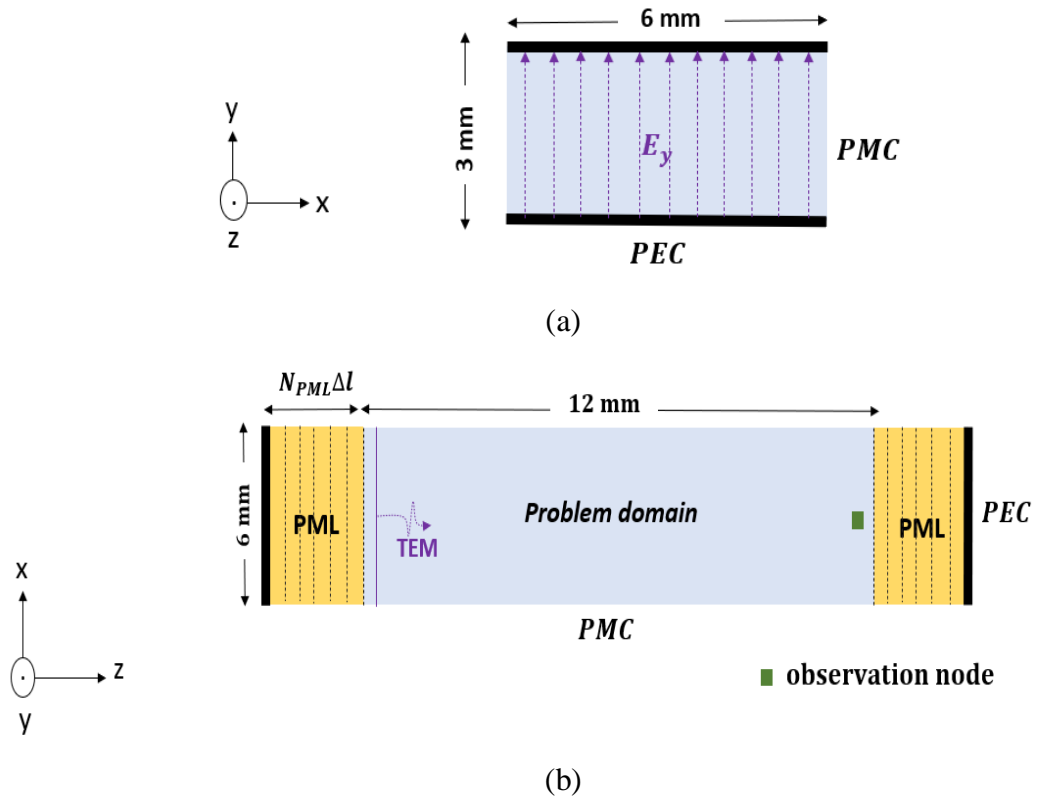


Figure 5.1. Geometry of the simulated wave guide (a) y - x plane view (b) x - z plane view showing E_y polarization and PMC and PEC conditions.

5.1.1 Influence Of The Conductivity Profile On The Mapped SCN-PML For Normally Incident Waves

In Chapter 2, it was demonstrated how the continuous PML equations achieves a perfect absorption for all incoming waves through an impedance matching scheme. However, numerical dispersion errors that arise due to underlying discretisation

scheme generate transitional reflections which reduce the accuracy of the solutions computed in the problem domain. A large contribution of these reflections arises at the medium-to-PML interface, and to mitigate against this unwanted effect, it is generally suggested to grade the conductivity across the PML medium from a near zero value at the first layer to a maximum value at the end layer. A schematic of a PML medium with constant and variable conductivity grading is shown in Figs 5.2a and 5.2b, respectively.

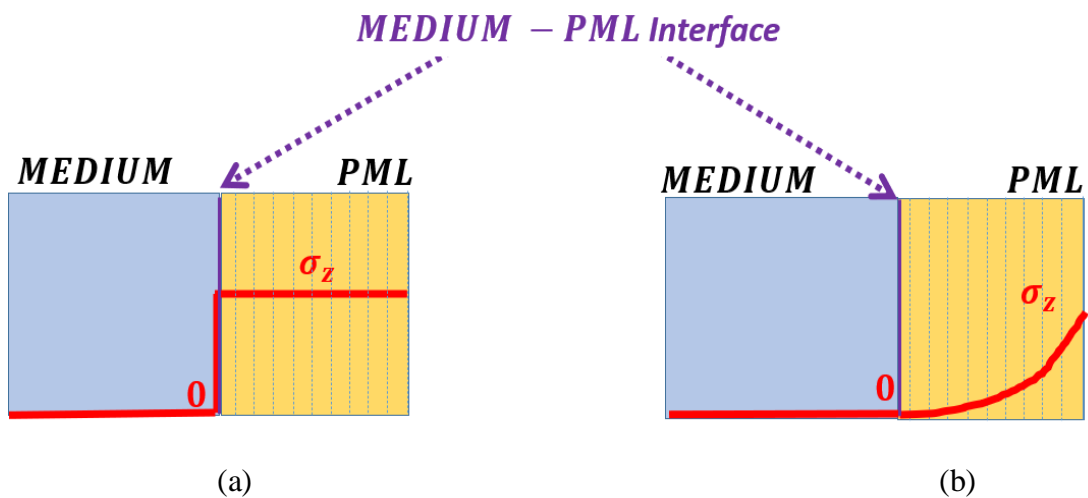


Figure 5.2 A PML with: (a) constant conductivity grading, (b) variable conductivity grading

Fig. 5.3 examines the reflections from the mapped SCN-PML for different conductivity gradings. A 10-layer mapped SCN-PML was employed in this investigation to allow for a smooth conductivity profile. The PML medium was backed by a PEC condition in order to properly observe the residual reflections after the PML round trip. As a comparison the same test was carried out on the SCN-PML formulated by Dubard *et al.* in [5.2]. The numerical reflections obtained from the mapped SCN-PML is shown in Fig. 5.3 where the influence of the conductivity profile of different theoretical reflection factors R_{th} (dB) are demonstrated. Figure 5.4 shows the results from the SCN-PML [5.2].

From Fig. 5.3 it can be seen that a graded conductivity profile has little effect on the overall reflection of waves impinged normally on the mapped SCN-PML medium. It is also clear that the numerical reflections generated by the mapped SCN-PML decrease linearly with decreasing theoretical reflection factor R_{th} (dB). Overall, this implies that a strong absorption is attainable by the mapped SCN-PML even in the presence of a sharp conductivity variation across the medium and PML region. This observation differs from the general behaviour shown in Fig 5.4 for the SCN-PML [5.2]. As shown in Fig 5.4, a smooth and gradual increase in conductivity obtains lower reflection levels than employing a constant conductivity profile across the PML. Furthermore, continually decreasing the theoretical reflection factor, R_{th} (dB), is shown to result in an increase in numerical reflections generated by the SCN-PML [5.2]. This observation is shown to be true for all conductivity gradings.

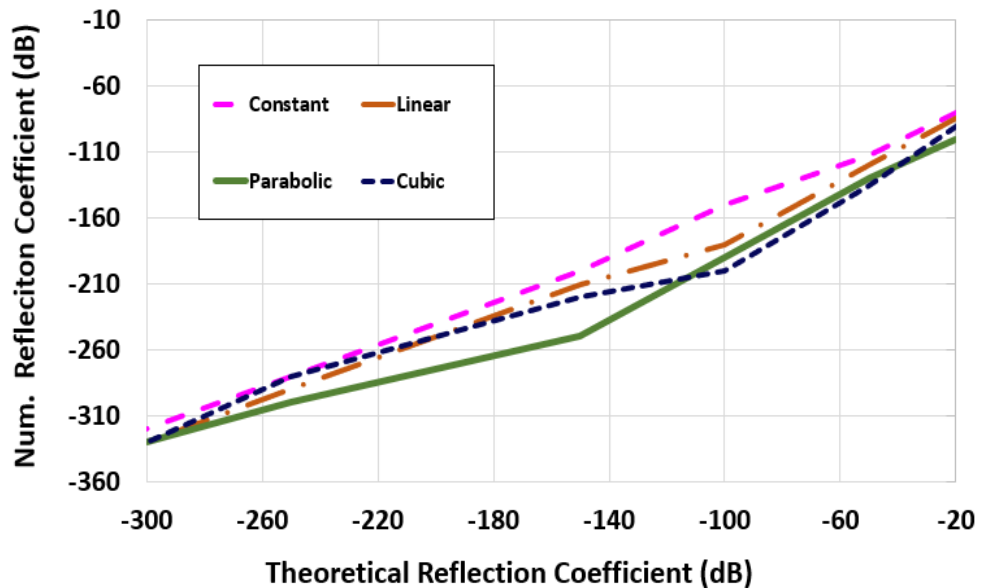


Figure 5.3 The influence of different conductivity profiles on the numerical reflection coefficient in the mapped SCN-PML.

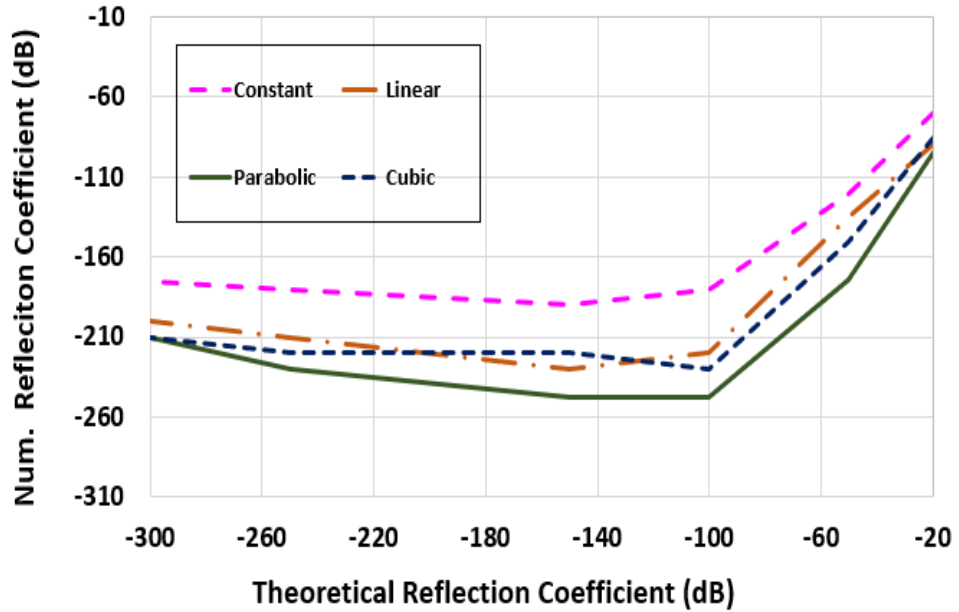


Figure 5.4 The influence of different conductivity profiles on the numerical reflection coefficient in the SCN-PML [5.2].

The results obtained in this investigation indicate that the mapped SCN-PML achieves a closer approximation to the desired continuous PML matched impedance condition. This explains the strong absorption (i.e. low reflection) achieved even in the presence of a sharp conductivity variation at the medium-to-PML interface. This unique behaviour arises due to the ability of the mapped SCN-PML to retain the underlying propagation properties of the transformed node. For normally incident waves the stub free SCN mesh exhibits zero dispersion [5.4]. Therefore, evident by the strong absorption shown in Fig 5.3., upon the complex coordinate mapping described in Chapter 4, this dispersion free property is retained by the mapped SCN-PML. Since there is a perfect transmission at the medium-to-PML interface all forward propagating fields are therefore exponentially attenuated in the TLM connect phase through the $e^{-\sigma_z \Delta t}$ factor (see Section 4.3.4). For this reason the dominant factor contributing to the attenuation of incident waves is the value of the PML conductivity σ_z set at the first layer which is determined by the value of the theoretical reflection factor R_{th} .

On the other hand, the sensitivity to sharp conductivity variation shown by previously published SCN-PML formulations [5.2], [5.3], [5.5] arises due to

dispersion errors introduced due to the use of stubs in these models. For this reason, in order to reduce numerical reflections generated in these models a smooth grading of conductivity must be applied across multiple PML layers.

5.1.2 Influence Of The Number Of PML Layers On The Mapped SCN-PML For Normally Incident Waves

In the previous section, the influence of different conductivity gradings applied across a mapped SCN-PML medium was investigated. Both a constant and variable conductivity profile were shown to achieve excellent absorption even in the presence of sharp conductivity variations at the medium-to-PML interface. In this section, the mapped SCN-PML is further characterized by investigating the influence of the number of PML layers employed. For different theoretical reflection factors R_{th} (dB) the numerical reflections generated by a mapped SCN-PML medium with $N_{PML} = 1, 2, 5, 15, 30, 40,$ and 50 layers was examined. For all experiments conducted the spatial discretization was kept constant at $\Delta l = 0.25 \text{ mm}$, therefore varying the number of PML layers N_{PML} translates to a variation in the thickness of the PML medium. In this test a constant conductivity grading was employed across the PML layer. The numerical reflection obtained are presented in Fig. 5.5. As similarly observed in Section 5.1.1 the theoretical reflection factor R_{th} (dB) is again shown to have the principal effect on the reflection performance of the mapped SCN-PML for the case of normally impinged waves. No significant distinction is observable in the reflection levels from increasing the number of PML layers. Again, this behaviour shows that a single layer of PML with high conductivity delivers the same numerical reflection as distributing the conductivity across multiple PML layers. This demonstrates a significant improvement in efficiency compared to existing discrete PML schemes [5.2], [5.5], [5.6] evaluated under similar test conditions which require the use of multiple layers to achieve a smooth conductivity grading.

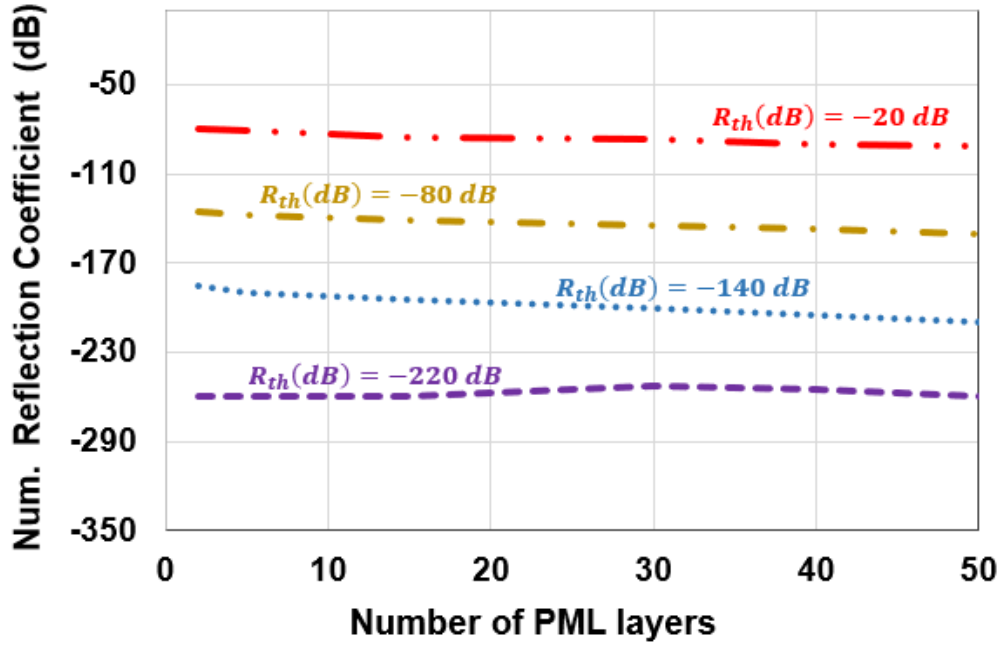


Figure 5.5 The numerical reflection coefficient as a function of number of layers for different theoretical reflection factors.

To further illustrate the efficiency of the mapped SCN-PML, the numerical reflection generated from a single layer was compared with the results obtained from different configurations of the SCN-PMLs published in [5.2] and [5.3] formulations and a matched boundary. The key results are presented in Fig. 5.6. where the SCN-PML configurations are characterised by the number of PML layers, the theoretical reflection factor and the conductivity profile used i.e. $(N_{PML}, 20\log_{10}R_{th}, \text{conductivity profile})$. The objective of this test was to find the configurations of SCN-PML which achieved a near perfect attenuation of the incident wave. Since the numerical noise floor for double precision floating point was identified to be at approximately 10^{-16} (i.e. $20\log_{10}(10^{-16}) = -320$ dB), below this level it is assumed a near perfect attenuation is obtained. As shown in Fig. 5.6, the SCN-PML implementations developed by Dubard *et al.* [2], and Le Maguer *et al.* [5.3] require 25 layers to obtain reflection levels below -290 dB; and so results in a $\frac{25 \times 2}{12} \times 100 = 166\%$ increase in the total nodes size compared to the matched boundary. This behaviour is in sharp contrast with the mapped SCN-PML which is shown to be

significantly more efficient since a single layer achieves reflections well below the numerical noise floor.

For illustrative purposes, Fig. 5.7 compares the time domain plot of the reflected field obtained from a single layer of the mapped SCN-PML with the zero reflected field obtained from the matched boundary. The strong attenuative behaviour of the mapped SCN-PML is demonstrated by comparing the amplitude of reflected field shown in Fig. 5.7 with the incident wave shown in Fig. 5.8. The inversion applied to the reflected field arises due to the PEC boundary reflection coefficient of $\Gamma = -1$. Note that the results from the matched boundary condition are not presented in Fig. 5.6 since a perfect absorption i.e. zero reflections (as shown in Fig. 5.7) was attained.

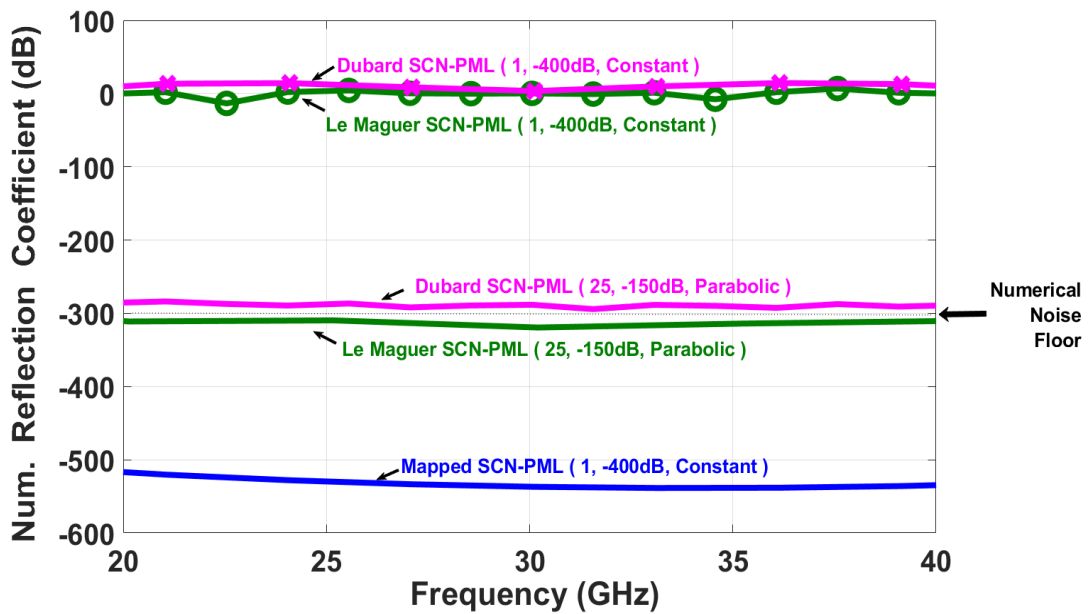


Figure 5.6 Numerical reflection versus frequency for waves normally impinging on various SCN-PML media terminated by a PEC condition.

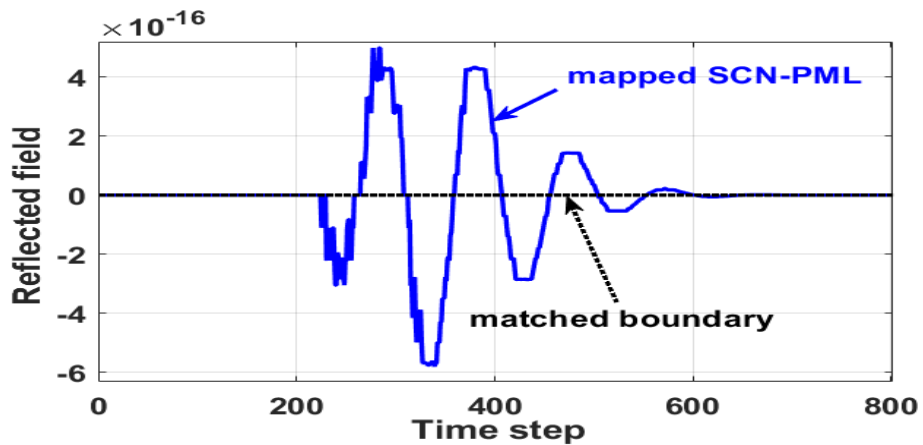


Figure 5.7 TLM time domain plot comparing the reflected field from the matched boundary and a single layer of mapped SCN-PML backed by PEC boundary.

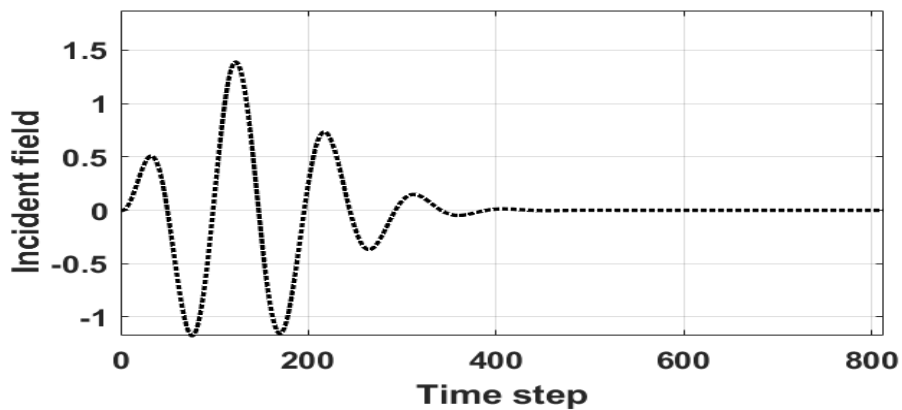


Figure 5.8 Time domain plot of the incident field

5.2 Performance Of The Mapped SCN-PML For Oblique Wave Incidence

In Section 5.1 the mapped SCN-PML was characterized for normally incident waves and the PML conductivity was demonstrated to have the dominant effect on the overall reflection performance. Most practical applications, however, require the attenuation of waves propagating with an arbitrary angle of incidence. Therefore, a more applicable characterization of the mapped SCN-PML should involve a study of the reflection performance for waves impinging from a wide range of angles.

This section extends the investigation carried out in Section 5.1 and studies the behaviour of the mapped SCN-PML applied to a rectangular metal waveguide. This problem is an excellent test case of PML and is generally regarded as the canonical application upon which numerous PML implementations have so far been validated. This is owed to the structure of the rectangular waveguide which allows all angles of incidence to be tested. In particular, the results from this investigation will highlight how the TLM numerical dispersion errors impact the accuracy of the mapped SCN-PML.

The reflection performance was investigated for an empty WR-28 rectangular waveguide with x , y and z dimensions given as 7.116 mm, 3.556 mm and 20 mm, respectively. The simulation parameters used were identical to the tests carried out in Section 5.2. However, unlike the previously investigated structure, PEC boundary conditions were applied on both the x and y walls and a matched boundary condition or SCN-PML medium was applied on the z -axis to simulate an infinite outward propagation. In the latter case, the PML medium was backed by a PEC wall. The dominant TE_{10} mode was excited by an amplitude modulated Gaussian pulse with a centre frequency of 32 GHz and a bandwidth of 12 GHz. The computational space was similarly discretized using a spatial discretization of $\Delta l = 0.25$ mm. The plane of excitation was located at one node from the medium-to-PML interface and the observation node was set at the other end of the waveguide – one node away from the medium to PML. The reflection coefficient was again computed using the reference solution of a longer waveguide with a length of 100 mm.

5.2.1 Influence Of The Conductivity Profile On The Mapped SCN-PML For Oblique Incidence Propagation

In this section the same tests carried out in Section 5.1.1 are repeated but now applied to the study of the mapped SCN-PML's absorption for the TE_{10} mode in a WR-28 rectangular waveguide. The TE_{10} mode was excited by an amplitude

modulated Gaussian pulse of center frequency 35.5 GHz and a bandwidth of 12 GHz. The influence of different PML conductivity gradings applied across a 10-layer mapped SCN-PML medium is examined.

The reflection performance obtained from a constant, linear, parabolic and cubic conductivity grading is shown in Fig. 5.9. As shown, applying a constant conductivity grading generates higher reflections at the medium-to-PML interface. Applying either a linear, parabolic or cubic conductivity profiles is shown to improve the reflection performance by approximately -13 dB. Nevertheless, the overall absorption of the mapped SCN-PML is significantly lower than the case of normal incidence shown in section 5.1.1. As shown, approximately -265 dB lower reflections is attainable for normally incident waves (Fig. 5.3) compared to the oblique incidence case. The above results demonstrate how the TLM numerical dispersion errors impact the accuracy of the mapped SCN-PML in practical simulations. It is noted that this behavior is also similarly reported in the SCN-PMLs [5.2], [5.3], [5.5].

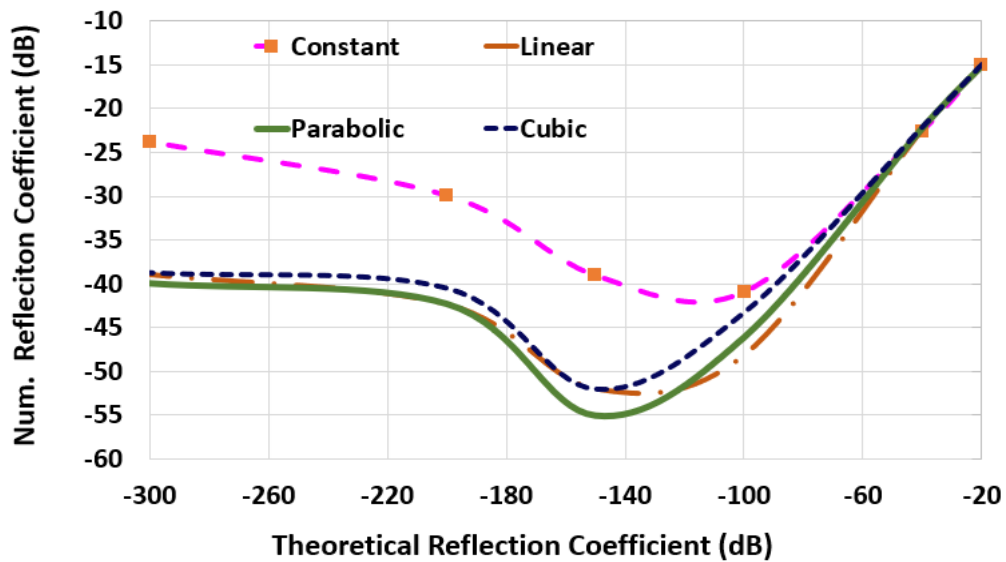


Figure 5.9 Numerical reflections as a function of theoretical reflection coefficient (dB) for constant, linear, parabolic and cubic PML conductivity gradings.

5.2.2 PML Tuning

As shown in the previous section, practical applications require a SCN-PML medium with a graded conductivity profile in order to reduce the occurrence of transitional reflections. Unlike the case of normally impinged waves where a single mapped SCN-PML layer demonstrated a near perfect attenuation of outgoing waves, multiple PML layers must now be employed to ensure a smooth conductivity grading is applied across the PML medium. Nevertheless, the decision of the number of PML layers used and the choice of theoretical reflection factor R_{th} is not straightforward. The common approach is more empirical in nature and typically requires some degree of PML tuning and variations of the control parameters to obtain the best reflection performance for a given PML medium thickness. In this section the PML tuning process will be briefly described which will be applied to obtain the optimum PML parameters required for the WR28 waveguide test case.

A schematic describing the steps involved in the PML tuning process is given in Fig 5.10. As shown the first step involves setting the number of PML layers N_{PML} to a fixed value. For this choice of N_{PML} several TLM simulations are run where the reflection performance for a set of R_{th} values is explored. The aim of this exploration is to identify an optimum R_{th} value. At the end of each exploration stage the reflection performance for each R_{th} value is evaluated, and if the results obtained are unsatisfactory the above iterative process will be repeated for a different value of N_{PML} . Ultimately, at the end of the tuning process a suitable combination of N_{PML} and R_{th} pairs should be identified depending on the required design requirements.

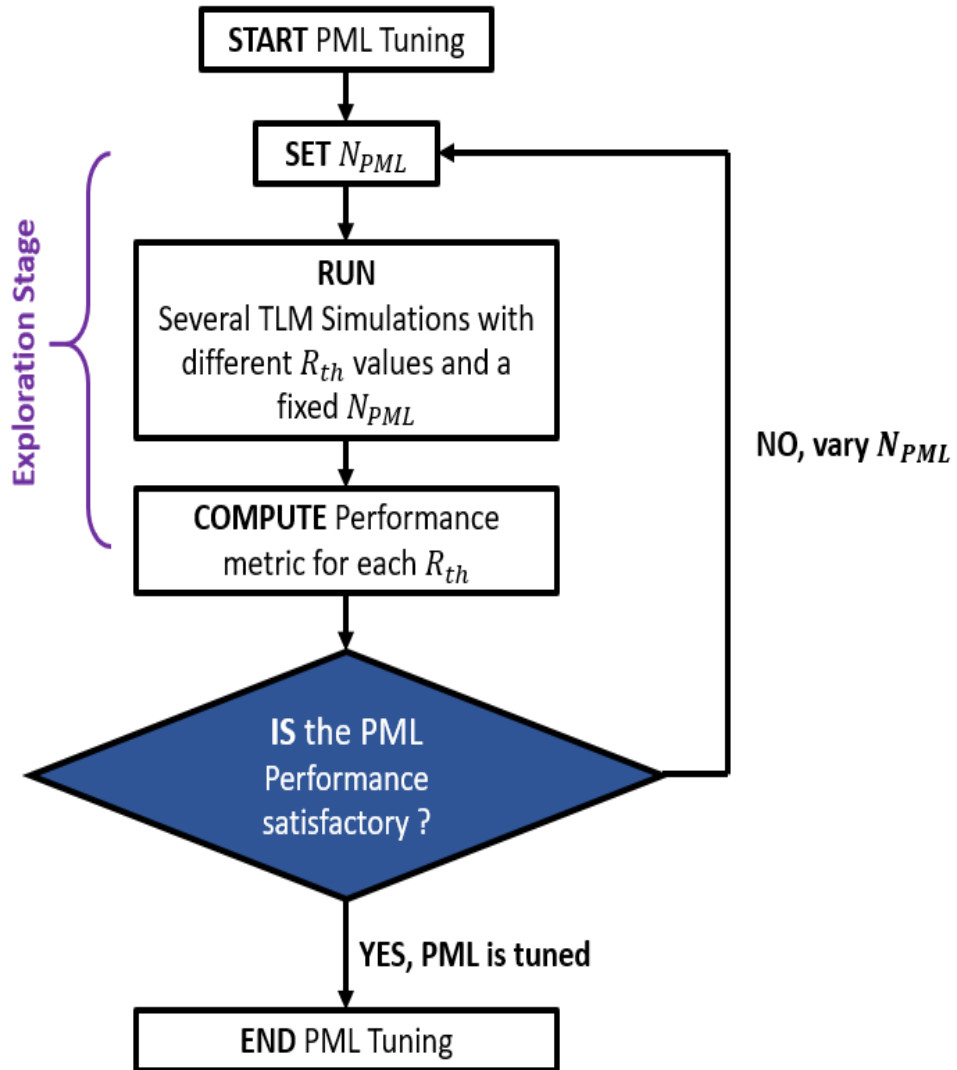


Figure 5.10 Schematic showing the PML tuning process.

The tuning process described above is now applied to the WR28 waveguide test case. For the first iteration the number of PML was set as $N_{PML} = 15$ and different theoretical reflection factors were explored. The results obtained for $R_{th}(\text{dB}) = \{-40 \text{ dB}, -160 \text{ dB}, -200 \text{ dB}, -300 \text{ dB}\}$ are shown in Fig. 5.11. As shown, for the choice of $N_{PML} = 15$ the highest reflection coefficient was demonstrated by $R_{th}(\text{dB}) = -40 \text{ dB}$ whilst the lowest reflection coefficient was demonstrated by $R_{th} = -160 \text{ dB}$. By exploring other N_{PML} values the overall behavior of the PML performance can be demonstrated for this test case.

The relationship between the average numerical reflection coefficient computed across the frequency range of operation (i.e. 29 GHz to 41 GHz) and the number of PML layers is thus presented in Fig. 5.12. In this test the parabolic conductivity grading was employed across the PML media. As shown, increasing the number of PML layers results in lower reflections for all values of R_{th} (dB). This behavior is expected, and it arises because of two factors. Firstly, an increase in the PML layer means a smoother conductivity grading is applied across the PML medium which in turn reduces the reflections at the medium-to-PML interface. Secondly, increasing the number of PML layers means the attenuated waves will experience a larger damping distance. For these reasons, the lowest reflection performance is demonstrated by a single PML layer. By setting $N_{PML} > 20$ layers reflections lower than -65 dB can be achieved. Nevertheless, it is noted that linearly increasing N_{PML} does not translate into linear reduction of the PML reflections.

Figure 5.13 compares the numerical reflection generated by a 25-layer mapped SCN-PML with the results obtained from the matched boundary and the SCN-PML [5.2], [5.3]. The limitation of the matched boundary termination in absorbing the off-normal waves is clearly seen by the high reflections produced. A similar absorption performance to the mapped SCN-PML is shown by the SCN-PML [5.2], [5.3] all of which demonstrate a substantial absorption (>40 dB) over the matched boundary condition. Nevertheless, the improvement in accuracy shown is at the cost of increasing the computational burden.

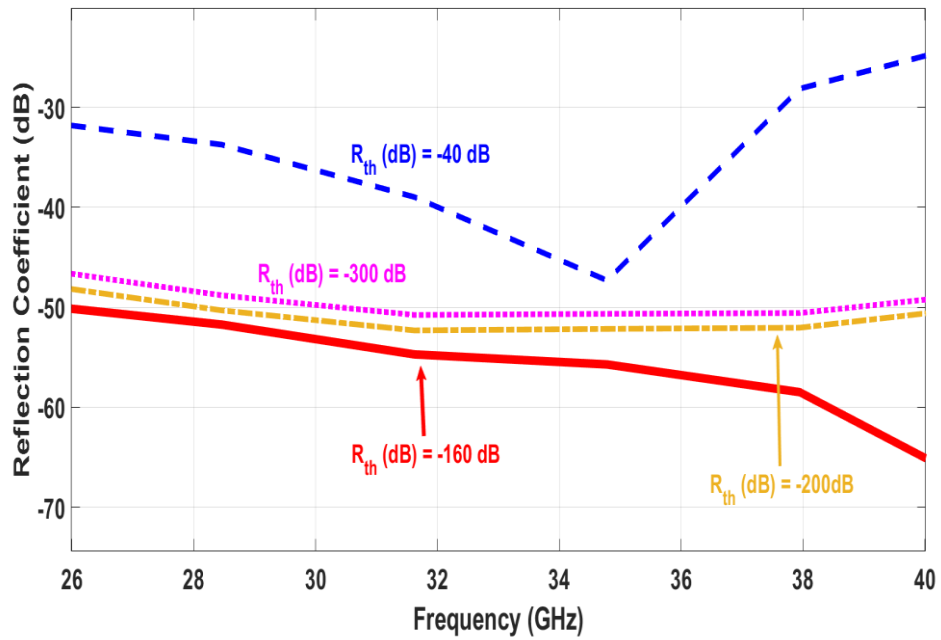


Figure 5.11 Numerical reflection coefficient versus frequency from a TLM simulation of WR28 rectangular waveguide terminated by 15-layer mapped SCN-PML backed by a PEC boundary.

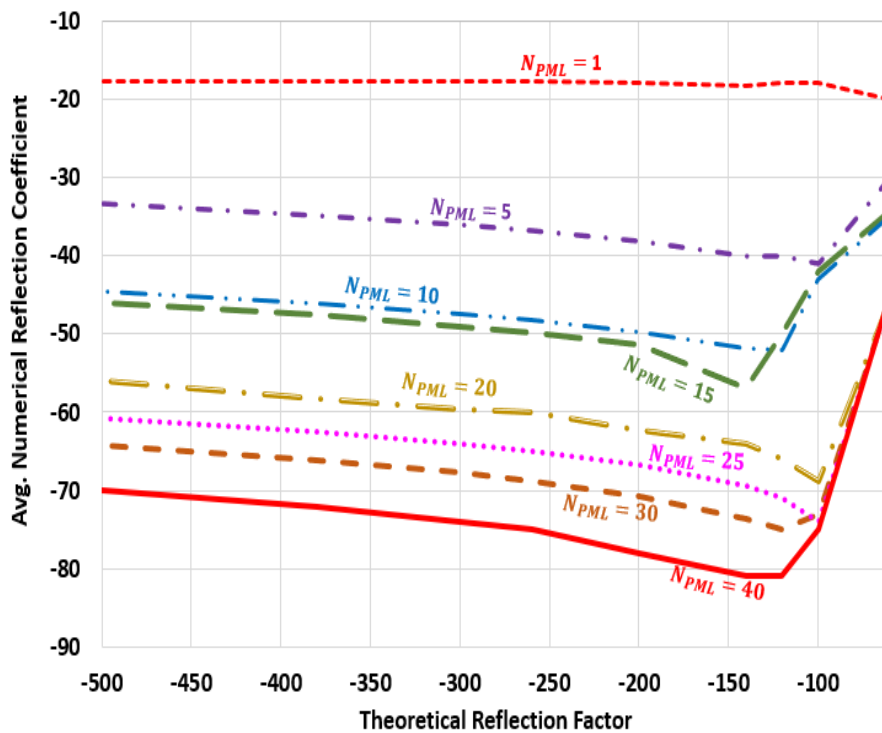


Figure 5.12 Numerical reflection coefficient versus theoretical reflection factor for different number of PML layers.

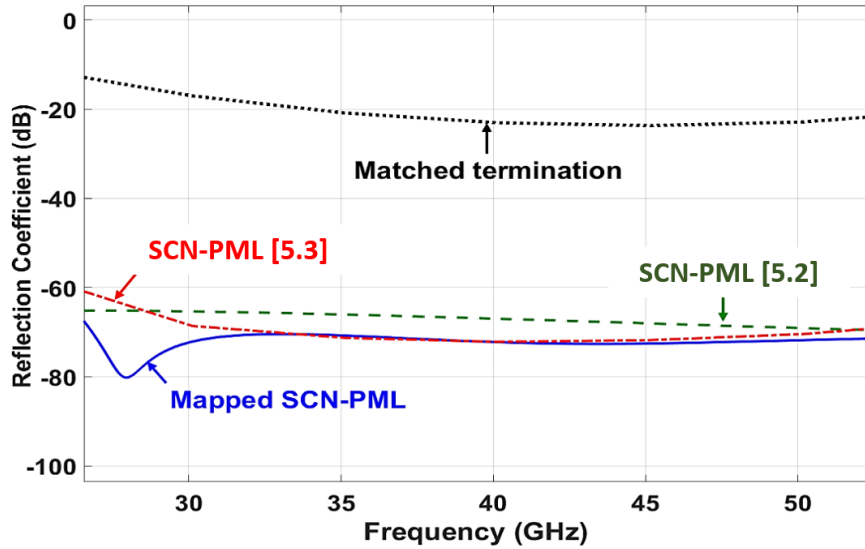


Figure 5.13 Reflection coefficients obtained from a TLM simulated empty rectangular waveguide WR-28 truncated by matched boundary and various SCN- PMLs employing a parabolic conductivity grading.

In addition to the reflection performance, another important factor to consider when deciding the number of PML used is the computational costs incurred due to the PML medium. To evaluate this effect, the computational burden from increasing the number of PML N_{PML} is evaluated in terms of the simulation run time and the memory usage. To demonstrate the sole contribution of the PML on the overall computational costs, the relative increase in run time and memory usage were computed which are presented in Figs 5.14 and 5.15, respectively. The results are also shown for different lengths of the waveguide to illustrate the computational demand of the PML in relation to the size of the problem domain. As expected, the run time and memory are shown to grow with increasing number of layers. However, as the size of the computational domain is increased the relative impact of the PML on the run time and memory is shown to reduce. This indicates that the benefits of the mapped SCN-PML is more realized in large scale problems since a higher accuracy can be achieved without incurring significant computational costs. For the present test case with waveguide length equal to 20 mm a 10 mapped SCN-PML (i.e. a total of 20 layers applied at both ends of the waveguide) is shown to be a good choice since a reflections of -50dB

can be achieved whilst the run time and memory usage contributed by PML only increases by a factor of 0.5.

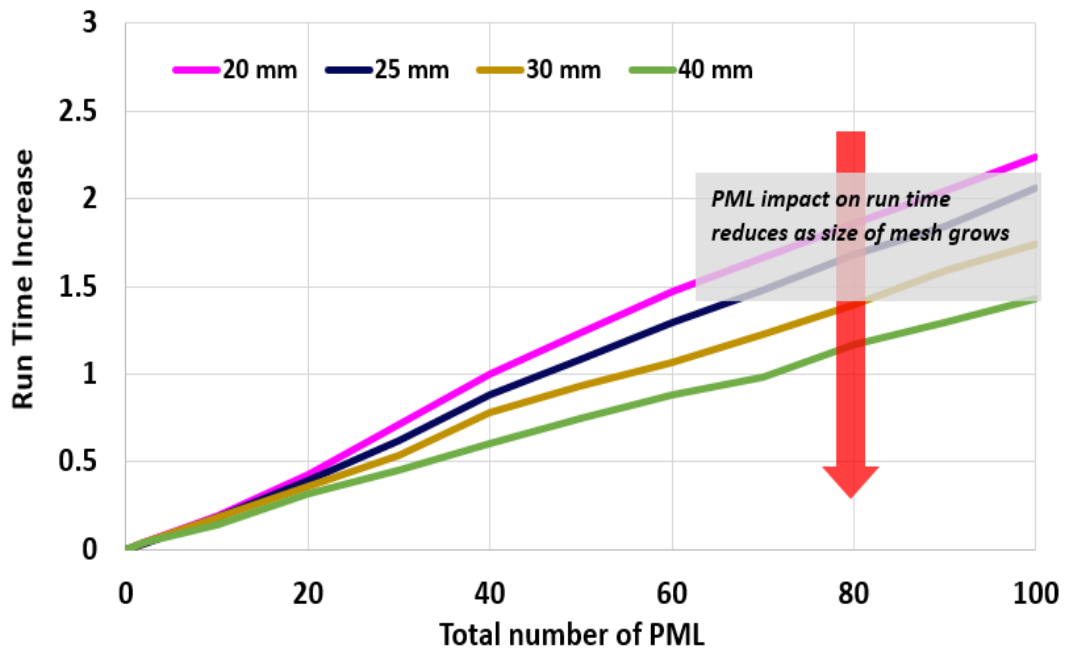


Figure 5.14 The relative increase in TLM simulation run time versus total number of mapped SCN-PML layers for different waveguide lengths.

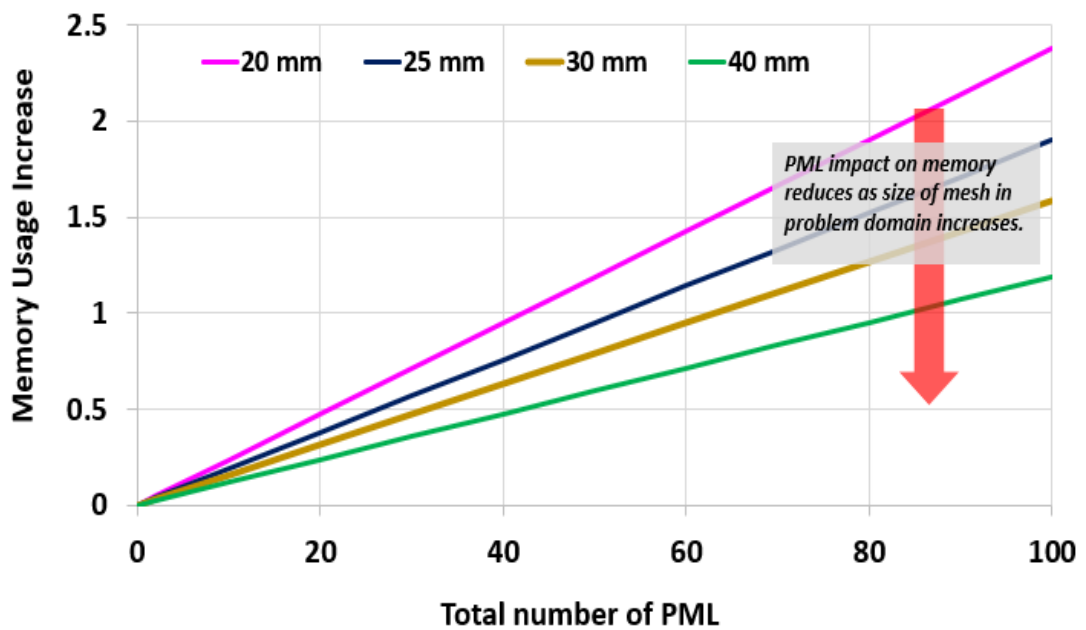


Figure 5.15 The relative increase in memory usage versus total number of mapped SCN-PML layers for different waveguide lengths.

5.3 Stability Of The Mapped SCN-PML

Stability is a critical requirement of all numerical methods. Whilst the few published SCN-PML implementations demonstrate a good absorption performance, with approximately -60 dB numerical reflection shown in the waveguide test case, they however exhibit a weak temporal stability, which in some cases generate exponentially growing solutions in the problem domain [5.2], [5.3], [5.5], [5.7]. This degrading phenomenon is practically unacceptable, and its removal is a primary motivator of the approach taken in the development of the mapped SCN-PML.

As described in Chapter 4, a key distinction of the mapped SCN-PML compared to the published SCN-PML formulations is its reliance on the derivation of a field-to-circuit equivalence for the PML medium. This approach to implementation allows the stretched coordinate PML theory [5.1] to be modelled as a special type of SCN node with stretched circuit parameters. Seeing that the un-stretched SCN is provably stable it is expected that this desirable temporal behavior must also be retained by the mapped SCN-PML since the required transformation/stretching, as shown in Section 4.3, is appropriately commuted to the transmission line parameters through the introduction of complex impedances/admittances and complex propagation delays

The objective of this section therefore is to investigate the temporal behavior of the mapped SCN-PML. The first stability test carried out examines the response of the mapped SCN-PML to waves impinging on the medium for long durations of time. A practical application where such behavior is observed is in problems involving high quality-factor radiating structures. Since this test is solely focused on examining the time domain response, an electric dipole oscillating at 1 GHz with a very narrow bandwidth was used to inject energy into a cubic volume. As illustrated in Fig. 5.16, the dipole source was placed at the center of a 11 mm \times 11 mm \times 11 mm uniformly meshed grid with $\Delta l = 1$ mm. All edges of the domain were surrounded by strong single PML layers with $\sigma_{x,y,z} = 18$ S/m which were backed by a PEC boundary

conditions. The observation point was set at a node two cells away from the cube corner. The normalized electric field obtained in the time domain from simulations employing the mapped SCN-PML is shown in Fig. 5.17 which is compared against the analytical time solution of a Hertzian dipole [5.8]. As shown, the results obtained with mapped SCN-PML implementation are in excellent agreement with the reference result and no instabilities are observed at all. As a comparison, the results obtained from the SCN-PML [5.2] is shown in Fig. 5.18 which exhibit an onset of instability after 600 iterations. It is noted that the exponential growth shown was generated for low to high PML conductivity $\sigma_{x,y,z}$ values. However, this instability can be delayed by backing the SCN-PML [5.2] with a matched boundary and choosing lower conductivity $\sigma_{x,y,z}$ values. On the other hand, no late time instabilities were observed with the mapped SCN-PML for all parameter choices.

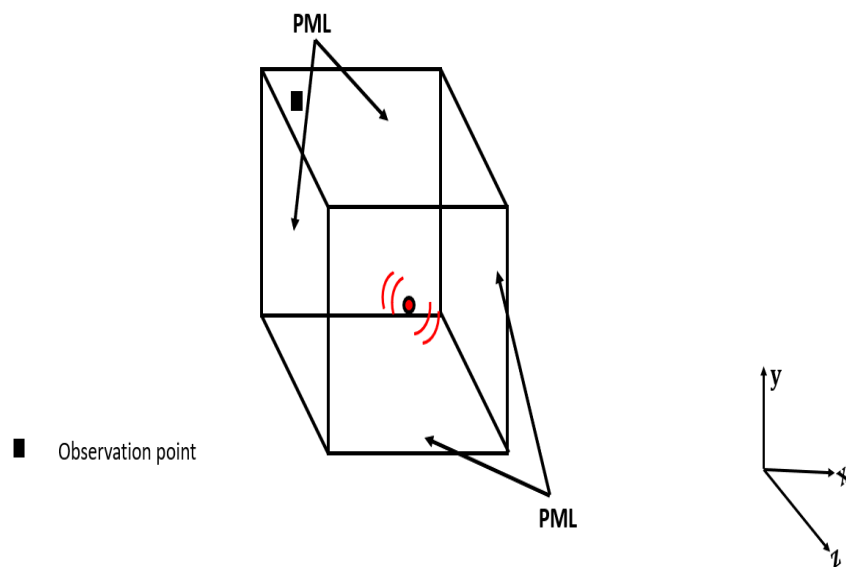


Figure. 5.16 Electric dipole source radiating in a cubic computational domain with PML applied on all edges.

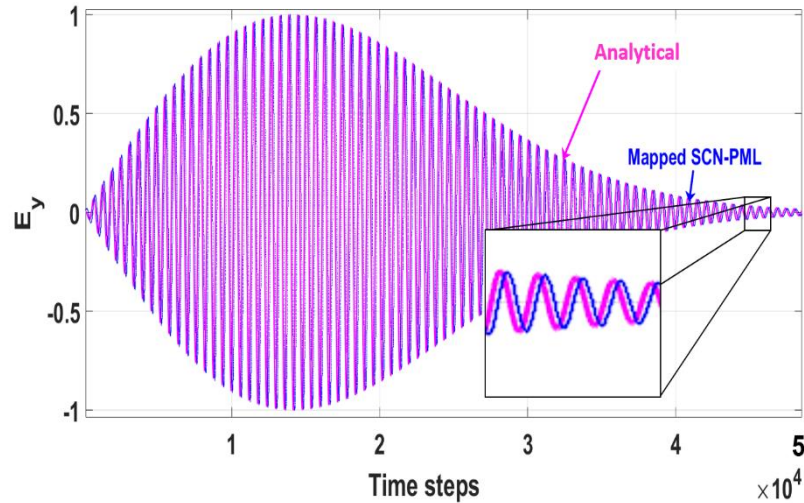


Figure. 5.17 Normalized E_y field obtained in the time domain from a narrow bandwidth dipole electric source radiating in a computational domain terminated with the mapped SCN-PML.

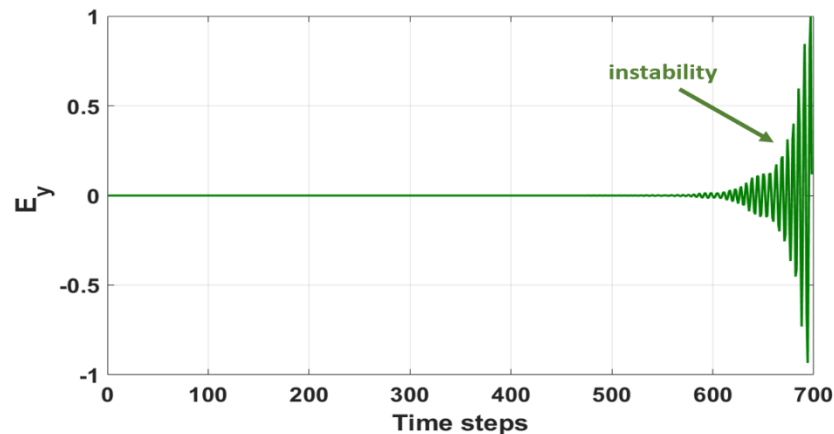


Figure. 5.18 Normalized E_y field obtained in the time domain from a narrow bandwidth dipole electric source radiating in a computational domain terminated with the SCN-PML [5.2]. Graph shows the early onset of an exponentially increasing field solutions.

A second test was conducted to evaluate the long time behavior of the mapped SCN-PML in the presence of strong evanescent energy impinging on the PML medium. For this investigation, the waveguide iris test case was simulated. In this application, the published SCN-PML have been reported to generate numerical instability [5.2], [5.3], [5.5], [5.7]. Therefore, to allow for a wider comparison the

simulation set up was identical to that reported in [5.7] where the WR28 waveguide studied in section 5.2 was loaded with a capacitive iris of dimensions as illustrated in Fig. 5.19. The iris was placed close to the PML (5 nodes away) to ensure strong evanescent energy coupling with the PML interface. This test configuration was solely chosen to evaluate the temporal behavior. In practice it is suggested to place the PML medium at greater than a wavelength away from the scattering structure to avoid absorption of radiation that would otherwise remain in the simulation. A 25 layer PML with high conductivity $\sigma_z \gg 0$ was employed by setting the peak conductivity to $\sigma_{max} = 46 S/m$ (i.e. $R_{th}(dB) = -500 dB$). The PML conductivity was graded parabolically across the PML medium which was backed by a PEC boundary. The observation and excitation were made at the same node at the opposite ends of the waveguide.

The time domain plot of the E_y component is presented in Fig. 5.20 which is compared with the results using the SCN-PMLs [5.2] and [5.3]. As shown, instabilities arise when employing both [5.2] and [5.3]. It is observed that the temporal behavior of the PML formulation proposed by [5.3] can be improved by setting the damping factor greater than 1, although this detrimentally increases the unphysical reflection from the PML, and typically instabilities still occur after $\sim 30,000$ time steps. The mapped SCN-PML is shown to exhibit no instability even with the iris placed at very close proximity to the PML. This demonstrates a substantial improvement in the temporal performance over existing SCN-PML schemes simulated in a similar context [5.2], [5.3], [5.5], [5.7] which is regarded as the major advantage of the mapped SCN-PML scheme.

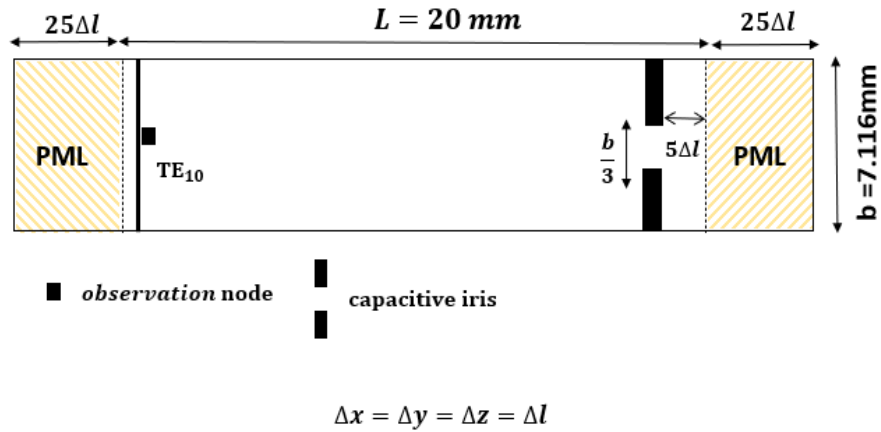


Figure 5.19 Geometry of the rectangular waveguide WR-28 loaded with capacitive iris.

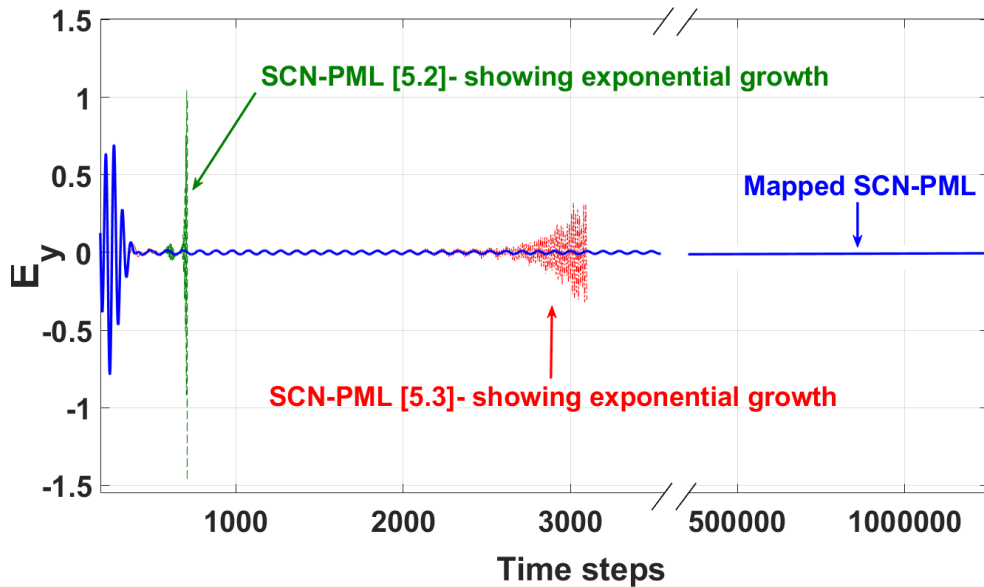


Figure 5.20 Time domain waveform of an empty waveguide WR-28 loaded with a capacitive iris and truncated by different SCN-PMLs terminated with a PEC boundary condition.

5.4 Summary

In this chapter, the absorption performance of the mapped SCN-PML was characterized using normal and oblique incidence waveguide test conditions under different variations of the PML control parameters. An excellent absorption was demonstrated for waves impinged normally on the mapped SCN-PML medium. This

behavior arises due to the approach taken in the development of the mapped SCN-PML formulation which retains the underlying propagation properties of the transformed node. Due to this, the inherent dispersion free property of the SCN mesh under normal propagation is retained. In this manner, the mapped SCN-PML maintains a strong absorption even in the presence of a sharp conductivity variation across the medium-to-PML interface. In such conditions a single mapped SCN-PML layer with sufficiently high PML conductivity $\sigma_z \gg 0$ can be deployed to achieve a near perfect attenuation of the incoming waves. Compared to the previously published SCN-PML schemes which require a smooth conductivity to be applied across multiple PML layers, the mapped SCN-PML is demonstrated to be more efficient in this case.

The excellent performance observed for normal incidence waves degrades in the case where the incoming waves are impinged from an off-normal angle. For oblique incidence waves, transitional reflections were shown to be generated by the mapped SCN-PML, and similar to other SCN-PML schemes a graded conductivity profile must be applied across the mapped SCN-PML medium. Under such conditions, the limitation of the matched boundary is evident. The reflections generated by the matched boundary is shown to be approx. -20 dB which is significantly higher than the -65 dB achieved by the 25-layers of the SCN-PML.

In practical applications, where waves are impinged from an arbitrary angle of incidence, the number of PML layers employed was shown to be the primary factor used to reduce the PML reflections. However, as expected, this is shown to come at a cost of an increase in computational demand. Nevertheless, the relative computational burden incurred by the PML medium decreases as the complexity or scale of the problem domain increases. It is in such test conditions that the PML benefits of improved accuracy can be truly realized. To optimize the PML design a guideline for tuning the PML was briefly described. Through this the overall absorption behavior for a given test condition can be obtained which could reveal the most suitable (and optimum) combinations of PML parameters to achieve a target reflection performance.

Finally, the excellent temporal stability of the mapped SCN-PML was demonstrated through the canonical waveguide iris test case. Compared to published SCN-PML schemes no appearance of instabilities was shown in the mapped SCN-PML even in the presence of high evanescent energy interacting with the PML interface. As an additional test the temporal response of the mapped SCN-PML for waves impinged on the layer for long durations of time was investigated. no long-term instabilities were observed in this test case which further corroborates the strengths of the mapped TLM-PML framework.

The next chapter will further demonstrate the advantages of the mapped SCN-PML for improving the computational efficiency and accuracy of 3D electromagnetic TLM simulations. The superiority of the proposed formulation over the TLM matched boundary shall be demonstrated by its application to topical electromagnetic scattering and radiation simulations.

References

- [5.1] W. C. Chew and W. H. Weedon, "A 3D perfectly matched medium from modified maxwell's equations with stretched coordinates," *Microwave and Optical Tech. Lett.*, vol. 7, no. 13, pp. 599–604, 1994.
- [5.2] J. L. Dubard, and D. Pompei "Optimization of the PML efficiency in 3-D TLM method." *IEEE Transactions on Microwave Theory and Techniques*; 48(7):1081–1087, 2000.
- [5.3] L. Maguer, and M. M. Ney, "Extended PML-TLM node: an efficient approach for full waveanalysis of open structures." *Int. J. Numer. Model.*, vol. 14 , pp. 129–144, 2001.
- [5.4] P. B. Johns, "A symmetrical condensed node for the TLM method," *IEEE Trans. Microwave Theory Tech.*, vol. MTT-35, no. 4, pp. 370-377, Apr. 1987.
- [5.5] T. W. Kang, C. Christopoulos, and J. Paul, "Implementation of the stretched coordinate-based PML for waveguide structures in TLM". *International journal of numerical modelling electronic networks. Devices and fields*. Vol. 18, pp. 107-118, 2005.

- [5.6] K. Sankaran, "Accurate domain truncation techniques for time-domain conformal methods," Ph.D dissertation. ETH Zurich, 2007.
- [5.7] S. Le Maguer, N. Pena, and M. M. Ney, "Matched absorbing medium techniques for full-wave TLM simulation of microwave and millimeter-wave components, *Ann. Telecommun.*, vol. 53, no. 3–4, pp. 115–129, Mar.–Apr. 1998.
- [5.8] H.G. Schantz. "Electromagnetic energy around Hertzian dipoles." *IEEE Ant. Prop. Magazine*. vol.43, no.2, pp.50-62, 2001.

Chapter 6

Mapped SCN-PML in Practical Electromagnetic Simulations

In this chapter, the effectiveness of the mapped SCN-PML in practical electromagnetic simulations will be demonstrated. The applications that will be studied include, (i) simulating the transmittance of planar Frequency Selective Surfaces (FSS) assumed to be infinitely periodic, (ii) investigating the scattering from a metallic body, (iii) simulating the coupling between two dipole antennas, and finally (iv) terminating the domain of inhomogeneous media.

6.1 Planar Periodic Structures

The study of the electromagnetic scattering from periodic structures is a subject of great interest within the electromagnetic community. This is due to the atypical properties they possess which find application in many novel engineering designs. Owing to the numerous opportunities available, various numerical techniques have been developed for analyzing the electromagnetic response of these structures. Amongst these, frequency domain integral equation methods, e.g. the Method of Moments (MoM), are extensively used because of their high accuracy and low computational costs [6.1]. However, these methods are less suited to complex inhomogeneous structures, in which case popular volumetric based methods, such as the FDTD, FETD and TLM [6.2]-[6.4] methods, are applied. While each technique

differs at the solver level, the general and more efficient simulation approach is to analyze only a unit cell of the periodic structure. This is as illustrated in Fig. 6.1 for a FSS constructed from repeating Jerusalem cross (JC) elements. In order to account for an infinite array of elements, periodic boundary conditions (PBCs) are applied along the unit cell walls. Floquet's (or Bloch's) theorem describe the field interaction inside periodic structures and thus form the mathematical background upon which the PBCs are formulated [6.3]. For a periodic structure with periodicity p_x along the x direction, incorporating the PBC ensures that the fields at the boundaries $x = 0$ and $x = p_x$ are the same except for a time shift. The fields at the boundary $x = 0$ can thus be expressed as

$$E_y(x = 0, y, z, t) = E_y(x = p_x, y, z, t - T_{dx}) \quad (6.1)$$

where $T_{dx} = k_x \frac{p_x}{c}$ represents the time delay.

In addition to the incorporating PBCs, absorbing boundary conditions (ABCs) must be applied in the direction perpendicular to the unit cell plane to effectively truncate the domain as seen in Fig. 6.1b). Nonetheless, there are limitations to the periodic unit-cell approach, e.g., it neglects the edge effects that occur in practice where a finite number of elements are used. However, these assumptions are acceptable as long as the structure is sufficiently large. It is also assumed that the structure is flat i.e. that its curvature is small compared to wavelengths of interest.

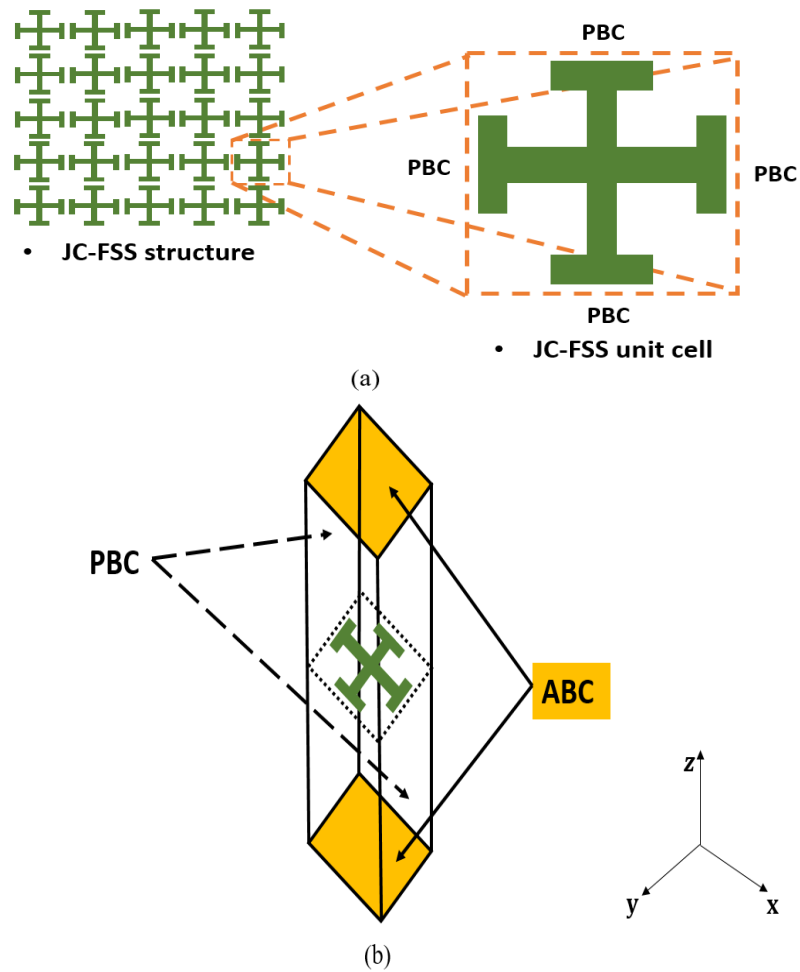


Figure 6.1.(a) A schematic showing a Jerusalem Cross FSS and the corresponding periodic unit cell with PBC applied on the peripheral walls (b) The unit-cell based model showing the ABCs applied in the non-periodic direction.

Two main challenges arise when simulating periodic structures using the TLM method. First, the TLM implementation of a generalized PBC is nontrivial. For normally incident plane waves, incorporating simple magnetic and electric walls is satisfactory since there is no phase shift between the periodic cells. However, for plane waves with oblique incidence a phase shift must be applied. This is challenging in time domain techniques since future field values are required in the computation. Several methods were proposed to address this, most of which employ an approximation of Floquet-Bloch's theorem and are more established in FDTD simulations [6.2]- [6.4] than in TLM method [6.5].

Second, a high-quality ABC such as the PML, is needed to properly truncate the domain in the out-of-plane direction. As formerly discussed in this thesis, the PML formulations in TLM have a weak stability which is particularly exacerbated in the presence of strong evanescent energy; thus, appropriate late time temporal behavior cannot be guaranteed. In contrast, analytical ABCs and the matched boundary ABC are computationally inefficient in these applications because they require a significantly extended computational domain to allow the strongly evanescent fields to be fully attenuated before reaching the truncation boundary.

In Chapter 5, the mapped SCN-PML formulation demonstrated an effectiveness in absorbing waves incident from oblique angles. It is attractive to further investigate the absorption and overall temporal behavior in applications involving waves incident from grazing angles; as well as, to evaluate the stability in the presence of strong evanescent fields. For this reason, the remainder of this section shall focus on investigating the effectiveness of the mapped SCN-PML in truncating the out of plane computational domain of different unit-cell based FSS simulations.

6.1.1 Simulation Setup

The simulation set up of the problem investigated is given in Fig. 6.2. As shown, a unit-cell model of an FSS was inserted at a distance $D=L/2$ along the z axis. The incident plane and observation plane are located at opposite sides to the FSS structure. Magnetic wall conditions were imposed on the x boundary and electric wall conditions were imposed on the y boundary. The PML region with a thickness of L_{pml} mm was applied at both ends of the structure which was backed by a standard TLM matched boundary condition. The PML conductivity was quadratically increased from zero to a maximum value σ_{max} S/m along the z direction of the PML region.

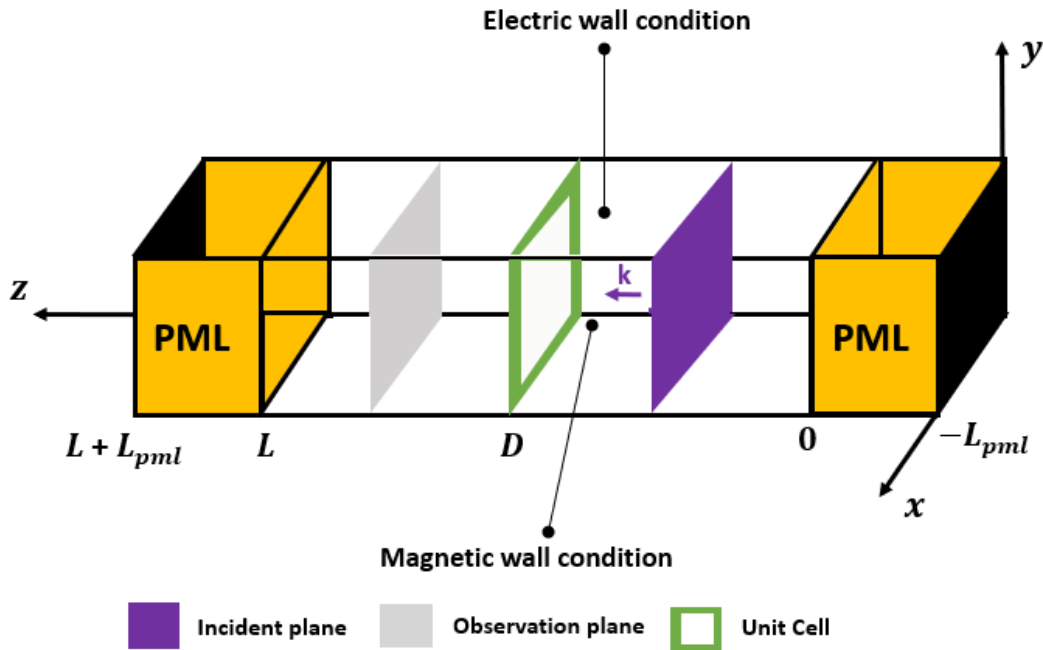


Figure 6.2. The simulation set up for analyzing the unit-cell FSS model.

6.1.2 Numerical Results

The transmittance of two unit-cell FSS patch upon illumination from a wide band normal incidence TEM Gaussian pulse was first investigated. A Gaussian pulse excitation with a center frequency of 15 GHz and a bandwidth of 30 GHz was imposed on the incident plane. Two canonical structures whose geometry and dimensions are given in Fig. 6.3 were chosen. They are referred to as a Jerusalem Cross Frequency selective surface (JC-FSS) and a Square loop FSS. Both structures were modeled as highly conducting lamina surfaces with zero thickness. The entire computational domain was discretized using a uniform mesh with a spatial discretization of $dl = 0.4$ mm ($dl = \frac{\lambda}{25}$) where $\lambda = 10$ mm is the wavelength at the maximum frequency of interest. This choice of dl was chosen as this was found to result in convergence for the frequencies of interest and particularly given the sharp geometrical features of the JC-FSS. Therefore, the unit cell of JC-FSS and Square loop FSS were discretized into 38×38 and 50×50 nodes, respectively. All problems were simulated at the maximum

permissible time step $dt = \frac{dl}{2c}$. The magnitude of the average transmitted power was computed as

$$P_t = \left| \left(\frac{\mathcal{F}(E_{AV}^t)}{\mathcal{F}(E_{AV}^i)} \right) \right|^2 \quad (6.1)$$

where $\mathcal{F}(\cdot)$ represents a Fourier transform function, E_{AV}^t is the average of the electric field observed across the observation plane and E_{AV}^i is the average of the incident electric field that was obtained by running the simulation without the unit cell present.

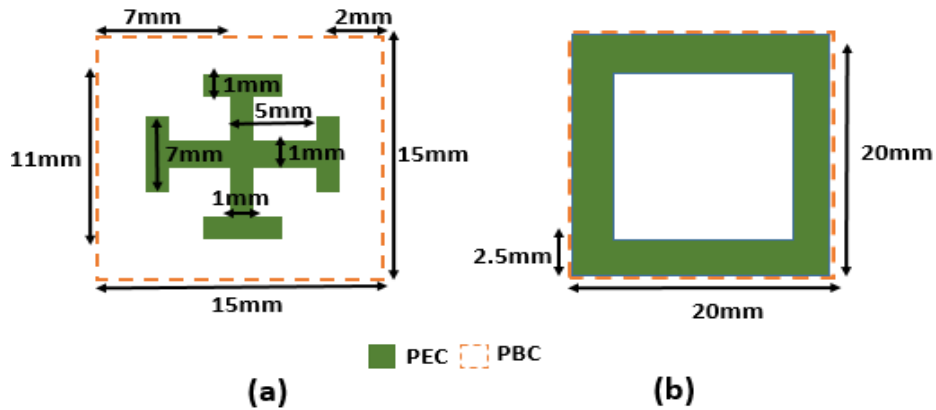
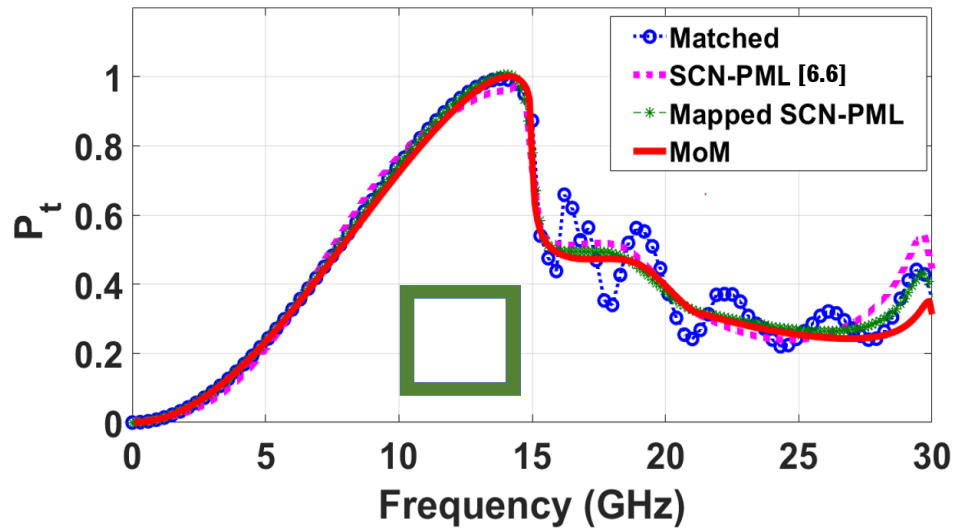


Figure 6.3. Periodic cell for : (a) JC-FSS, and a (b) Square loop FSS patch

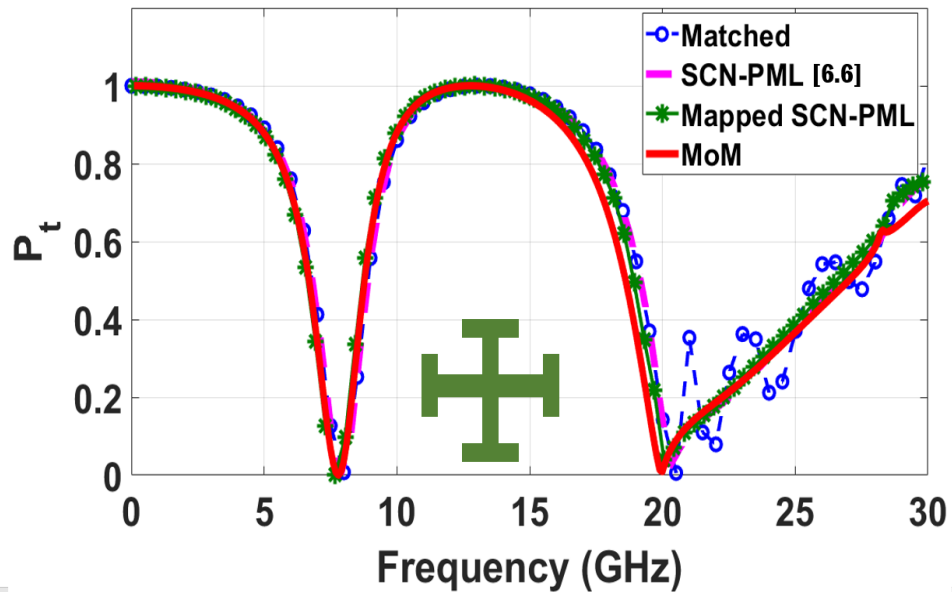
To demonstrate the accuracy of the mapped SCN-PML the computed transmitted power was compared against a benchmark result from a MoM analysis. Comparison was also made with results obtained using a TLM matched boundary and the SCN-PML published in [6.6]. The PML parameters were set as $L_{pml} = 8 dl$ and the theoretical reflection factor was set as $R_{th} = 10^{-2}$ which corresponds to a maximum conductivity of $\sigma_{max} = 4 S/m$. The PML parameters used in this investigation were chosen empirically through a process of PML tuning, as described in Section 5.2.2, in order to obtain the optimum performance. The transmitted powers from the square loop FSS and JC-FSS are presented in Figs. 6.4(a, b), respectively. The distance between the FSS and the PML was set approximately equal to the Fraunhofer distance $D \sim 2\lambda$ ($D = 50dl$) to ensure only the radiated energy is absorbed.

The result shown in Fig. 6.4a, demonstrate the overall high pass behavior of the square loop FSS; good agreement is observed in all the methods for frequencies below 15 GHz. Above 15 GHz, the first grating lobe begins to propagate and this is poorly absorbed by the simple matched boundary termination, thus explaining the oscillations shown. Both PMLs better absorb the grating lobe, as is evidenced by the absence of oscillations and agreement with the MoM analysis across the whole spectrum.

A similar behavior is observed in Fig. 6.4b for the JC-FSS. The resonant band stop behavior of the JC-FSS is observed across all methods with good agreement found up to 20 GHz. In this structure the first grating lobe begins to propagate above 20 GHz; as was observed in the square loop FSS this is also poorly absorbed by the matched boundary ABC. Again, both PMLs better absorb the grating lobes excited in the JC-FSS unit cell, evidenced by the absence of oscillations and excellent agreement with the MoM analysis across the whole spectrum.



(a)



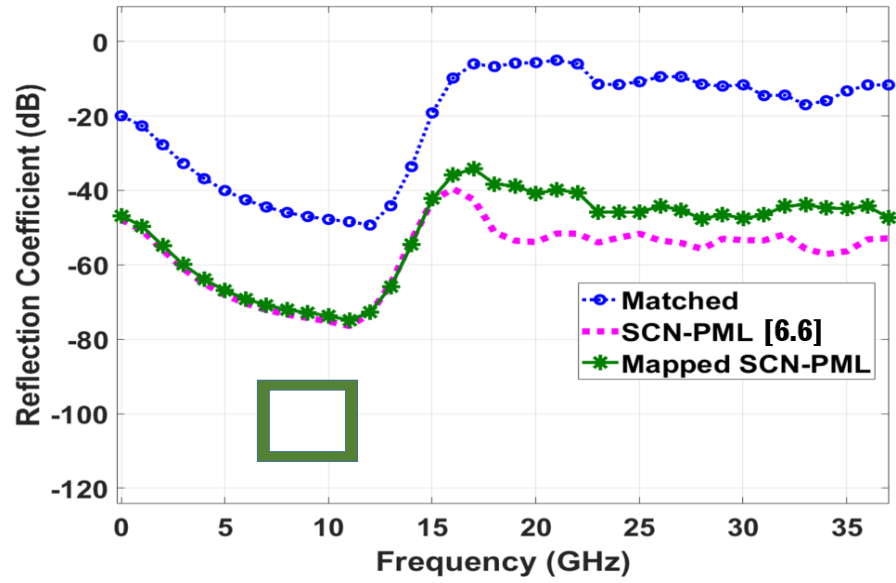
(b)

Figure 6.4. Magnitude of the transmitted power in (a) a square loop FSS (b) a JC-FSS for which the FSS to ABC distance $D = 50dl$, and PML parameters were $L_{pml} = 8dl$ and $\sigma_{max} = 4 S/m$.

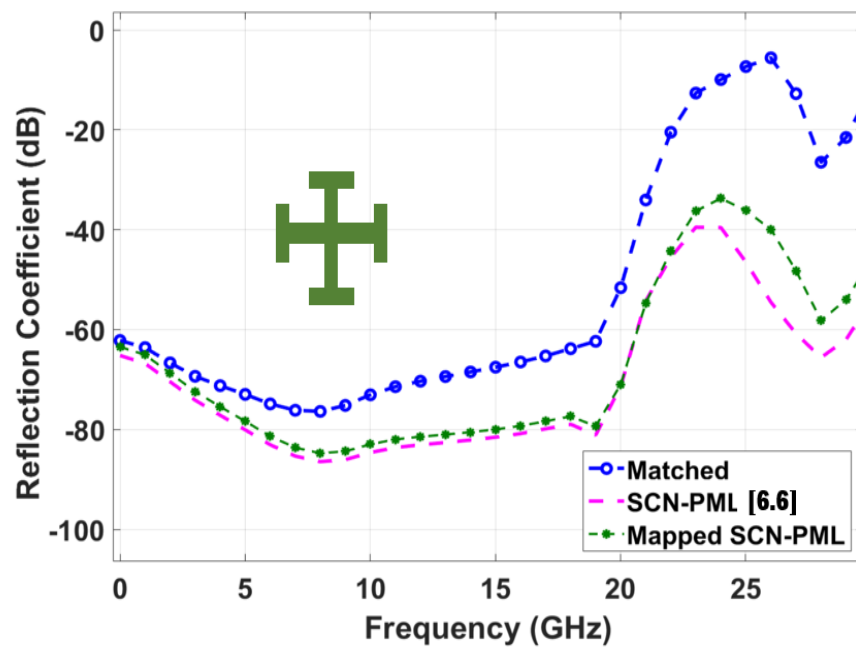
To better examine each ABCs absorption to the wave transmitted by both FSS's the reflection coefficients were also extracted from the above experiments, and the results obtained for the square loop FSS and JC-FSS are shown in Figs 6.5a and b, respectively.

For the square loop FSS, as shown in Fig. 6.5a, the highest reflection is shown to be generated in all ABCs employed above the frequencies from which the first grating lobe begins to propagate. In this structure, this corresponds to frequencies greater than 15 GHz where the matched boundary termination is shown to generate the highest reflection levels in the range of approximately -5 dB to -10 dB. The matched boundary's poor absorption of the grating lobes manifests as the oscillations which appear above 15 GHz in Fig. 6.4a. In contrast, both PMLs show better absorption to the grazing and evanescent fields where the SCN-PML developed in [6.6] is shown to produce approximately -5 dB lower reflections for the grating lobes than the mapped SCN-PML.

The same behaviour as demonstrated in the square loop FSS is observed in Fig. 6.5b for the JC-FSS. As shown, frequencies above the first grating lobe i.e. 20 GHz are more poorly absorbed by all ABCs employed. The highest reflections levels of approximately -10 dB to -20 dB are demonstrated by the matched boundary termination. This is a slight improvement to the performance obtained in the square loop FSS. This also explains why the magnitude of the oscillations observed in Fig. 6.4b are lower than those observed in Fig. 6.4a. Similarly, both PMLs show better absorption to the matched boundary across the bandwidth of operation. The SCN-PML [6.6] can be seen to produce approximately -5 dB lower reflections for the grating lobes than the mapped SCN-PML.



(a)



(b)

Figure 6.5 Numerical reflections generated by the matched boundary, SCN-PML [6.6] and mapped SCN-PML in a TLM simulated (a) square loop FSS (b) a JC-FSS.

Although both PMLs demonstrate close performance for both FSS structures investigated differences however arise in their temporal behavior. For the above simulation and PML parameters, the SCN-PML [6.6] showed instabilities in the late-

time for both structures. A time domain plot showing the instability generated in the square loop FSS simulation is shown in Fig. 6.6. On the other hand no instabilities were observed with the mapped SCN-PML.

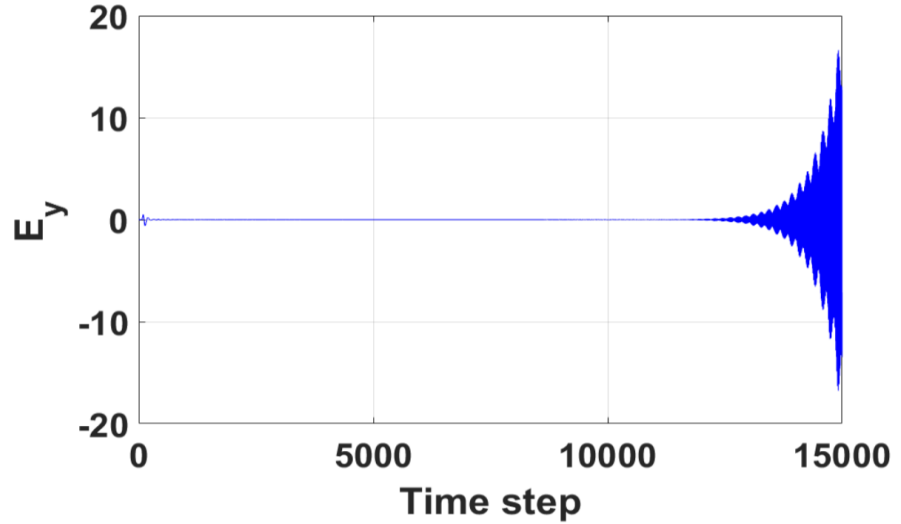


Fig.6.6. Instability generated by the SCN-PML [6.6] in a TLM simulation of a square loop FSS.

As a final investigation, the overall temporal stability of mapped SCN-PML was studied. This involved a parameter sweep on the PML parameter σ_{max} , varying the distance D between the FSS and PML media and using different mesh refinements. For all parameter choices explored no instabilities were observed when using the mapped SCN-PML in simulations terminated after 2 million time steps. On the other hand, the SCN-PML [6.6] introduced instabilities which could be delayed if: i) the strength of the PML medium was reduced i.e. $\sigma_{max} \rightarrow 0$, ii) the mesh was more finely discretized $dl \rightarrow 0$ and iii) the distance D between the FSS and PML media was increased. This elucidates an important benefit of the mapped SCN-PML since a lower absorption and a larger computational domain is otherwise required to ensure instabilities are at best delayed.

6.2 Radiation and Scattering Applications

This section investigates, the effectiveness of the mapped SCN-PML in radiation and scattering applications. In such applications, a high quality ABC is

critical to ensure the outgoing fields are unperturbed by the presence of the finite domain. Due to the angle dependent performance of most ABCs, the radiating/scattering source is required to be placed at a considerable distance away from the domain boundaries. This creates an unwanted buffer region which further degrades the overall computational efficiency. A key advantage of the PML over the analytical ABC is the higher absorbing performance demonstrated for a wider angle of incidence. This means, a higher computational efficiency is attainable since the radiation/scattering sources can be placed closer to the PML interface.

The aim of the study carried out in this section is to investigate the overall reduction in buffer region (and thus overall computational grid) whilst employing the mapped SCN-PML. Two test cases are studied. The first test case involves the computation of the radar cross section (RCS) of a metal sphere illuminated by a plane wave and the second test case calculates the mutual coupling of two dipoles as a function of separation. Both test cases have been deliberately chosen as the results are sensitive to the performance of the boundary conditions applied to the truncated computational domain. The accuracy of the test cases are determined by benchmarking the results against the analytic solutions. The computational efficiency advantage of employing the mapped SCN-PML is thus evaluated through comparisons with simulations employing the commonly used matched boundary termination.

6.2.1 Metallic scatterer

The first test case consists of the calculation of the RCS of a perfectly conducting sphere. As shown in Fig. 6.7, a sphere with a radius of 1 m and was positioned at the centre of the computational domain such that the sphere's centre to the outer boundary is denoted by a distance d .

The sphere was illuminated by a Gaussian plane wave with a 200 MHz bandwidth and 150 MHz centre frequency excited from a Huygens surface [6.7] enclosing the sphere. The rest of the domain is filled with a vacuum. For this problem, the mesh was uniformly discretized using mesh length $\Delta l = 0.025 m$. This resolution was found to provide a sufficiently accurate result (with respect to mesh density) for

the effects of the boundary conditions to be clearly observed. The PML medium with thickness L_{pml} was situated within the computational domain which was backed by the standard TLM matched boundary condition.

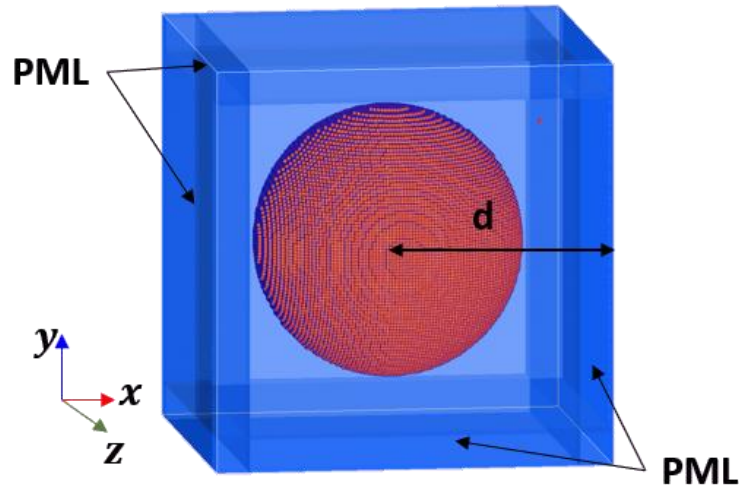


Figure 6.7 PEC sphere in cubic computational domain with PML applied on the domain boundaries.

The time domain scattered field is recorded on a second surface outside the Huygens surface and this is used to calculate the time domain far field and hence the frequency domain RCS.

Several simulations were performed where the distance d from the sphere's centre to the outer boundary were varied. The RCS results of the simulations conducted are shown along with the analytic solution [6.8] in Fig. 6.8. Three test cases involving the matched boundary and two test cases involving the mapped SCN-PML are presented. For the test cases involving the matched boundary d was varied as follows: 1.5 m, 2.0 m and 4.0 m. For both test cases involving the PML the distance d was set to 1.5 m whilst the PML medium thicknesses were varied between $L_{pml} = 0.20$ m (i.e. $N_{PML} = 8$ layers) and $L_{pml} = 0.25$ m (i.e. $N_{PML} = 10$ layers). The PML parameters were set as: $R_{th} = 10^{-4}$ for both cases where a parabolic PML conductivity grading was employed. Clearly, as shown in Fig. 6.8, if a matched boundary is used then a distance of at least 4 m from the centre of the sphere to the outer boundary is

required in order to obtain acceptable agreement with the analytic result. However, a similar level of accuracy can be obtained using both PMLs ($L_{pml} = 0.20\text{ m}$ and $L_{pml} = 0.25\text{ m}$) in a mesh with outer boundary distance of only 1.5 m. This demonstrates that a significant accuracy is attainable even when the PML medium is placed very close to the scattering object.

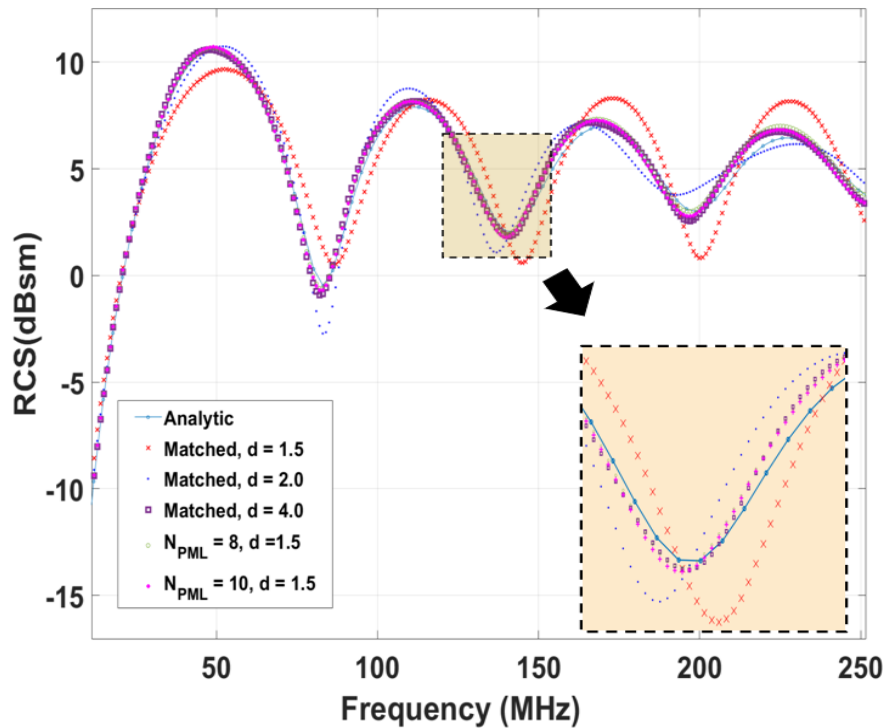


Figure 6.8 Analytic RCS result of a 1 m metal sphere compared with the TLM simulation results obtained from different computational domains terminated with the matched / PML boundaries.

To quantify the computational efficiency gained from using the PML, the computational costs in terms of the simulation run time and memory occupied for each of the test cases is presented in Table 6.1. As shown, the highest overall computational cost is incurred for the case where $d = 4.0\text{ m}$ and only a matched boundary condition is applied. However, for the same level of accuracy employing a PML with thickness $L_{pml} = 0.20\text{ m}$ with $d = 1.5\text{ m}$ yields lower computational costs. The main computational expense when employing the PML is shown to be in terms of the additional memory storage which arises due to the PML auxiliary terms required to compute the TLM scatter (see Section 4.3.2). For this reason, in this design, the

PML with $L_{pml} = 0.2$ m offers the most effective solution due to the high accuracy attained and lower overall computational costs compared to the PML with $L_{pml} = 0.25$ and the simulations employing only the matched boundary.

Table 6.1 Computational expenses for different sized computational domain terminated with matched / PML boundary conditions on a 6 core Intel i7-9850H @ 2.6 GHz with 32 GB available RAM.

	d (m)	<i>Thickness of PML</i> L_{pml} (mm) (Number of PML layers N_{PML})	<i>Mesh size</i>	<i>Memory</i> (MB)	<i>Run</i> <i>time</i> (h)
case 1	1.5	0	43200	3,304	0.28
case 2	2	0	102400	8,279	0.69
case 3	4	0	819200	17,675	1.34
case 4	1.5	0.20 (8)	43200	3,513	0.38
case 5	1.5	0.25 (10)	43200	3,604	0.41

6.2.2 Antenna Coupling

The second test case involved investigating the coupling between two thin wire dipoles as a function of their separation. The x directed dipoles were modelled using the TLM thin wire model [6.9]. The source dipole has a voltage source with a series resistance of 50Ω and the receiver dipole is loaded with a high impedance. In the simulation the time domain current on the source dipole, $i_1(t)$, and the voltage on the receiver dipole, $v_2(t)$, are recorded. These are Fourier transformed and the mutual impedance, $Z_m(f) = v_2(f)/i_1(f)$ is calculated.

The computational domain illustrating a single separation is shown in Fig. 6.9 where both dipoles are 0.05 m long and the dipole wire radii are 0.01 mm. The mutual impedance for separations in the z direction from 0.01 m to 1 m are calculated at a frequency of 2.7 GHz where the distance to the outer boundary in the x and y directions is kept constant. Each separation requires a different mesh and a separate simulation. This is an excellent test for absorbing boundary conditions as the aspect ratio of the meshes become very large for large antenna separations and reflections from the outer boundaries at close to grazing angles become significant. Consequently, this requires increasing the buffer region.

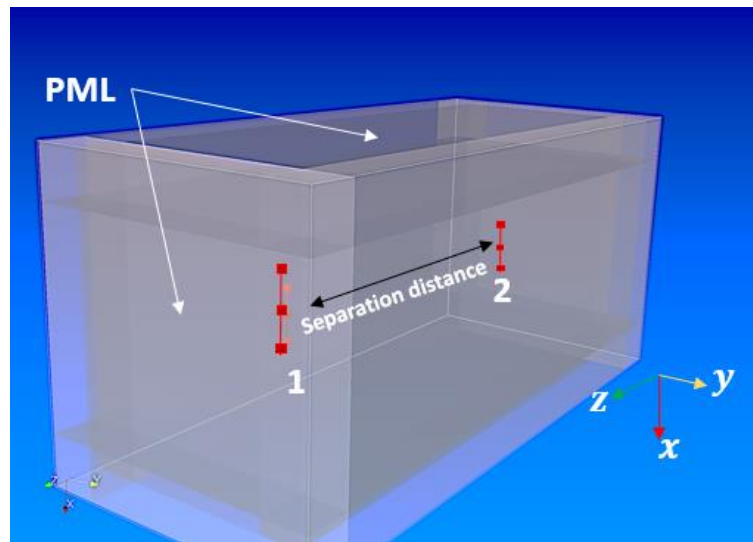


Figure 6.9 Illustration of a computational domain showing a dipole coupling model with PML applied on domain boundaries. The source dipole is labelled as “1” and the receiver dipole is labelled as “2”.

Six simulations were performed in the dipole mutual impedance tests. Four of these test cases involved employing the matched boundary where the distance in the x , y and z -directions to the outer boundary were varied as follows: 0.0525 m, 0.1025 m, 0.1525 m, and 0.2025 m. The remaining two test cases employed a PML with a thickness $L_{pml} = 0.025$ m where the distances to the outer boundary was set as 0.0525 m and 0.1025 m. The PML theoretical reflection factor was set as $R_{th} = 10^{-4}$ where a parabolic PML conductivity was applied. The results of these simulations are shown in Fig. 6.10 which shows the magnitude of the mutual impedance $|Z_m|$ in dB along

with the results of the analytic solution [6.10]. The results using the matched boundary, whilst being reasonable for separations up to 0.1 m, show significant deviations from the expected results for higher separations due to reflections from the outer boundary of the problem space. These reflections arise since by increasing the antenna separation the longitudinal dimension of the computational domain is also increased, as such this results in an increase in grazed angle incident at the outer boundary. The two PML results are very close to the analytic result, even for very large separations. This demonstrates sufficient absorption of the grazed incident waves for a relatively smaller size of computational domain.

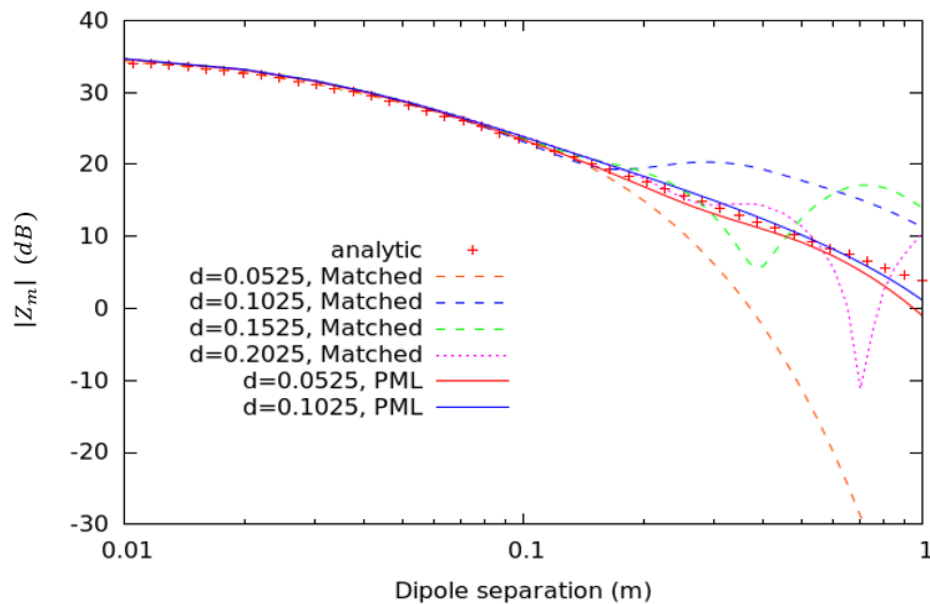


Figure 6.10. Magnitude of mutual impedance as a function of dipole separation distance. Results with matched boundaries (dashed curves), PML (solid curves) and analytic solution (crosses).

Fig. 6.11 and Fig. 6.12 show the magnitude of the E_x field component at 2.7 GHz over the problem space for a dipole separation of 0.4 m for the matched boundary and PML respectively. Both simulations are for an outer boundary distance of 0.1525 m.

The matched boundary field plot in Fig. 6.11 clearly shows the interference effect of the field reflected from the outer boundary whereas the PML field plot in Fig.

6.12 shows the absorption of the outward going wave in the PML and the expected undistorted spherical waves in the far field of the source dipole antenna. The matched boundary field plot shows a very low field value in the region of the receiving antenna; this corresponds to the minimum in the green dashed curve in Fig. 6.10.

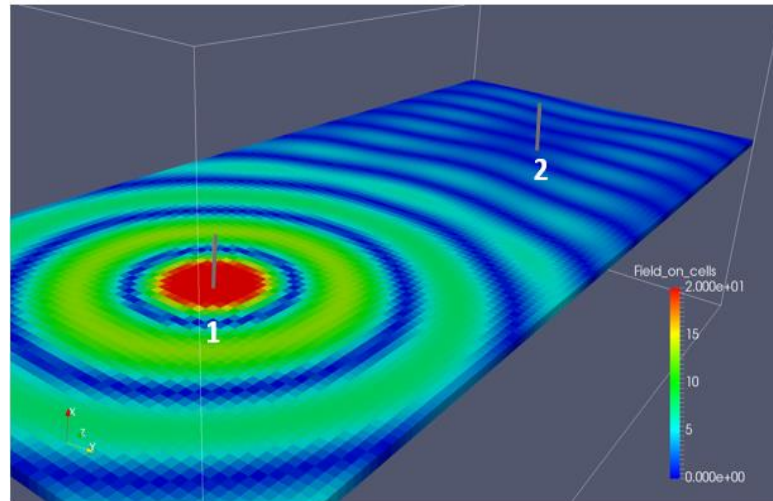


Figure 6.11 Magnitude of the E_x field component at 2.7 GHz with a matched boundary for a dipole separation of 0.4 m.

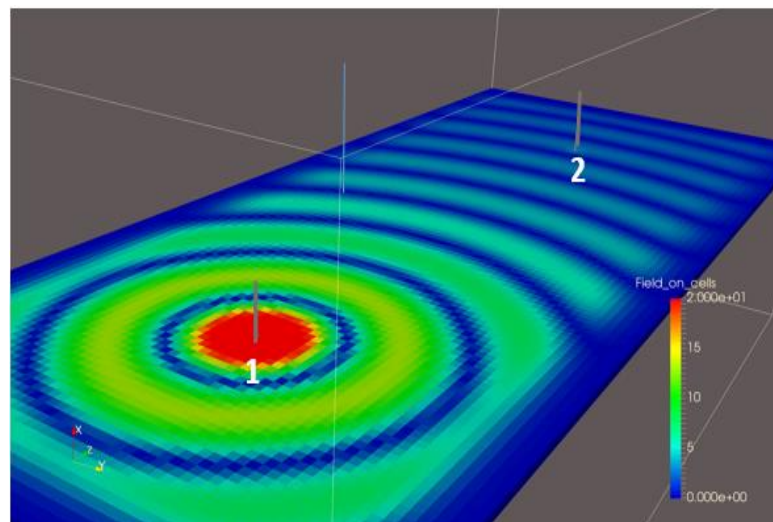


Figure 6.12. Magnitude of the E_x field component at 2.7 GHz with a PML for a dipole separation of 0.4 m.

6.3. Inhomogeneous Media

The final application studied in this chapter involves simulating the field penetration through an infinitely extended substrate. This test was chosen because it offers a straightforward demonstration for problems where the inhomogeneity in the physical domain overlaps into the PML medium. For such problems it is more efficient to simulate the computational domain using the 15-port Type I Hybrid SCN. For this reason, the mapped Hybrid SCN-PML formulation developed in Section 4.3.3 will be employed to effectively model the material inhomogeneity in the PML region.

An illustration of the computational domain of the problem simulated is shown in Fig. 6.13. As shown a 3 mm thick slab was placed at the middle of a cubic grid with dimensions $v \times v \times v$ mm which was uniformly discretized using $dl = 0.3$ mm. For the purpose of the investigation a 60 GHz differentiated Gaussian pulse was used as an excitation signal for the source which was placed 2 mm away from the slab. The material parameters of the substrate were chosen to represent the effective material properties of a composite structure (as reported in [6.11]) and are given as: $\epsilon_{ry} = 2$, $\sigma_{ey} = 10000 \text{ Sm}^{-1}$. The infinite extent of the domain was simulated by placing matched / PML boundary conditions on the outer boundary of the computational domain. When employing the PML the infinite extent of the substrate was simulated by overlapping the material properties of the slab into the PMLs on the x and z axis. At best when modeling lossy media the split-field based SCN-PMLs proposed in [6.6] and [6.12] can only be applied to cases with isotropic losses i.e. $\sigma_{ex} = \sigma_{ey} = \sigma_{ez}$. This is because the PML field attenuation in the split-field based scheme is achieved by treating the PML as a lossy medium. As such these formulations are unable to simultaneously incorporate both the material loss and PML loss. For this reason such schemes cannot be applied to the above test case, or similar problems.

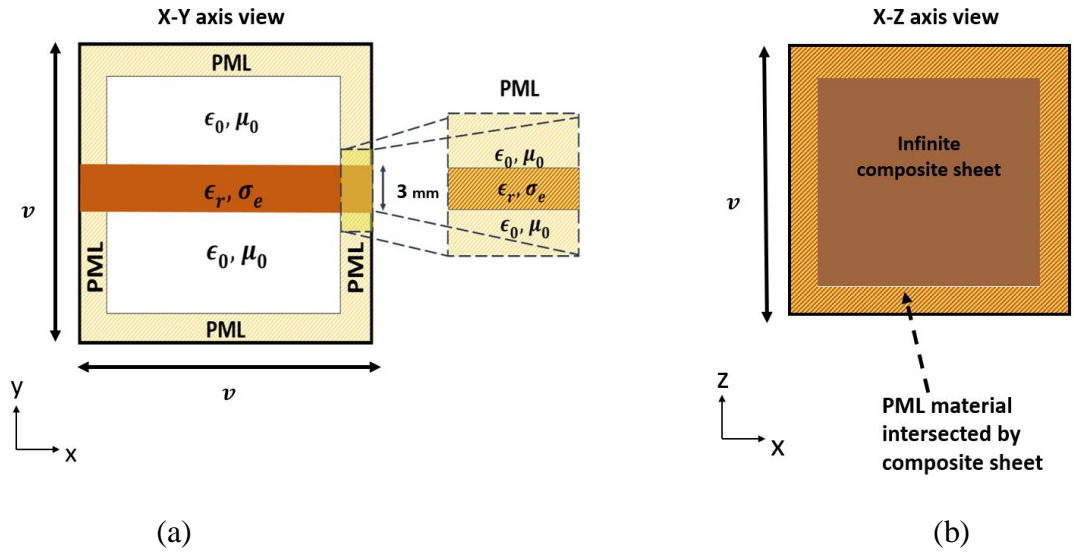


Figure 6.13. Image showing a 3 mm thick infinitely extended composite sheet suspended in a $v \times v \times v$ computational domain : (a) x-y view (b) x-z view of the material space showing intersection into the PML region.

The transmitted fields E_y^{trans} were obtained 2 mm at the opposite side of the slab. The shielding effectiveness was then computed as follows:

$$S.E_{dB} = 20 \log_{10} \frac{\mathcal{F}(E_y^{inc})}{\mathcal{F}(E_y^{trans})} \quad (6.2)$$

where E_y^{inc} represents the incident field which was obtained by running the same simulation but without the slab in place.

Several tests were carried out all of which investigate the accuracy of the shielding effectiveness results as the size of computational domain v is varied. For each test case the accuracy of the different boundary conditions employed was evaluated by observing the convergence to a reference solution. In this study, the reference solution represents the solution obtained by significantly extending the dimensions of the domain v such that reflection effects from the boundaries are absent at the observation point. This therefore represents the *perfect* result and this was found to be for the case where $v = 100 \text{ mm}$ for simulations terminated after 1200 time steps.

The results of the shielding effectiveness from five different simulations are shown in Fig. 6.14. Two of these tests involved terminating the computational domain with the matched boundary where the dimension v for each was given as : 15 mm and 50 mm. For the test cases involving the PML a 5 layer (i.e. 1.5 mm thick) medium was employed where the theoretical reflection factor was set as $R_{th} = 10^{-4}$. For a parabolically graded PML media this corresponds to a maximum $\sigma_{max} = 20 S/m$. The PML results for the cases where $v = 10 mm$ and $v = 15 mm$ are shown in Fig. 6.14. The superior absorbing quality of the mapped HSCN-PML is clearly demonstrated by the absence of oscillations in the results and the better convergence with the reference solution compared to the simulations employing the matched boundary termination. The results show a substantially higher accuracy can be attained in a smaller computational domain terminated by the PML compared to the same domain size terminated by the matched boundary. Although when employing the matched termination the test case where $v = 50 mm$ shows better agreement than the case where $v = 15 mm$, however oscillations are still noticeable in the results. In order to improve the convergence of the matched termination the computational domain would have to be significantly extended beyond $v = 50 mm$. As shown in Table 6.2 compared to the test cases employing a 5 layer PML this signifies a substantial increase in the simulation time and computational memory.

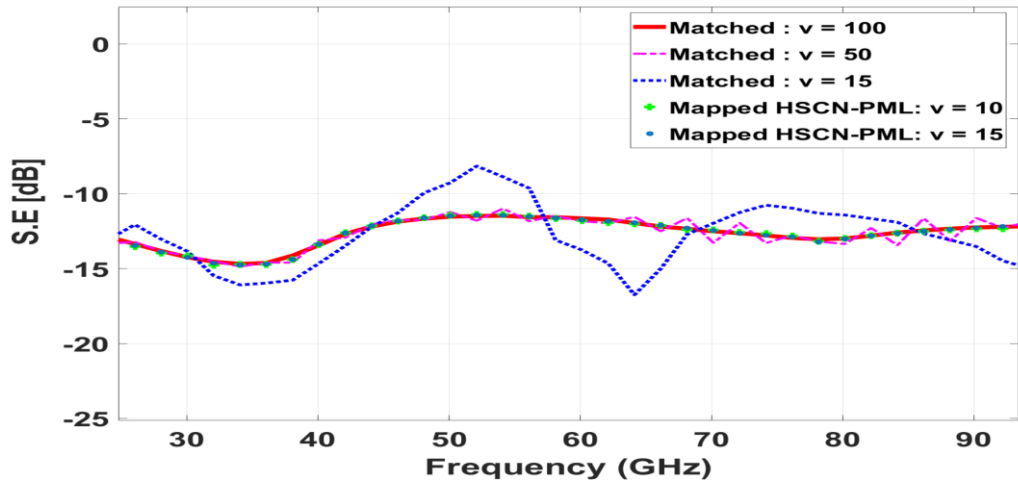


Figure 6.14. Shielding effectiveness of an infinitely extended lossy dielectric slab embedded in free space computed in TLM simulation employing matched/PML boundary terminations.

Table 6.2 Computational expenses for different sized computational domain terminated with matched / PML boundary conditions on a 6 core Intel i7-9850H @ 2.6 GHz with 32 GB available RAM

	ν (mm)	Thickness of PML (mm) (Number of PML layers)	Mesh size	Memory (MB)	Run time (h)
case 1 (reference)	100	0	37037037	22596	4.656
case 2	50	0	4629629	9374	0.462
case 3	15	0	125000	274	0.011
case 4	10	1.5 (5)	37037	200	0.004
case 5	15	1.5 (5)	125000	290	0.015

6.4 Summary

This chapter demonstrated the capability of the mapped SCN-PML in a variety of practical electromagnetic applications. Four applications were studied namely, (i) simulating the transmittance of planar Frequency Selective Surfaces (FSS) (ii) investigating the RCS of a metallic body, (iii) simulating the coupling between two dipole antennas, and finally (iv) terminating the domains of inhomogeneous media. Each test case was carefully chosen to evaluate the PML under specific test conditions. For each of the test carried out the PML results were benchmarked against a reference solution to highlight the accuracy as well as the overall computational efficiency.

The first application investigated involved simulating the transmittance of a JC and square loop FSS. In this test the mapped SCN-PML was employed in terminating the out of the plane direction of the computational domain. Compared to the matched boundary termination the results obtained from the mapped SCN-PML demonstrated excellent convergence compared with the benchmark solutions from MoM simulations. Approximately 35 dB absorption was demonstrated for the Floquet modes, therefore highlighting a capability to better absorb grazed incident waves. Compared with existing SCN-PML methods the mapped SCN-PML demonstrated excellent temporal behaviour by the absence of instability even in the presence of strong evanescent energy.

Next, the computational efficiency advantage from employing the mapped SCN-PML was demonstrated in radiation and scattering applications. The results demonstrated a substantial reduction in the buffer region is attainable by employing 8 layer PML. This was shown to translate to a significant reduction in the computational costs in terms of memory and overall run time.

The chapter was concluded by demonstrating the capability of the mapped HSCN-PML in terminating materially inhomogeneous media. An investigation was carried out which involved simulating the shielding effectiveness of an infinitely extended composite substrate suspended in free space. Compared to the matched boundary condition, the results obtained show excellent convergence to a reference

case was attainable for a significantly smaller computational domain. This demonstrates that the presence of a non-uniform media interfacing the PML does not result in high reflections propagating into the computational domain. In addition, this test case demonstrates an added advantage of the proposed PML formulation over the existing split-field based TLM-PML schemes which cannot be applied to cases involving anisotropic lossy domains.

References

- [6.1] X. Dardenne and C. Craeye, "Method of Moments Simulation of Infinitely Periodic Structures Combining Metal With Connected Dielectric Objects," in *IEEE Transactions on Antennas and Propagation*, vol. 56, no. 8, pp. 2372-2380, Aug. 2008.
- [6.2] W.L. Ko, and R. Mittra, "Implementation of Floquet boundary condition in FDTD for FSS analysis" Proc. 1993 IEEE Antennas Propagat. Soc.Intl.Symp., Ann Arbor, MI., Vol.1 , pp.14-17, 1993.
- [6.3] J. G. Maloney and M. P. Kesler, "Scattering Analysis of Periodic Structures Using Finite-Difference Time-Domain," CA, USA: Morgan & Claypool, 2012.
- [6.4] J. A. Roden, S. D. Gedney, M. P. Kesler, J. G. Maloney, and P. H. Harms, "Time-domain analysis of periodic structures at oblique incidence orthogonal and nonorthogonal FDTD implementations," *IEEE Transactions on Microwave Theory and Techniques.*, vol. 46, no. 4, pp. 420-427, 1998.
- [6.5] G. Romo and T. Smy, "Modeling of photonic crystals using a real valued transmission line matrix method," *J. Appl. Phys.*, vol. 94, no. 4, pp. 2177–2182, 2003.
- [6.6] J. L Dubard, and D. Pompei "Optimization of the PML efficiency in 3-D TLM method." *IEEE Transactions on Microwave Theory and Techniques*; 48(7):1081–1087, 2000.
- [6.7] A. Taflove, *Computational Electrodynamics - The Finite Difference Time Domain Method*, 2nd ed. Boston: Artech House, 2000.
- [6.8] G.T. Ruck, D.E. Barrick, W D. Stuart and C.K. Krichbaum, "Radar Cross Section Handbook," Plenum Publishing Co, vol 1, 1970.

- [6.9] A.J. Włodarczyk, V. Trenkic, R.A. Scaramuzza and C. Christopoulos, “A fully integrated multiconductor model for TLM,” *IEEE Trans. MTT*, vol. 46, no 2, pp 2431-2437, Dec 1998.
- [6.10] G.H. Brown and R. King, “High Frequency Models in Antenna Investigations,” *Proc IRE*, vol 22, pp 457-480, 1934.
- [6.11] M. S. Sarto, “A new model for the FDTD analysis of the shielding performances of thin composite structures,” *IEEE Transactions on Electromagnetic Compatibility*, vol. 41, no. 4, pp. 298–306, 1999.
- [6.12] L. Maguer, and M. M. Ney, “Extended PML-TLM node: an efficient approach for full waveanalysis of open structures.” *Int. J. Numer. Model.*, vol. 14 , pp. 129–144, 2001.

Chapter 7

Conclusions

7.1 Summary of the Work

The overall objective of this project was to formulate a technique to enable the effective termination of TLM meshes. To achieve this, this thesis has focused on developing a novel stretched coordinate (SC) TLM-PML implementation. Prior to this work a handful of TLM-PML formulations have been proposed however these schemes demonstrate a weak temporal stability which thus limits their effectiveness in a broad class of electromagnetic applications. To address this problem, particular consideration was to be made on the discretization approach taken in order to ensure the highly desired unconditional stability of the TLM method is maintained upon implementation. A summary of the discussions, developments and findings made in this thesis thus follows.

In Chapter 2, a general discussion of the behavior of the PML equations in the continuous and discrete domains was delivered. The theory of the PML was presented through the split-field, uniaxial and stretched-coordinate PML interpretations. The main distinctions between each PML interpretation was highlighted. The advances of the PML was discussed as well as the limitations in practical applications. The discretization of the PML equations was described to alter the highly desirable PML “perfect” matching condition and generate spurious reflections. This results in a performance discrepancy between different PML implementations.

In Chapter 3, the TLM theory was presented through its core principles. The 2D shunt and series TLM nodes were described and their analogy with Maxwell’s equations was derived. Subsequently, this led to the development of a framework for implementing the stretched coordinate PML in TLM which was formulated for the 2D TLM shunt node. The PML formulation was developed based on establishing an

analogy between the equations describing the TLM shunt node and the modified (stretched) second-order wave equations. This method is referred to as the mapped TLM-PML and when applied within the context of the shunt node it is specifically referred to as the mapped shunt-node PML. The mapped TLM-PML formulation employs a mapping approach and implements the stretched coordinate PML theory by a direct stretching of the transmission line parameters from real to complex space. This approach to PML implementation was shown to result in a complex propagation delay and complex frequency dependent line admittances/impedances. This results in a modification of the standard scatter and connect equations. The connect equations were shown to be modified by introducing an additional attenuation of propagation pulses. The modified scatter equations were derived by following the approach taken in the classical TLM theory but with an additional consideration made on how to appropriately handle the complex frequency dependent line parameters.

The performance of the mapped shunt-node PML was validated through a variety of numerical tests based on the canonical waveguide application. The first investigation carried out examined the influence of different conductivity gradings across the PML medium on the PML performance. The constant, linear, parabolic and cubic conductivity profiles were studied. The benefits of a graded conductivity profile were demonstrated by the comparatively lower reflection levels achieved compared to the constant profile case. The best performing conductivity profile was shown to be the parabolic grading.

The relationship between the numerical reflections and the theoretical reflection factor for different number of PML layers was also investigated. Results showed that the reflections generated by the mapped shunt-node PML can be significantly reduced for a given theoretical reflection factor R_{th} (dB) by increasing the number of PML layers used. It was also seen that for each application considered an optimal value of the theoretical reflection factor R_{th} (dB) exists which achieves the lowest reflections for a given choice of N_{PML} .

The ability of the mapped shunt-node PML in terminating lossy dielectric media was also demonstrated. The numerical reflections generated show that good

absorption performance (>70 dB) is maintained even when incorporating lossy media. As a final characterization test, the performance of the mapped shunt node PML was compared against the split-field TLM-PML formulation presented in [7.1] and a conventional TLM matched boundary. Both PML schemes demonstrated better absorption (>50 dB) compared to the matched boundary termination. Nonetheless, the clear advantage of implementing a SC PML formulation, is the ability to terminate both lossless and lossy dielectric media. In such applications, the split field based TLM-PML schemes fail since the node conductance G_{ez} is naturally employed by these formulations to enforce the attenuation of propagating modes in the x and y directions. Hence G_{ez} cannot be employed to suitably model the electric losses represented by the electric conductivity σ_{ez} .

Finally, for further illustrative purposes the strong absorbing capability of the mapped shunt node PML was demonstrated in a topical application, involving the plane wave scattering from a PEC airfoil with profile Naca0015. Compared to the matched boundary termination the scattered field in the computational domain was shown to be more rapidly attenuated when employing the mapped shunt-node PML.

In Chapter 4, the TLM theory in the 3D setting was presented through the Symmetrical Condensed Node (SCN). Subsequently the theory of the mapped TLM-PML framework described in Chapter 3 was extended to the SCN. Extension to hybrid SCN (HSCN) nodes was also presented. When applied in this context the mapped TLM-PML is specifically referred to as the mapped SCN-PML or mapped HSCN-PML, respectively.

In Chapter 5, the absorption performance of the mapped SCN-PML was characterized using normal and oblique incidence waveguide test conditions under different variations of the PML control parameters. An excellent absorption was demonstrated for waves impinged normally on the mapped SCN-PML medium. This behavior arises due to the approach taken in the development of the mapped SCN-PML formulation which retains the underlying propagation properties of the mapped

node. Due to this, the inherent dispersion free property of the SCN mesh under normal propagation is retained. In this manner, the mapped SCN-PML maintains a strong absorption even in the presence of a sharp conductivity variation across the medium-to-PML interface. In such conditions a single mapped SCN-PML layer with sufficiently high PML conductivity can be deployed to achieve a near perfect attenuation of the incoming waves. Compared to the previously published SCN-PML schemes which require a smooth conductivity to be applied across multiple PML layers, the mapped SCN-PML was demonstrated to be more efficient in this case.

The excellent performance observed for normal incidence waves was shown to degrade in the case where the incoming waves are impinged from an off-normal angle. For oblique incidence waves, transitional reflections were shown to be generated by the mapped SCN-PML, and similar to other SCN-PML schemes a graded conductivity profile must be applied across the mapped SCN-PML medium. Under such conditions, the limitation of the matched boundary was clearly demonstrated by the 40 dB higher reflection generated compared to the SCN-PMLs.

In practical applications, where waves are impinged from an arbitrary angle of incidence, the number of PML layers employed was shown to be the primary factor used to reduce the PML reflections. However, this comes at a cost of an increase in computational demand. Nevertheless, the relative computational burden incurred by the PML medium decreases as the complexity or scale of the problem domain increases. It is in such test conditions that the PML benefits of improved accuracy can be truly realized. To optimize the PML design a guideline for tuning the PML was briefly discussed. Through this the overall absorption behavior for a given test condition can be obtained which could reveal the most suitable (and optimum) combinations of PML parameters to achieve a target reflection performance.

The temporal stability of the mapped SCN-PML was demonstrated through the canonical waveguide iris test case. Compared to published SCN-PML schemes no appearance of instabilities was shown in the simulations employing the mapped SCN-PML even in the presence of high evanescent energy interacting with the PML interface. As an additional test the temporal response of the mapped SCN-PML for

waves impinged on the layer for long durations of time was also investigated. No long-term instabilities were observed in this test case which further demonstrated the strength of the mapped TLM-PML framework.

In Chapter 6, the effectiveness of the mapped SCN-PML in practical electromagnetic simulations was further demonstrated through a variety of applications. The test cases investigated were carefully chosen to evaluate the PML under specific test conditions. For each of the test carried out the PML results were benchmarked against a reference solution to highlight the accuracy as well as the overall computational efficiency.

The first application investigated involved simulating the transmittance of a Jerusalem Cross (JC) and square loop FSS. In this test the mapped SCN-PML was employed in terminating the out of the plane direction of the computational domain. Compared to the matched boundary termination the results obtained from the mapped SCN-PML demonstrated excellent convergence compared with the benchmark solutions from MoM simulations. Approximately 35 dB absorption was demonstrated for the Floquet modes, therefore highlighting a capability to better absorb grazed incident waves. Compared with existing SCN-PML methods the mapped SCN-PML demonstrated excellent temporal behaviour by the absence of instability even in the presence of strong evanescent energy.

The second application involved evaluating the computational efficiency advantage obtained from employing the mapped SCN-PML in radiation and scattering applications. This was carried out by simulating the RCS of a metallic body and also simulating the coupling between two dipole antennas. The results demonstrated by both studies show that a substantial reduction in the buffer region is attainable by employing 8 layer PML. This was shown to translate to a significant reduction in the computational costs in terms of memory and overall run time.

The final investigation carried out involved simulating the shielding effectiveness of an infinitely extended composite substrate suspended in free space.

For this test the mapped HSCN-PML was employed in terminating the materially inhomogeneous media. Compared to the matched boundary condition, the results obtained show excellent convergence to a reference case was attainable for a significantly smaller computational domain. This demonstrates that the presence of a non-uniform media interfacing the PML does not result in high reflections propagating into the computational domain. Furthermore, this test case was used to demonstrate an added advantage of the proposed PML formulation over the existing split-field based TLM-PML schemes which cannot be applied to cases involving anisotropic lossy domains

7.2 Future Work

The investigations carried out have demonstrated the utility of the proposed method in terminating Cartesian based TLM meshes. However, in order to realize the full potential of the PML, extensions of the proposed technique must be made to allow for the termination of non-Cartesian TLM grids. To date the applications of the domain truncation techniques in TLM have been restricted to the structured grid case. Non-Cartesian based TLM methods, i.e. the unstructured TLM (UTLM) [7.2] and cylindrical TLM[7.3], therefore rely on the simple but inefficient matched termination. Developing an effective SC PML formulation for either of these methods constitutes a significant advancement of the TLM method.

The theory of the mapped TLM-PML as developed in this thesis can be extended to the Cylindrical TLM node. In this case, the cylindrical SC PML equations [7.4] would be employed and the general constitutive parameters arising from mapping procedure would be sought as similarly described in Section 4.3. This would reveal the transformation of the transmission line impedances/admittances. Following from this the modified scatter and connect equations can be obtained according to the same approach described in Section 4.3.2 and 4.3.4.

Extending the mapped TLM-PML to the UTLM method can be achieved using a hybrid mesh approach which involves discretizing the PML region using the cuboidal mapped TLM-PML (as developed in Chapter 4 and interfacing this region

with a computational domain discretized using tetrahedral UTLM nodes. This approach is conceptually similar to the technique applied in [7.5] which involved a hybrid mesh consisting of a hexahedral PML region interfacing with wedge elements directly extruded from a tetrahedral mesh. To achieve this a coupling strategy between the cuboidal TLM node and the tetrahedral TLM node must be deployed in the interior domain as similarly described in [7.6]. This way a buffer region is introduced which ensures the mapped TLM-PML is interfaced by a cuboidal TLM node. A potential limitation of this approach, however, is the computational costs as a result of introducing the buffer region. Nonetheless, this is still expected to deliver a significant improvement in accuracy and computational efficiency compared to the currently employed matched boundary termination.

A more challenging but direct approach to implementing the PML in UTLM involves formulating a purely tetrahedral PML node. Achieving this would remove the need for a buffer region and also maximizes the geometric flexibility of the UTLM.

References

- [7.1] N. Pena, and M.M. Ney “A new TLM node for Berenger’s perfectly matched layer”, *IEEE Microwave and Guided Wave Lett.*, 6, (11), pp. 410-412, 1996.
- [7.2] P. Sewell, J. G. Wykes, T. M. Benson, C. Christopoulos, D. W. P. Thomas, and A. Vukovic, “Transmission-Line Modelling Using Unstructured Tetrahedral Meshes,” *IEEE T. Microw. Theory Tech.*, vol. 53, no. 6, pp. 1919-1928, June 2005.
- [7.3] J. Joković and T. Dimitrijević, "TLM cylindrical model of a coaxially loaded cylindrical cavity," *2011 10th International Conference on Telecommunication in Modern Satellite Cable and Broadcasting Services (TELSIKS)*, pp. 420-423, 2011.
- [7.4] F. L. Teixeira and W. C. Chew, “Systematic derivation of anisotropic PML absorbing media in cylindrical and spherical coordinates,” *IEEE Microw. Guided Wave Lett.*, vol. 7, pp. 371–373, 1997.
- [7.5] G. Chen, L. Zhao, W. Yu, S. Yan, K. Zhang and J. Jin, "A General Scheme for the Discontinuous Galerkin Time-Domain Modeling and S-Parameter Extraction of

Inhomogeneous Waveports," in *IEEE Transactions on Microwave Theory and Techniques*, vol. 66, no. 4, pp. 1701-1712, April 2018.

- [7.6] P. Sewell, T. M. Benson, C. Christopoulos, D. W. Thomas and A. Vukovic, "Regular space filling tetrahedral elements for transmission line modelling (TLM)," *URSI International Symposium on Electromagnetic Theory*, 2010, pp. 283-286, 2010.